Characterization, Stabilization and Coherent Combination of High Power Laser Beams for Gravitational Wave Detectors

Von der Fakultät für Mathematik und Physik
der Gottfried Wilhelm Leibniz Universität Hannover

zur Erlangung des akademischen Grades
Doktorin der Naturwissenschaften
Dr. rer. nat.

genehmigte Dissertation von

M.Sc. Nina Bode

2023

Referent:	Apl. Prof. Dr. Benno Willke Gottfried Wilhelm Leibniz Universität Hannover
Korreferent:	Prof. Dr. Michèle Heurs Gottfried Wilhelm Leibniz Universität Hannover
Korreferent:	Prof. Volker Quetschke University of Texas Rio Grande Valley
Tag der Promotion:	12.04.2023

Abstract

Current and future gravitational wave detectors (GWDs) require high power and low noise laser systems at a wavelength of $1064\,\mathrm{nm}$ in the continuous wave regime, with excellent spatial beam quality. These systems are highly complex and not commercially available. Hence, this thesis is dedicated to the development of a laser system, to be used in current GWDs, and of different concepts for laser systems, suitable to provide even laser powers of $\sim 400\,\mathrm{W}$ or larger for future detectors. It also presents a promising solution to transport the generated high power laser beams via a hollow-core fiber from the laser table into the GWD's isolated in-vacuum environment.

First, investigations on a sequential installation of solid-state laser amplifiers are presented. They confirm the suitability of these amplifiers for the generation of laser powers up to $195\,\mathrm{W}$, and uncover limitations of them. These results built the basis for the laser system that the advanced Laser Interferometer Gravitational-Wave Observatorys (aLIGOs) will use in their fourth science run, a prototype of which was tested successfully at the aLIGO Livingston site within this thesis.

In sequence, three different configurations for the coherent combination of two laser beams are reported as possibility to increase the laser power above the level available from sequential amplifier chains. They were investigated under the different aspects important for GWD laser systems. The first configuration is a pre-stabilized laser system (PSL) based on the coherent combination of two laser beams from the same seed laser source amplified by solid-state laser amplifiers, that allowed for the generation of a $100\,\mathrm{W}$ laser beam, with beam quality and noise characteristics similar or better as for current GWD systems. The second configuration is a coherent combination of two laser beams from the same seed source amplified by fiber laser amplifiers, which generated a total output power of $398\,\mathrm{W}$ with beam quality and free-running noise within the requirements of current GWD systems. This power level exceeds the laser power of $\sim 200\,\mathrm{W}$ so far available for GWD PSLs. Finally, the benefit of a variable beam splitter for the coherent combination of two independent laser beams with different power levels, is demonstrated.

As final investigations, novel technologies for the generation and transportation of laser beams at the power levels required for future GWDs are presented. The coherent combination of three laser beams with a bow-tie resonator as combining element is a promising possibility for further power scaling. The first results of a proof-of-experiment are promising and further plans for an extension of this concept are described. The transportation of high power laser beams from the laser table to the GWD main vacuum system is especially challenging. Here, an analysis of the beam quality and laser noise of a high power beam transported by a hollow core fiber, encourages for further research in this direction.

The results presented in this thesis built a foundation for the challenging development of high power laser systems at a wavelength of $1064\,\mathrm{nm}$ and the transportation of the generated laser beams for current and future GWDs.

Keywords: high power laser system, laser amplification, coherent beam combination, hollow core fiber, laser stabilization, gravitational wave detection

Contents

List of acronyms

aLIGO	advanced Laser Interferometer Gravitational-Wave Observatory
AOM	acousto-optic modulator
ASD	amplitude spectral density
CBC	coherent beam combination
CCD	charge-coupled device
CDS	real-time digital control and data acquisition system
DC	direct current
eLIGO	enhanced Laser Interferometer Gravitational-Wave Observatory
EOM	electro-optical modulator
FFT	fast Fourier transform
FSR	free spectral range
DBB	diagnostic breadboard
ET	Einstein Telescope
GWD	gravitational wave detector
HG	Hermite-Gaussian
HOM	higher-order mode
KAGRA	Kamioka Gravitational Wave Detector
LISA	Laser Interferometer Space Antenna
LO	local oscillator
Nd:YAG	neodymium-doped yttrium aluminum garnet
Nd:YVO_4	neodymium-doped yttrium orthovanadate
NPRO	non-planar ring oscillator
PBS	polarizing beam splitter
PER	polarization extinction ratio
PMC	pre-mode-cleaner
PSL	pre-stabilized laser system
PZT	piezo-electric element
QPD	quadrant photodiode
RF	radio frequency
RPD	relative power noise photodiode
RMS	root mean square
RPN	relative power noise
SQL	standard quantum limit

SBS stimulated Brillioun scattering

TEM transverse electromagnetic

TFP thin film polarizer

TPD transmission photodiode

1. Introduction

High power, narrow linewidth and high beam quality laser systems are required for the current and next generation of ground-based interferometric GWDs. This chapter will motivate and give background information for the experimental laser system development that was performed in the scope of this thesis. It will be split in three sections. The first section will give an overview about gravitational waves and their detection. This includes information about the existing and next generation of interferometric GWDs. The second section will describe the requirements on laser systems for GWDs based on the coupling of the certain laser beam properties to the interferometer sensitivity. Hence, the second section gives the objectives for the investigations on laser systems for GWDs. The third section will describe two concepts for the development of high power laser systems, which are used in different configurations in the experimental work that is presented in Chapter 3 and Chapter 4.

1.1. Gravitational waves and their detection

Gravitational waves are spacetime deformations caused by accelerating massive objects, like inspiraling neutron stars or black holes. They cause a periodical stretching and compressing of the perpendicular axes of space-time and were first predicted in 1916 by Albert Einstein as a result of his general theory of relativity [1]. Up to date, a network of five ground-based interferometric GWDs are operating. All of the detectors are enhanced Michelson interferometers with arm lengths L from several hundred meters up to several kilometers as shown as simplified schematic in Figure 1.1. The sky-localization of the gravitational wave signals is determined via triangulation, and the total measurement confidence is increased with more detectors. The gravitational wave signal in a GWD is measured as strain. The strain $h_{\mathrm{gw}}(f)$ is defined over the arm length difference change triggered by the gravitational wave signal divided by the arm length, and is limited by the detector noise given as a amplitude spectral density (ASD) with the unit $1/\sqrt{\mathrm{Hz}}$.

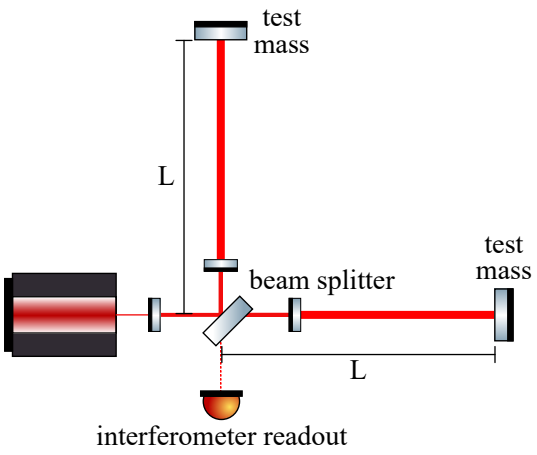

Figure 1.1.: Simplified schematic of an interferometric GWD with arm length L.

The two American aLIGO detectors [2], located in Hanford, Washington, and Livingston, Lousiana, are the so far most sensitive detectors. They have arm lengths of

$4\,\mathrm{km}$ and aim to measure gravitational wave signals with a design strain sensitivity in the order of $10^{-24}\,1/\sqrt{\mathrm{Hz}}$ in the frequency band between $100\,\mathrm{Hz}$ to several kilohertz. The aLIGOs were the first detectors that were sensitive enough to measure a gravitational wave signal in 2015. Their direct measurement of a gravitational wave originating from the inspiraling and merging of two black holes opened the area of gravitational wave astronomy. The Advanced Virgo detector in Italy [3] joined the aLIGOs in August, 2017. It has $3\,\mathrm{km}$ long arms and, at most signal frequencies, a slightly lower design sensitivity than aLIGO.
aLIGO and Advanced Virgo measured several gravitational wave signals in three observing runs over the last years, which are summarized in gravitational wave catalogs [4–7]. Most of the so far measured signals were caused by inspiraling and merging black hole pairs, but also signals origin from neutron star pairs as well as neutron star black hole pairs were detected. The first measured inspiraling and merging neutron star pair signal was a multi-messenger event, which was detected not only by GWDs but also by a number of optical telescopes [8]. The scientific output of the measurements gave already an interesting insight in the early development of the universe including for example the origin of rare earth metals.
The Kamioka Gravitational Wave Detector (KAGRA) [9, 10], in Japan, joined the GWD network in 2019 and did it's first observing run together with the German-British GEO600 detector [11, 12], located in Germany, while the other detectors went into an early commissioning break to prepare for their fourth observing run [13]. KAGRA is the first detector with the infrastructure to work at cryogenic temperature to reduce thermal effects at low measurement frequencies. It is constructed under ground and has arm lengths of $3\,\mathrm{km}$. KAGRA aims at a sensitivity level close to Advanced Virgo.
aLIGO and Advanced Virgo are second generation gravitational wave detectors. They partly use the infrastructure from the first generation detectors, which are upgraded on the basis of knowledge that was gained in research groups within the GWD community and at the GEO600 detector. KAGRA in comparison has some third generation infrastructure and can, thus, be sorted in between the second and third generation of GWDs.
The GEO600 detector has an arm length of $600\,\mathrm{m}$ and a sensitivity of $10^{-22}\,1/\sqrt{\mathrm{Hz}}$ at frequencies around $1\,\mathrm{kHz}$. GEO600 has not measured any gravitational wave signals so far, but plays an important role as technology demonstrator for the other detectors.
The measurable gravitational wave signal amplitude for specific gravitational wave sources defines how far away and how long ago an event that causes the emission of a gravitational wave can be detected. By increasing the detector sensitivity an increasing number of gravitational wave signals from different sources and locations can be measured. With an increasing number of detectors also the observable fraction of the universe increases and the sky localization capability of the network improves. Thus, the GWD network is still growing and the existing detectors are being improved. The second generation detectors will be extended by LIGO India which is an aLIGO like detector that is already under construction [14]. The now running detectors will be further optimized for the next science runs and upgrades into next generation detectors are planned [15–19].
The already operating 2nd generation interferometric GWDs are the first which are able to detect signals. There are several proposals for third generation GWDs. One is the European Einstein Telescope (ET) [20, 21], which is proposed to be build

in Europe and has a triangular shape with in total six interferometers with $10\,\mathrm{km}$ arm length. Another proposed third generation detector is the American Cosmic Explorer [22]. In this project two detectors similar to the aLIGO design with arm length of $20-40\,\mathrm{km}$ should be build in the United States. Both, ET and Cosmic Explorer are at advanced planning stages.
Interferometric gravitational wave detection at frequencies between $0.1\,\mathrm{mHz}$ and $1\,\mathrm{Hz}$ should be achieved with the Laser Interferometer Space Antenna (LISA) [23], a space-based interferometric GWD with several million kilometer long arms in a triangular configuration, which is planned to launch in the 2030s.

1.2. Laser requirements for gravitational wave detectors

The sensitivity of interferometric GWDs depends on several parameters such as their arm length, the seismic isolation of the interferometer end mirrors, called test masses, or the laser power. The laser system is a necessary sub-system for an interferometric GWD, which has to be carefully designed to not degrade the detectors sensitivity. A laser source for GWDs has to operate in continuous wave mode. This section will focus on the requirements that laser sources for GWDs have to fulfill besides that. It will be described how the laser power, beam profile and laser noise couple to the detector's performance and what techniques are used to optimize theses laser characteristics. The description exposes the challenges in laser development for gravitational wave detectors and therewith motivates the experimental work on high power lasers for gravitational wave detectors that was performed within in this thesis.

1.2.1. Laser power

For a basic understanding the impact of the laser power on the GWD readout can be visualized by a simple Michelson interferometer contrast shown in Figure 1.2. The higher the laser power the steeper is the power per phase slope, which leads to an increase of the gravitational wave signal size on the interferometer output. The differential arm length changes and thus phase changes in for example aLIGO are detected with the DC readout scheme [24]. This means that the interferometer is locked close to the dark fringe and just a small amount of laser power is detected at a photodetector. The signal slope is especially small at this point, which makes it even more important to have high laser power in the interferometer. The maximal laser power is nevertheless limited, as also fundamental noise sources scale with the laser power.
A fundamental sensitivity limitation for the detection of gravitational waves results from the quantum nature of light and is called standard quantum limit (SQL). The quantum noise of a GWD is composed of the photon shot noise and the quantum radiation pressure noise. Both noise sources result from the Poisson distribution of photons in a laser beam that get important in different ways. The photon shot noise directly describes the uncertainty in power on the detector readout. All changes in power will be read out as possible phase changes and thereby mask the gravitational wave signal. The gravitational wave strain equivalent of the relative photon shot noise h_{shot} in the detector scales with the laser power as described in [25],

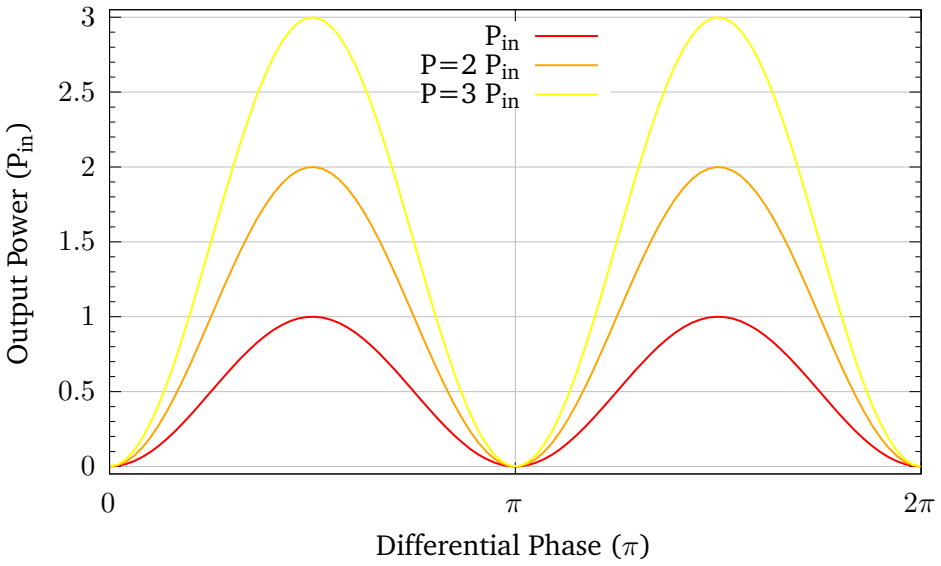

Figure 1.2.: Contrast of a simple Michelson inteferometer dependent on the input power P_{in}. The signal slope increases for increasing laser power.

and is given as an ASD in units $1/\sqrt{\text{Hz}}$:

$$h_{\text{shot}}(f) = \frac{1}{L}\sqrt{\frac{\hbar c\lambda}{2\pi P_{\text{in}}}}. \tag{1.1}$$

This equation assumes a simple Michelson interferometer as detector. Here f describes the measurement frequency, L the interferometer arm length, $\hbar$ the reduced Planck constant, c the speed of light, λ the laser wavelength and P_{in} the laser power that is injected to the interferometer. Hence, the relative photon shot noise in the interferometer decreases when the laser power is increased, independent on the measurement frequency.
The quantum radiation pressure noise is produced by the back-action of the interferometer's suspended test masses to the varying radiation pressure that the laser beam's Poisson distributed photons induce to the test masses. The test mass movement causes a phase fluctuation which turns into power fluctuations at the interferometer output. Hence, the gravitational wave equivalent strain of the quantum radiation pressure noise h_{rp} in the detector also includes the test mass mass m and is derived by [25]:

$$h_{\text{rp}}(f) = \frac{1}{mf^2L}\sqrt{\frac{\hbar P_{\text{in}}}{2\pi^3 c\lambda}}. \tag{1.2}$$

As the photon shot noise, it is given as ASD in units $1/\sqrt{\text{Hz}}$. The quantum radiation pressure noise scales with $1/f^2$ and is thus the dominating quantum noise contribution at low frequencies. In contrast to the relative photon shot noise it increases with increasing power.
The quantum noise limit for a specific parameter set is given by the quadratic sum of the photon shot noise and the quantum radiation pressure noise. Figure 1.3 shows the corresponding curves plotted for a simple Michelson interferometer with an arm lengths of $L = 4\,\text{km}$, a test mass mass of $m = 40\,\text{kg}$, a laser wave length

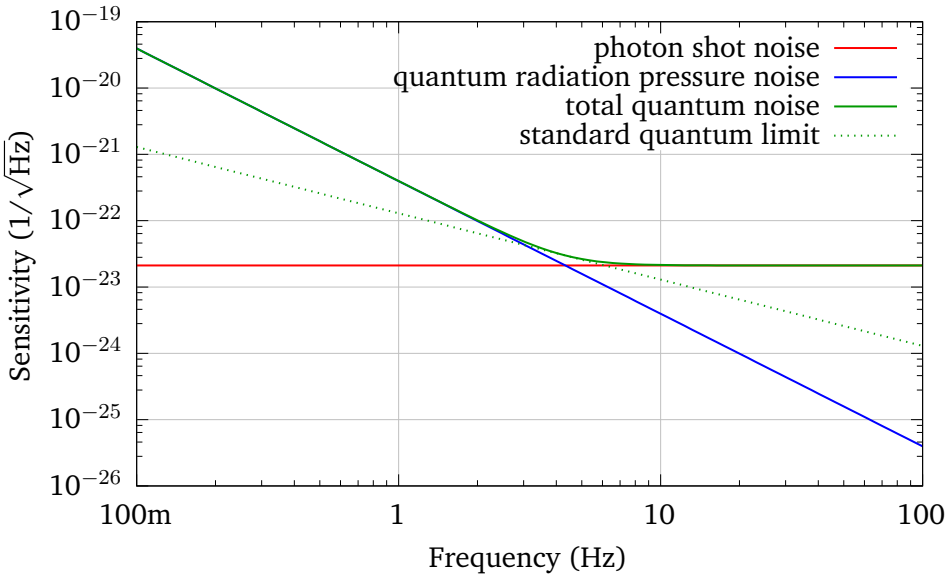

Figure 1.3.: Quantum noise contributions for a simple Michelson interferometer with an arm lengths of $L = 4\,\text{km}$, a test mass mass of $m = 40\,\text{kg}$, a laser wave length of $\lambda = 1064\,\text{nm}$ and a laser power of $750\,\text{kW}$. The SQL gives the classical limitation in a given detector environment.

of $\lambda = 1064\,\text{nm}$ and a laser power of $750\,\text{kW}$. The contributions of the relative photon shot noise and quantum radiation pressure noise vary when the power is changed. The SQL for a certain interferometer arm length describes the optimal sensitivity for each frequency, which is achieved by optimizing the laser power such that the relative photon shot noise and the quantum radiation pressure noise are equal. It is derived by inserting the frequency dependent optimal power into the total quantum noise equation. The gravitational wave strain equivalent of the SQL in a detector as ASD in units $1/\sqrt{\text{Hz}}$ is then derived by [25]:

$$h_{\text{SQL}}(f) = \frac{1}{\pi f L}\sqrt{\frac{\hbar}{m}}. \tag{1.3}$$

It can be pointed out here that the SQL does not depend on the laser wavelength but only the interferometer arm length and test mass masses. The SQL gives the classical sensitivity limitation for a given detector configuration. Non-classical approaches are needed to overcome this limitation, as described in the following. A more detailed description and calculation of the SQL can be found in [25].
The described quantum noise is calculated for simple Michelson interferometers but the interferometric GWDs are more complex than that. An overview of the additional components in a GWD is depicted in Figure 1.4. The power build-up in the power recycling cavity [25–27] is changing the effective input power and the signal recycling cavity enhances the gravitational wave signal in a certain frequency range by tuning the detector bandwidth [25, 27, 28]. The round trip number of the arm cavities [25] can be described as an effective arm length increase and the detector response causes an increase of the relative shot noise curve at high frequencies [27]. In addition the classical quantum noise limitation can be reduced for example via non-classical vacuum squeezed states of light that are injected from

the interferometers dark port [29].
All those effects have to be considered when defining the laser power requirement. Finally the chosen power level depends on the aimed measurement frequency band

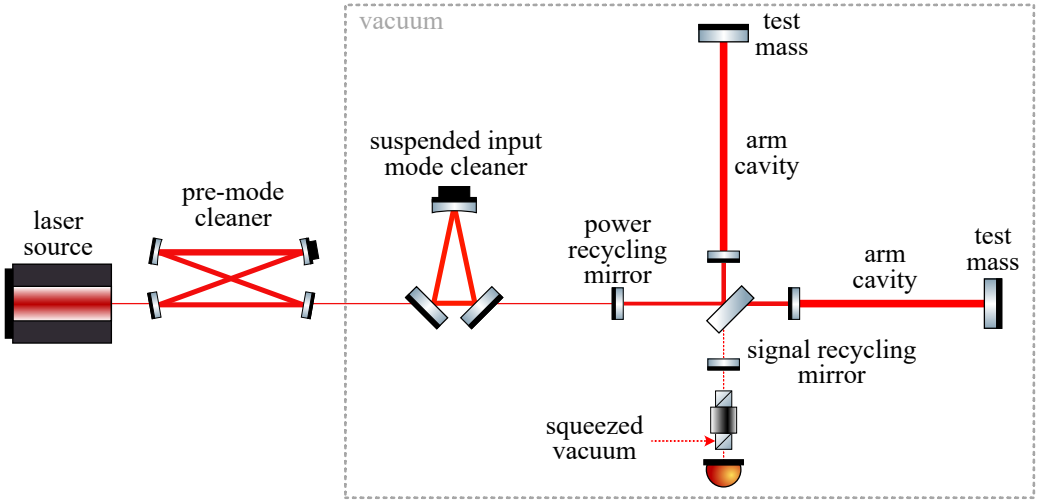

Figure 1.4.: Simplified schematic of a GWD. Depicted are the mode-cleaners, the power and signal recycling mirrors, the arm cavities and the injection port for squeezed vacuum.

and the detector configuration. aLIGO and Advanced Virgo aimed for $200\,\mathrm{W}$ of laser powers before the mode-cleaners in order to reach their design sensitivities [2, 3].
To reach higher sensitivities in upgrades of the second generation detectors and the third generation detectors, the limiting noise sources have to be identified and suppressed. The aLIGO design sensitivity is limited by seismic noise and suspension thermal noise at frequencies below about $8\,\mathrm{Hz}$, by radiation pressure noise at frequencies below about $40\,\mathrm{Hz}$, by coating Brownian thermal noise below about $300\,\mathrm{Hz}$ and by photon shot noise at higher frequencies [30]. The named noise sources will be tackled by different methods in future GWDs. The contribution of seismic noise can be reduced when the interferometer is installed underground. This is proposed for ET and already implemented for KAGRA [31]. Quantum noise in general is and will be further reduced by the injection of a frequency depended squeezed state of light [29]. Suspension thermal noise and coating Brownian thermal noise can be reduced by a cryogenic cooling of the optics, especially the test masses, like it is installed for KAGRA and proposed for the potential aLIGO update LIGO Voyager [32], for ET [20] and for the second phase of the Cosmic Explorer project [22]. The influence of quantum radiation pressure noise can be decreased with improved test mass suspensions and higher test mass masses. Finally a higher laser power would increase the sensitivity where photon shot noise is limiting.
To obtain a large measuring band with high sensitivity, ET will split the measuring devices in high and low frequency interferometers [20]. The low frequency interferometers will operate at cryogenic temperatures to decrease the Brownian thermal noise contribution that would be limiting otherwise. This also requires a different kind of optics and therewith a longer laser wavelength. They will use laser powers up to only a few W, to further reduce thermal effects on the test masses and to lower the radiation pressure noise impact.

The high frequency detectors of ET will work at room temperature and stick with a wavelength of $1064\,\mathrm{nm}$. High power laser sources with powers in the order of $700\,\mathrm{W}$ will be required to have a low photon shot noise level and thus achieve the design sensitivities [20].
The Cosmic Explorer design involves high power laser sources at a wavelength of $1064\,\mathrm{nm}$ in the first design step and aims to switch to high power laser sources at a wavelength of $2\,\mu\mathrm{m}$ for the final design [22]. The present thesis is concerned with laser sources for the coming updates of the second generation detectors and the high frequency detectors of the third generation of GWDs, all operated at a wavelength of $1064\,\mathrm{nm}$.

1.2.2. Relative power noise

Fluctuations in the power of a laser beam relative to the total laser power are described by the relative power noise (RPN). The coupling of the RPN to the output of a Michelson interferomter is negligible for a Michelson interferometer with symmetric arm length due to the common mode rejection of the interferometer. The real GWD interferometer arms have small asymmetries. For example deviations in the coating of the arm cavity substrates within the manufacturing tolerances lead to differences in reflectivities and the arm cavity storage time [33]. But also, the intended mismatch for the DC readout results in an unequal optical path length. Dependent on the length difference the common mode rejection is reduced [34].
Hence, the RPN of the laser beam that is injected in a GWD couples to some extent into power fluctuations at the interferometer readout. Those fluctuations mask gravitational wave signals with a lower amplitude and thus limit the detection sensitivity. The requirement for the maximal acceptable RPN of the laser beam injected to the GWD interferometer is set by the transfer function from the RPN to the detectors output and designated design sensitivity. For example, in aLIGO a power stability of $2 \cdot 10^{-9} 1/\sqrt{\mathrm{Hz}}$ at a measurement frequency of $10\,\mathrm{Hz}$ is required for the laser beam that enters the interferometer to reach the design sensitivity [35]. Also at very high frequencies in the MHz regime a low power noise is required to ensure a clean sideband modulation needed for the interferometer control [34]
The RPN of a laser beam can be divided into two parts. First the technical noise, which can for example occur from distortions in the laser resonator or noise of electrical power supplies for the laser. Technical noise can be suppressed by passive filtering and active feedback control loops. Intrinsically low noise seed lasers are used to avoid the need of a high actuation bandwidth. Mode-cleaner cavities that are installed between the laser system and the interferometer as well as the coupled cavity of the power recycling mirror and the arm cavities passively suppress the laser power noise between their pole frequency [36] and free spectral range (FSR) [37, 38].
The power can be maximally actively stabilized until it reaches the second RPN contribution, which is the relative shot noise on the power sensor used for the stabilization. The relative shot noise on the sensor is here given as power spectral of the relative power noise RPN_{SN} at measurement frequencies f:

$$RPN_{SN}(f) = \frac{2h\nu}{\bar{P}}. \tag{1.4}$$

Here h represents the Planck constant, ν the laser frequency and $\bar{P}$ the mean laser power. Hence, the limitation for power stabilization is given by the laser power that can be detected on a photo sensor.
For example, in aLIGO a cascaded power stabilization system is used. A pre-stabilization with one photodiode as sensor is performed at the laser preparation. In addition a photodiode array is used as in-vacuum sensor [37]. The array consists of four in-loop and four for out-of-loop photodiodes to increase the detectable laser power and by that decrease the shot noise limitation of the power stabilization.
New power stabilization techniques like the optical AC coupling [39] or indirect power sensing over for example radiation pressure noise [40] are investigated to allow a stronger suppression of the technical relative power. A power noise stabilization to noise levels below the shot noise of a photo detector is only possible with non-classical elements [41].

1.2.3. Laser beam profile and polarization

The transversal laser mode purity of laser sources for GWDs directly effects the amount of power that is injected into the interferometer, as higher order laser modes are filtered at resonators in the beam path [42]. aLIGO, for example, uses a pre-mode-cleaner [38, 43] directly behind the laser source and a input mode-cleaner which is installed in-vacuum [38]. Both of them are designed to be only resonant for the fundamental Gaussian laser mode. Therefore, the suppression of higher-order modes (HOMs) in transmission of the resonators is mainly defined by their linewidths and the HOM spacing, that is determined by the round-trip Gouy phase of the mode-cleaner cavity. A high content of HOMs in the laser beam would cause losses of laser power at the mode-cleaners. Therefore, the requirement for the HOM content is implicated in the power requirement before the mode-cleaners compared to the power behind the mode-cleaners.
Nevertheless, even with very high available laser powers it is desired to have a small HOM content, as the HOM power at the mode-cleaner dark ports cause an increased shot noise on the Pound-Drever-Hall sensors needed for the cavity locks [44]. Additionally, the mode purity in transmission of the mode-cleaners is limited by the HOM suppression of the cavities and the eigenmode quality of the resonators itself which can be distorted as described in Section 3.1.5 of [37]. The resulting residual HOM content behind the mode-cleaners can further couple to the interferometer and cause an increased shot noise in the power recycling cavity and the arm cavity Pound-Drever-Hall sensors, which would degrade their reachable stability.
Also polarization impurities would cause an impact on the usable laser power. Light that is not in a defined polarization would be filtered at Faraday isolators in the laser system or at the input mode-cleaner and thus also reduce the laser power that is injected to the interferometer.
Fluctuations in the laser beam profile and polarization have to be considered as especially critical as they induce an increased laser power noise in transmission of Faraday isolators and resonators.

1.2.4. Relative beam pointing noise

The relative beam pointing noise of a laser beam describes fluctuations in the beam position and beam angle relative to the optimal alignment. Hence, they can be treated as a fluctuation on the HG_{10} and HG_{01} mode content at the mode-cleaner

cavities as described in [45]. The relative beam pointing noise can origin at different points of the optical layout from a GWD. It is produced for example by moving optical surfaces due to vibrations on the optical tables, temperature variations or unstable mounting.
Relative beam pointing noise is partially suppressed by the mode-cleaner cavities. But simultaneously, it is converted to RPN behind the mode-cleaner cavities, which couples to the GWD interferometer readout like described in 1.2.2. The architecture of the second and third generation GWDs reduces a coupling of this power noise to the interferomter readout, as the last power stabilization components are located in-vacuum behind the input mode-cleaner and are seismically isolated. Nevertheless, beam pointing noise that occurs behind the mode-cleaners couples to the interferometer output through asymmetries in the interferometer arms.
High relative pointing coming from the laser preparation is avoided by the use of highly stable optical components, a stable room temperature, passively seismically isolated optical tables as well as a thoughtful design of the water-cooling systems. A further reduction of the coupling from beam pointing could for example be reached by an active beam pointing control. The coupling from relative pointing noise through the transition between the input optics [46] and the in-vacuum components could for example be improved by using fibers instead of periscopes. Research in this direction is presented in Section 4.2 of this thesis, in which the transportation of a high power laser beam in a hollow core fiber is investigated.

1.2.5. Laser frequency noise

The frequency noise of a laser beam arises, for example, from instabilities of the laser resonator. In an ideal Michelson interferometer with equal arm length, frequency noise would not couple to the readout due to the interferometers common mode rejection [47]. The frequency disturbances of a laser beam would have the same travelling time in both arms of the interferometer and cancel each other at the dark output port. As described in Section 1.2.2 the interferometer arms are not perfectly symmetric in real GWDs. Hence, laser frequency noise shows up as differential phase fluctuations on the interferometer beam splitter and thus couples as power fluctuations in the interferometer readout. Furthermore, frequency noise can couple through scattered light that interferes with the main laser beam or through higher order modes that are not resonant in the arm cavities but couple in the interferometer output due to mismatches. In both effects big path length differences and therewith a frequency noise coupling appears [47, 48].
In order to avoid high couplings to the interferometer readout from laser frequency noise, a low noise seed source is chosen, which is then further stabilized in multiple steps similar to the laser's relative power noise, as described in Section 1.2.2. For example in aLIGO the laser frequency is pre-stabilized to the length of an stable, in-vacuum, rigid spacer reference cavity in a first step. Next it is stabilized to the input mode-cleaner and finally to the length of the coupled cavity, formed by the power recycling mirror and the arm cavities of the interferometer [47]. It is necessary to stabilize the laser frequency in several steps to enable an initial interferometer lock before the coupled cavity's length can be used as final frequency reference. In addition passive stabilization of the frequency noise is performed by the filtering of the mode-cleaners as well as the coupled cavity formed by the power recycling mirror and arm cavities above their pole frequencies [36] and up to their FSR fre-

quency [37, 47].
The much longer arms of ET and Cosmic Explorer, will complicate a final stabilization to the common arm length in future detectors and a higher frequency stability of the light entering the power recycling cavity will be needed. A detailed description of the frequency noise coupling in aLIGO is given in [47]. Here also the current stabilization system and a proposal with two suspended mode-cleaners for the next generation is provided.

1.3. Laser concepts for gravitational wave detectors

The stringent requirements on the GWD laser characteristics [35] in combination with the high laser power as both stated in Section 1.2, make the development of a suitable laser systems challenging. There are no commercial laser sources available that fulfill all the requirements. Thus laser systems that consist of several stages for stabilization and power amplification were developed for the now running GWDs and have to be developed for the future ones.
In this section two options to generate low noise high power laser systems are presented. The first part concentrates on laser systems based on laser amplifiers and the second part on the coherent beam combination technique as an option to further increase the laser power. The systems that were developed and tested within the scope of this thesis are based on the technologies that are presented in this section.

1.3.1. Laser amplification

All second generation GWDs use low power, continuous wave non-planar ring oscillator (NPRO) lasers as seed laser source, as they have a narrow linewidth in the kHz regime, good inherent noise properties with an operated noise eater and a high fundamental Gaussian mode content [49, 50]. Additionally there are mirror substrate materials and photo detectors available that work very well with the provided laser wavelength of $1064\,\mathrm{nm}$. As the NPRO lasers only delivers up to $2\,\mathrm{W}$ of output power, low noise laser amplifiers are used to increase the laser power up to the levels needed for the use in GWDs.
Current and past GWDs use solid-state or fiber laser amplifier systems. In this subsection first the basic concept of laser amplification will be described. Following from that, an overview of solid-state and fiber laser amplifier systems will be provided and the limitations for each will be discussed.

Concept

A very simple schematic of a laser beam that is amplified by a laser amplifier is shown in Figure 1.5a. The seed laser beam that needs to be amplified is guided through a laser active medium, which can be based on different materials, like for example gases, semi-conductors, solid-states or glass fibers. The laser active medium must be a three or more energy level system with an energy difference between the higher laser levels that matches the seed lasers wavelength. An energy level picture on the example of neodymium doped yttrium orthovanadate (Nd:YVO_4) crystals is shown in Figure 1.5b [51]. The needed population density in the upper laser level is obtained via absorption that is generated with a pump laser at a wavelength that is matched to the energy difference between the the upper laser level and the ground state.
The seed laser beam then triggers a stimulated emission process in the active medium due to which more photons at the seed wavelength are generated. The new generated photons have the same beam characteristics as the ones of the seed beam, which means that the beam quality of the seed beam as well as the laser frequency can be kept in this process. The conversion between the two lower energy levels happens without optical emission. A detailed description of laser amplification and Nd:YVO_4 can be found in chapter 1 and 2 of [52].

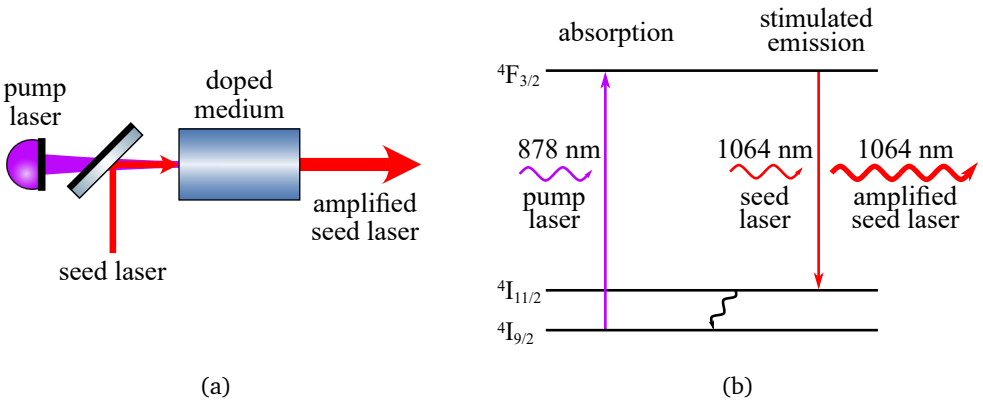

Figure 1.5.: a) Basic principle of laser amplifiers. A seed laser beam passes the doped medium. The pump laser causes an absorption in the medium and the seed laser beam the stimulated emission at the seed wavelength.
b) Energy level diagram of Nd:YVO_4. A population inversion between the upper and lower laser state is generated via absorption of the pump light. The seed laser beam triggers a stimulated emission at its wavelength and thereby gets amplified. The transition between the two lower laser states happens without optical emission.

The maximal power level generated with laser amplifiers is given by the available pump and seed power, the volume of the active medium as well as the properties of the doping. What is limiting the systems that are used in GWDs will be described in the following.

Solid-state laser amplifier systems and their limitations

Most high power laser systems, either for scientific or industrial use, are based on a cascaded system of laser amplifiers or on injection-locked laser amplifiers in an oscillator configuration. The choice of the amplifier material thereby depends mainly on the seed laser wavelength that needs to be amplified. Different configurations of solid-state laser amplifiers are and were used in GWD laser systems over years. The amplifiers work reliable and keep the frequency stability of the NPRO seed laser at most frequencies [53–56].
The maximal power level that can be reached with the solid-state laser amplifiers suitable for GWDs is limited by different parameters. One of them is the available material for amplifiers at the requested wavelength itself. The possible doping, the size of the material and the efficiency given by the quantum defect and losses theoretically define the reachable power level if the available pump and seed power is not restricted. Additionally to the theoretical material parameters, other effects can limit the amplifier's output power. For example high thermal gradients induced by a high pump and seed power at small beam radii can cause losses, deformations of the beam profile or even break the crystals. Also an inhomogeneous saturation of the amplifier will cause a deformation of the beam profile. Hence, it will decrease the available power in the Gaussian laser mode [52, 53].
Up to now laser systems based on solid-state laser amplifiers that are suitable for

gravitational-wave detectors and have a maximal power in the $200\,\mathrm{W}$ regime were presented. The laser system that was developed for aLIGO used four neodymium-doped yttrium aluminum garnet (Nd:YAG) crystals in an injection locked oscillator configuration with a neodymium-doped yttrium orthovanadate (Nd:YVO_4) solid-state pre-amplified NPRO laser beam as seed. This system could deliver up to around $200\,\mathrm{W}$ of laser power [57]. The downside of this system was it's complexity and the high cooling demand and therefore high water flow, needed because of the low pump efficiency of just $30\,\%$, which led to vibrations on the optical table.
Those problems led to a change in the system for the 3rd GWD network's observing run. There the same pre-amplified seed beam was used and then amplified by a new version of a Nd:YVO_4 solid-state laser amplifier [54, 56]. The available power was reduced to $70\,\mathrm{W}$ by this, but the system got less complex and needed less cooling. Due to problems, like scattering at point absorbers in the interferometers, the aLIGO detectors were not operated with more than $40\,\mathrm{W}$ at that time anyway [34].
A laser system with a NPRO seed laser and three cascaded Nd:YVO_4 solid-state laser amplifiers, with an output power of about $195\,\mathrm{W}$ will be presented in Section 3.1 of this thesis. The laser system was developed to investigate the influence of the chosen amplifiers on the seed beam's shape and noise properties as well as to identify possible limitations. The results are published in [55] and build the basis for the laser system that will be used in the 4th aLIGO observing run (O4). A prototype of the O4 system was installed in a test and training laboratory at the aLIGO Livingston detector site and will also be presented in Section 3.1. The system consists out of a NPRO laser as seed, followed by two cascaded Nd:YVO_4 solid-state laser amplifiers, and delivers up to $140\,\mathrm{W}$ of output power [56].

Fiber laser amplifier systems and their limitations

A similar, if not better, beam quality and noise behaviour compared to solid-state laser amplifier systems can be obtained with fiber laser amplifiers. Fiber laser amplifiers have several advantages compared to solid-state laser amplifiers. The laser and pump light can be guided over a long distance in a small mode area which results in a higher pump efficiency compared to solid-state laser amplifiers. This also comes with a moderate heat distribution and thus a lower cooling demand. The resulting laser beam is nearly diffraction limited and its profile is given by the possible fiber modes and thereby well defined. Due to the fiber guidance, also less optical components are necessary which can reduce the system's complexity [58–60].
The main limitation for the amplification with fiber laser amplifiers is the stimulated Brillioun scattering (SBS). SBS describes an effect in which standing phonon waves that build up in the fiber cause scattering of the amplified light and thus an increase of the laser beams MHz RPN [61]. SBS scales with the fiber geometry and length as well as the laser power guided through the fiber. The effective fiber length for SBS can be reduced for example by inducing a high temperature gradient along the fiber [62]. Additionally the SBS threshold can be lifted with backwards pumping, as this induces a higher power gradient than forward pumping, and thus decreases the region in the fiber with power levels that can induce SBS [63].
The so far presented fiber laser amplifier systems at a wavelength of $1064\,\mathrm{nm}$ that are build to fulfill the requirements of GWDs have maximum output powers in

the 200 W regime [59, 60, 62]. All those systems are based on ytterbium doped double-clad fibers and showed a similar, partly even better, beam quality as solid-state laser amplifier systems.
Proof of principle experiments showed already laser powers of up to 365 W [62, 64] and it seems to be promising that even higher laser powers are possible with the shown technology. It was also shown that systems with new kinds of fibers can deliver more than 350 W and the development in this direction is ongoing [65, 66].
The biggest disadvantage of fiber laser amplifiers so far was their reliability and stability. Back reflections can cause severe damage on fiber laser amplifiers and the fiber processing and component development is complex. Nevertheless, a lot of development in this direction happened over the last years. The fiber laser amplifier laser systems are shown to work long-term stable and the manufacturing got much more reliable [60]. Thus, laser systems based on fiber laser amplifiers became a promising option as laser source for future ground based GWDs. It is still open to test these fiber laser amplifier systems in a gravitational wave detector laser system environment including active and passive stabilization.

1.3.2. Coherent beam combination

The design sensitivity to gravitational wave signals will increase with coming generation of GWDs. As described in Section 1.2.1, at high measurement frequencies this is related directly to the needed laser power, which thus also has to be increased. The maximal output power of cascaded laser amplifier systems is limited to several hundred watts as described in Section 1.3.1. As the power recycling and arm cavity finesse is limited, the coherent combination of several laser beams is investigated as a new technology to increase the laser power.
The basic concept of the coherent beam combination (CBC) as well as different coherent beam combination laser systems will be described in this section.

Concept

The coherent combination of laser beams describes a technique which is used to add the power of several laser beams via constructive interference. For this the to-be-combined laser beams have to be spatially superimposed and spectral coherent on the combination point. Figure 1.6 depicts the basic concept of a coherent beam combination assembly on the example of two laser beams beams of the same power that are combined on a 50:50 beam splitter. There are also other combination schemes as for example the coherent polarization beam combination [67], which are not used in this work and are therefore not described further. In the shown example beam 1

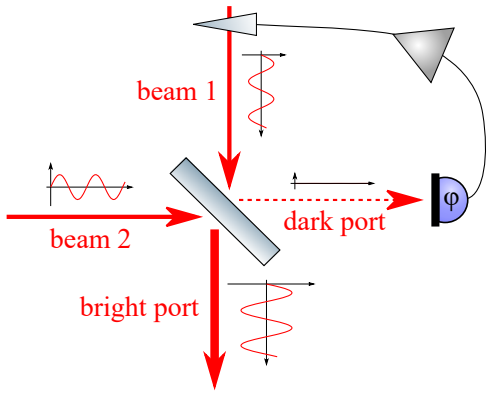

Figure 1.6.: CBC of two laser beams on a beam splitter. The differential phase and frequency are controlled in a feedback control loop.

and beam 2, are guided to the beam splitter from two directions. Without coherence between the two beams, each of them is divided into two equal parts by the beam splitter. One part is reflected and the other part transmitted.
The first requirement for a successful combination of the two laser beams is a superimposition of the laser beams with a good spatial overlap. The second requirement is the spectral coherence. Both together make an interference between the two laser beams possible.
In order to produce a dark output port with almost no laser power and a bright beam splitter port, also called combined port, with almost all the laser power of both beams, the frequency of the two incident beams has to be equal and their phase has to be matched in order to keep the interference at a steady level. In the schematic, a sensor is shown on one output port of the beam splitter, which measures the phase and frequency difference between the interfering beams. The obtained signal can be used as an error signal for a feedback control loop that feeds back to a phase and frequency shifter which actuates on the phase and frequency of beam 1 to match it to the phase and frequency of beam 2 in a feedback control loop.
As the coherent beam combination technique is based on the interference between the laser beams, it is applicable for laser systems at all wavelengths.

Laser systems based on the coherent combination of laser beams

The coherent beam combination of laser beams can be obtained in two different methods. The first method is the tiled aperture combination, where an array of laser beams is combined in the far field. This method can be used for various industrial and scientific applications where a very high continuous wave or pulsed laser power is needed but the laser requirements on the beam profile in the near field can be neglected. Laser systems in the kW level based on the tiled aperture coherent beam combination of several laser beams, where presented in various publications [68–71].
Systems that need a coherent beam combination at the near field or at every position along the beam propagation direction can be based on the filled aperture combination method. This is needed to couple efficiently to an optical cavity or interferometer. In the filled aperture method a beam combining element, like the beam splitter shown in Figure 1.6 in Section 1.3.2, is used to ensure a coherent combination in the near field and, with a good spatial alignment between the beams, also in the far field.
Laser systems based on the filled aperture coherent beam combination of laser beams are highly considered for the future ground based GWDs Cosmic Explorer and ET, as it should be possible to add the power of low noise laser systems in this scheme, while the beam quality of a single beam is preserved.
Up to date most coherent beam combination experiments with the aim to be used in GWDs where performed with two amplified beams from one seed source. In 2016 a group in the ARTEMIS laboratory in France has presented a filled aperture coherent beam combination laser system designed to be used in the Advanced Virgo GWD [72]. They coherently combined two $40\,\mathrm{W}$ laser beams provided by two fiber laser amplifiers in the arms of a Mach-Zehnder interferometer with a combination efficiency of $96\,\%$. Another filled aperture coherent beam combination laser systems with low laser noise and good beam quality was demonstrated

by a cooperation of the Max Planck Institute for Gravitational Physics Hanover and the Laser Zentrum Hannover e.V. [73]. The experimental layout also included two fiber laser amplifiers in the arms of a Mach-Zehnder interferometer. Here two times $10\,\mathrm{W}$ where combined with a combination efficiency of 95-$97\,\%$ and a noise behaviour similar to a single amplifier.
The so far presented coherent beam combination systems where analyzed regarding the reachable power level and partly their free-running laser noise. For an integration into GWDs it is important to understand how the coherent beam combination control loops influence the power and frequency noise and if it affects the possibility to stabilize those. Therefore, a PSL based on the coherent beam combination of two laser beams from the same seed source amplified by solid-state laser amplifiers in a Mach-Zehnder interferometer configuration is presented in Section 3.2. The resulting $100\,\mathrm{W}$ laser beam was precisely characterized in order to reach a complete picture about possible downsides of the coherent beam combination process.
So far, no coherent beam combination laser systems were presented that exceed the laser power available by sequential amplification of a laser beam. A first step towards the high laser powers required for future GWDs like ET was performed with the laser system that will be presented in Section 3.3 of this thesis. The system is based on two high power fiber laser amplifiers in both arms of a Mach-Zehnder interferometer. This experiment was performed in a cooperation with and located at the Laser Zentrum Hannover e.V.. Here a $400\,\mathrm{W}$ coherent combined beam could be obtained. The system is characterized regarding the combination efficiency and free-running laser noise, and the results are published in [74] and [75]. A follow up experiment, in which two laser beams amplified by fiber amplifiers will be combined in a PSL, is designed on the basis of the results generated in Section 3.2 and Section 3.3. The system is already under construction at the Albert Einstein Institute Hanover.
A coherent beam combination experiment with two independent laser sources was presented in a Master thesis performed at the Albert Einstein Institute Hannover [76]. Here two $5\,\mathrm{W}$ laser beams were combined to a $9\,\mathrm{W}$ beam in a proof-of-principle experiment. Another proof-of-principle coherent beam combination of independent laser beams was performed in the scope of the present thesis and will be presented in Section 3.2. The reseaurch focus in this experiment is on the combination of different laser powers with a variable beam splitter as combining element. The two single laser beams had laser powers of $70\,\mathrm{W}$ and $100\,\mathrm{W}$ and could be combined to a $145\,\mathrm{W}$ laser beam.
One approach to reach even higher power levels than available from two amplified laser beams is to combine more than two laser beams. In Section 4.1 a proof-of-principle coherent beam combination of three laser beams, with a bow-tie resonator as combining element, is described. The three laser beams all origin from a single laser source and are amplified by solid-state laser amplifiers. In the first tests of this system three $5\,\mathrm{W}$ laser beams were combined to a $11.3\,\mathrm{W}$ laser beam. The losses can be traced back to the HOM content of the three input beams, which are not combined in this scheme, and first noise measurements are presented.

2. The aLIGO pre-stabilized reference system environment

The advanced Laser Interferometer Gravitational-Wave Observatory (aLIGO) PSL was developed in a cooperative effort of the Laser Zentrum Hannover e.V. and the Albert Einstein Institute in Hanover. One each was installed in the GWDs at Hanford and Livingston. An additional complete PSL at the Albert Einstein Institute served as a reference for the running systems at the aLIGO sites until the third observing run. The system contains the laser source as well as the components for the passive and active pre-stabilization of the laser beam parameters. Part of the PSL is the diagnostic breadboard (DBB) which can be used for a fully automated characterization of all important laser parameters. It was developed at the Albert Einstein Institute in Hanover as well and is also part of the reference PSL system in Hanover. For simplicity, the environment of aLIGO's pre-stabilized reference system in Hanover will also shortly be called reference system in this thesis.
With changing from an injection-locked high-power oscillator to a single-pass solid-state laser amplifier configuration during the third observing run (O3) of the gravitational wave detector (GWD) network, the aLIGO laser system has gotten less complex. Hence, it is no longer needed to keep an exact copy of the complete laser system in Hanover. Nevertheless, the components for the pre-stabilization are the same as for aLIGO, which makes the reference system an ideal environment to test new high power laser systems with respect to their suitability for gravitational wave detectors. The output laser beam of the reference system can in addition be perfectly used to test components that could be installed in the input optics part of a GWD [46]. Therefore, the reference system also includes a second DBB, which is used to characterize the PSL output laser beam.
For that reasons, a large part of the experimental work performed for this thesis is performed in the reference system environment. This chapter will briefly describe the reference system environment and the included diagnostic breadboards and thereby will serve as a reference for the experimental chapters of this thesis. A more detailed description of the aLIGO PSL and thus the reference system can be found in [37, 38, 57]. The diagnostic breadboard is described in [77] and [37].
The chapter starts with the layout of the pre-stabilization components and the description of the seed laser system as well as the pre-stabilization control loops step by step. The complete stabilization schemes that are used in the aLIGO detectors will explained only briefly, as they aren't part of the reference system. Afterwards the diagnostic breadboard layout and measurements will be described.

2.1. PSL reference environment layout

Figure 2.1 shows a schematic overview of the pre-stabilization components of the aLIGO PSL reference system environment. For completeness, the layout also includes the summation points of additional stabilization loop control signals that

are generated in the aLIGO interferometers. The corresponding control loops will also be briefly explained in this section.

All subsystems of the PSL are controlled via the aLIGO real-time digital control

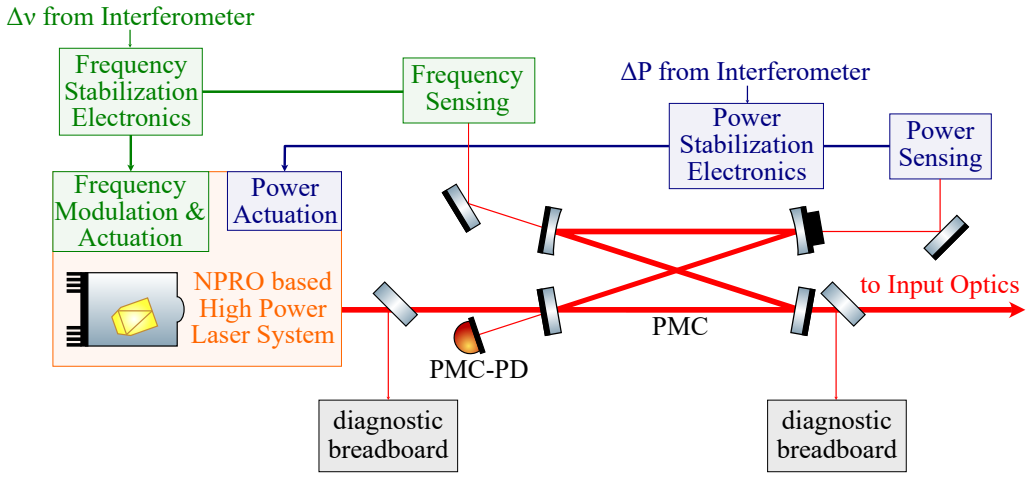

Figure 2.1.: PSL reference environment layout. The seed laser source is guided to the pre-mode-cleaner (PMC) for filtering. The two low power output ports of the PMC are send to the sensors used for the frequency and power pre-stabilization feedback control loops. Two DBBs are used to characterize the laser beam before and behind the PMC.

and data acquisition system (CDS) [78]. The CDS allows a remote control of the laser systems and, thus, also adjustments to the laser system while the GWDs are in observation mode. All electronic signals in the laser system, for example generated by power and temperature sensors or voltage drivers and filter electronics, are recorded by the CDS. Also digital control loops can be implemented on the laser system, for example to support existing analog control loops. At aLIGO the PSL is in a closed laser room, that is held at a constant temperature and not entered during while the detectors are in observing mode. Most electronics as well as the water cooling systems are located outsides of the laser room to prevent electronic or acoustic noise to couple in the laser noise. In the reference system only the water-cooling and the seed laser diodes and the corresponding electronics are located in separate rooms.

The seed laser source installed in the reference system is the so called enhanced Laser Interferometer Gravitational-Wave Observatory (eLIGO) frontend, which is a well known laser system that has proven its reliability in several systems [53]. A central optical component of the aLIGO PSL, and thus of the reference system is the so called aLIGO pre-mode-cleaner (PMC) [37, 38, 43]. The PMC provides two low power output ports for the power and frequency pre-stabilization as well as the stabilized main output beam [37, 57], which can be send to the GWD interferometer via the input optics subsystem [46]. In the reference system the output beam of the PMC can be used for other experiments. The PMC eigenmode also serves as an ideal geometry reference for the laser beam. All those named PSL reference system subsystems will be described further in the next subsections.

2.1.1. The enhanced LIGO frontend laser

The eLIGO frontend laser [53] is based on a master oscillator power amplifier (MOPA) system. It was used as laser system for eLIGO and GEO600 as well as a seed laser in the aLIGO PSL until the fourth observing run and is therefore also part of the reference system. It has proven its reliability over years and thus serves as excellent seed laser for the amplification or coherent beam combination experiments that are performed in the scope of this thesis.
A schematic overview of the frontend is depicted in Figure 2.2. All lenses that are

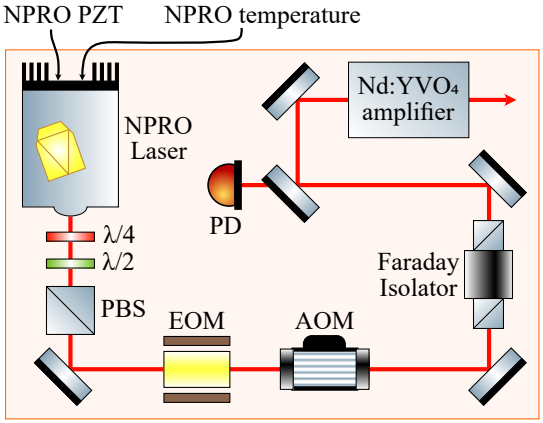

Figure 2.2.: The eLIGO frontend consists of a 2 W NPRO laser which is amplified up to about 35 W with a solid-state laser amplifier. The frontend frequency, phase and power can be controlled with several actuators.

used for mode shaping as well as some of the beam guiding mirrors are left out for simplicity. The laser beam from a 2 W NPRO laser is first polarization cleaned by a quarter-wave and a half-wave plate as well as a polarizing beam splitter. NPRO lasers are used for all gravitational wave detector laser systems that operate at a wavelength of 1064 nm, as they deliver a very good beam quality and noise behaviour to begin with [49, 50]. The linear polarized beam is then guided through an electro-optical modulator (EOM) and acousto-optic modulator (AOM), which can be used for frequency and power actuation, respectively. A Faraday isolator protects the NPRO laser from back reflections. The laser beam can be amplified to about 35 W by a Nd:YVO_4 solid-state laser amplifier. Four diodes at a wavelength of 808 nm with a maximum optical power of 60 W are coupled to the amplifier via fibers and used to pump the amplification process. All optical frontend components are located on an aluminum breadboard in a closed box to protect them from environmental influences. The water-cooling system needed to cool the amplifier head, the amplifier electronics and the pump diodes are located at a separate room to prevent acoustic noise or vibrations produced by them to couple to the laser noise. Also the pump diodes and their electronics are located in a different room.
The solid-state laser amplifier diodes are controlled via a Beckhoff system which allows for a remote control. The produced signals are further send to the CDS for monitoring. Also all other electronic signals produced in connection with the frontend, for example from temperature or flow sensors, are read out by the CDS. An analog and digital interlock system are used for fast and slow emergency shutdowns of the laser system, respectively.

2.1.2. aLIGO pre-mode-cleaner

The aLIGO PMC [79] is a bow-tie resonator with a round-trip length of $2.02\,\mathrm{m}$, a Finesse of 129 and a FSR of $149\,\mathrm{MHz}$ [38, 43]. Its main purpose is the passive filtering of the injected beam's spatial laser mode as well as the beam pointing and radio frequency (RF) laser noise [37, 38]. Furthermore the PMC serves as geometric reference for its injected and transmitted laser beam [38]. Its two low power output beams are send to the frequency and power pre-stabilization sensors as depicted in Figure 2.3 and Figure 2.4.
The PMC is protected from air fluctuations via a housing. The input and output mirror are flat and the additional two mirrors have a curvature of $-3\,\mathrm{m}$. In the original version of the PMC the two flat mirrors and one of the curved ones are glued directly to a rigid aluminum spacer. The second curved mirror is glued to a piezo-electric element (PZT) which is then glued to the spacer. Earlier it was assumed that the glue might out-gas which could negatively effect the PMC performance. Therefore, the PMC box's top is open in the reference system.
At the aLIGO detector in Hanford, Washington the PMC was replaced by the so called all-bolted PMC, with mechanically fastened instead of glued mirrors, during the third observing run [80]. The aim of this change is to avoid potential mirror contamination from the glue, ease the fabrication process and allow an easy mirror swap if necessary. This PMC will also be used in the new aLIGO laser system at both aLIGO sites for the fourth observing run and is already installed for a prototype of this system in the test and training facility at aLIGO Livingston, Louisiana. To date, there are no plans to exchange the reference systems PMC.
The PMC length, and therewith its resonance frequency, is stabilized to the laser frequency via the Pound-Drever-Hall locking scheme [44]. An EOM in the laser system imprints the needed phase modulation sidebands at a frequency of $35.5\,\mathrm{MHz}$ to the laser beam. A photodiode (PMC-PD) in reflection of the PMC is used as sensor. The photodiode signal as well as a local oscillator (LO) signal are send to an analog mixer. This mixer provides an error signal with a linear slope, which is amplified and filtered. The resulting control signal drives the PZT on one of the PMC mirrors, which actuates on the cavity length. A slow control of the PMC length via heat pads attached to the PMC aluminum spacer, extends the control range. It compensates for slow drifts of the laser frequency and thereby keeps the PZT in the middle of its control range. The analog locking electronics are controlled digitally via the CDS over digital-to-analog converters. The digital control is used to enable the lock, for automated re-locks as well as to adjust analog gains. For this purpose, all analog signals of the loop are read out by the CDS via analog-to-digital converters.
The main utility of the PMC is to filter higher order laser modes from the main laser beam. Therefore the PMC length is stabilized to be resonant to the Gaussian transverse electromagnetic $(\mathrm{TEM})_{00}$ mode of the laser beam. Due to the chosen round trip Gouy-phase of $1.75\,\mathrm{rad}$ the higher order laser mode resonance frequencies in the PMC are clearly separated from the TEM_{00} mode. Hence, if the PMC length is stabilized to be resonant for the TEM_{00} mode of the injected laser beam, all modes at frequencies outside of the resonance linewidth are suppressed. The Hermite-Gaussian $(\mathrm{HG})_{01}$ and HG_{10} mode are suppressed by a factor of 3969 [38]. The relative beam pointing can also be described as fluctuations to the first order TEM PMC eigenmodes. Hence, the mode filtering effect also applies for the laser beam's relative pointing noise. The theoretically expected suppression factor of 63 was proven to be valid in the reference system at and above Fourier frequencies of

20 Hz [38].
Above its pole frequency of 578 kHz and below its free-spectral range of 149 MHz the PMC also serves as passive low pass filter for the lasers relative power and frequency noise. This high frequency filtering is important as it increases the signal to noise ratio of MHz phase modulation sidebands that are imprinted to the beam with an EOM that is located behind the PSL [38]. In the aLIGO detectors, additional mode and noise filtering is provided by the in-vacuum input mode-cleaner [38].
In addition to its filtering effects, the PMC also serves as a reference for the beam geometry given by the PMC eigenmode. This ensures that changes in the laser system only require a realignment and mode matching of the laser beam to the PMC eigenmode, but do not change the beam path and shape behind it.

2.1.3. Power pre-stabilization

The active power stabilization for aLIGO [37, 57] is split in the pre-stabilization, also called first loop, and a second loop with an in-vacuum sensor as already mentioned in Section 1.2.2. The main components of the power pre-stabilization loop and their arrangement in the PSL is depicted in Figure 2.3. The pre-stabilization

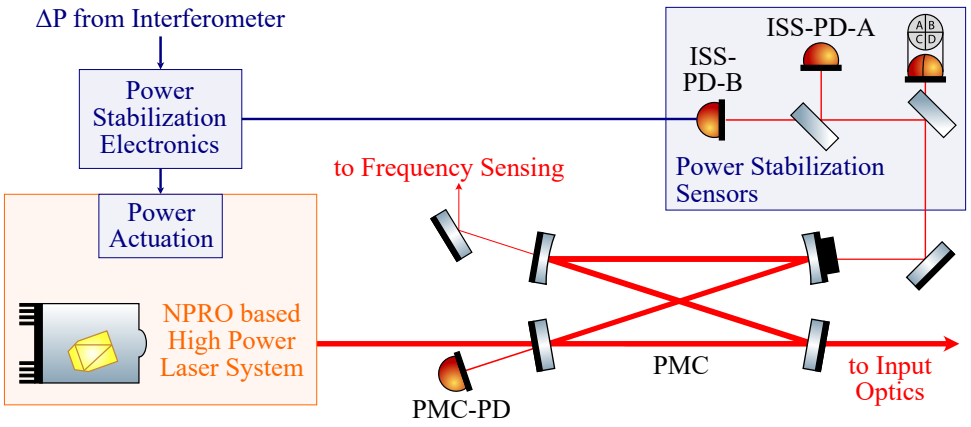

Figure 2.3.: PSL power stabilization layout. A set of photodiodes at one of the PMC's low power output ports are used as in-loop and out-of-loop sensors, respectively. The power correction is performed with power actuators in the laser system.

loop contains an in-loop and out-of-loop photodiode (ISS-PD-A and ISS-PD-B) that sense the power fluctuations at a pick-off beam from the PMC and can detect a laser power of up to 4 mW, which corresponds to a shot noise limitation of about $10^{-8} 1/\sqrt{\text{Hz}}$ [57]. Both photodiodes as well as a quadrant photodiode, that detects beam position changes, are located in a closed aluminum box to protect the sensors from stray light. The box also prevents air fluctuations or room light to couple in the signal. For this reasons also most of the beam path between the PMC and the box is en-housed in beam tubes.
The power fluctuations measured with the in-loop photodiode are filtered and amplified with analog electronics and the resulting control signal is send to a power actuator in the laser system. All electronic parameters and offsets can be controlled via the CDS. The power actuator can be an AOM, as it is used in the aLIGO PSL

[56, 57] or for example a current driver on an amplification stage [54], as it is used in one of the laser systems that are investigated in this thesis. As part of the first power stabilization loop, an additional low gain digital control loop can be used for a first power stabilization, which can help to adjust the parameters for the analog loop.
The second loops power stabilization sensor in aLIGO consists of an array of four photodiodes as in-loop and out-of-loop detector, each [37, 38, 81]. The array is located behind the input mode-cleaner in-vacuum and allows to measure more power in a quieter environment and thus to stabilize to a lower noise level. The signal is added in the error point of the PSL power stabilization electronics. Hence, the PSL's power actuator is also used for the second stage's stabilization. The second power stabilization loop is not part of the PSL itself and thus also not part of the reference system.

2.1.4. Frequency pre-stabilization

Similar to the power stabilization, also the active frequency stabilization is subdivided in different frequency stabilization loops [37, 38, 57]. The reference cavity displayed in Figure 2.4 serves as frequency reference for the pre-stabilization, or first loop. The reference cavity is a $203\,\mathrm{mm}$ long Fabry-Pérot cavity with a finesse

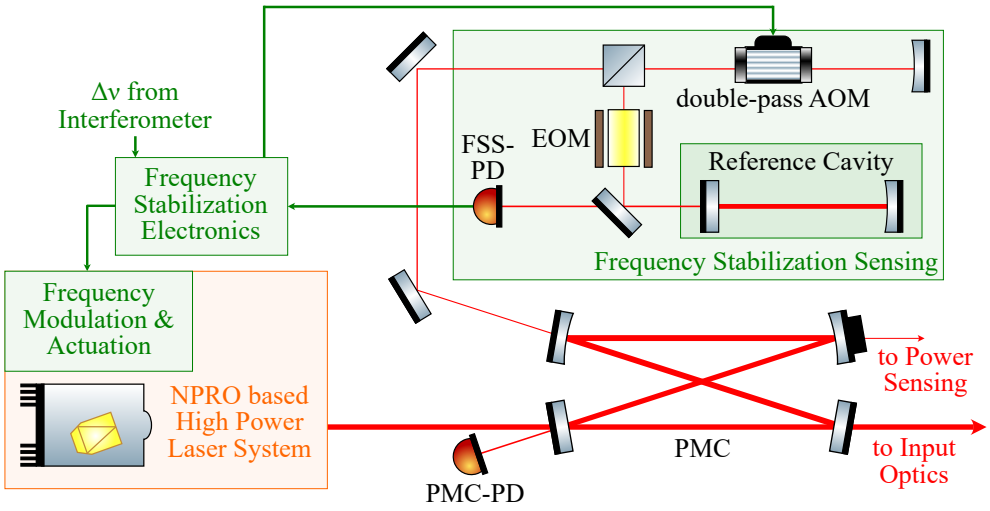

Figure 2.4.: A frequency pre-stabilization is realized by locking the laser frequency to the eigenmode of a monolithic reference cavity via the Pound-Drever-Hall scheme. The reference cavity is located at one of the PMC's low power output ports. A double-pass AOM is used to add frequency corrections from the interferometer's final frequency stabilization loop

of 9518 and a FSR of $736.5\,\mathrm{MHz}$. The two curved mirrors, with radii of curvature of $-0.5\,\mathrm{m}$, both, are optically contacted to a rigid fused silica spacer, which is installed on a single pendulum stage supported by a passive vibration isolation stack and eddy current dampers in a temperature controlled vacuum tank. The small thermal conductivity of fused silica in combination with a pressure below $10^{-6}\mathrm{Pa}$ allows for a very stable length and thus resonance frequency of the cavity [37, 38, 57].
The laser frequency is stabilized to the TEM_{00} eigenmode of this cavity via the

Pound-Drever-Hall locking scheme. An EOM in the frequency stabilization path hereby provides the needed $21.5\,\mathrm{MHz}$ phase modulation sidebands. A photodiode in reflection of the cavity (FSS-PD) measures a signal, which is then demodulated in an analog mixer with a LO signal at the sideband frequency. The resulting error signal is filtered and amplified with analog electronics. The so produced control signal is fed back to frequency modulators in the laser system.
In aLIGO as well as in the laser systems that will be presented in Chapter 3 of this thesis, the laser frequency is controlled with a PZT on the NPRO crystal, for actuation of the optical path length in the crystal, as slow and an EOM behind the NPRO laser, as fast frequency actuator, respectively. An additional control of the NPRO crystal temperature holds the PZT in the middle of its actuation range and thereby increases the range of the of the NPRO crystal length control.
The pre-stabilization is needed to allow a lock acquisition of the GWD interferometer. The final frequency stability in aLIGO is reached via a system of nested feedback control loops. First the laser systems frequency is stabilized to the input mode-cleaner and finally to the length of the coupled cavity, formed by the power recycling mirror and the arm cavities of the interferometer [37, 38, 47]. All frequency stabilization control loops work with the Pound-Drever-Hall scheme. An additional EOM before the input mode-cleaner is needed to imprint the needed phase modulation sidebands on the laser beam that comes from the PMC as they are out of the PMC linewidth and can therefore not be imprinted with the PSL's EOM before the PMC. The frequency corrections that are needed in addition to the pre-stabilization are added at the double-pass AOM that is also shown in Figure 2.4.

2.2. The Diagnostic Breadboard

The DBB is a tool developed at the Albert Einstein Institute in Hanover, that is used to fully automated, characterize a laser beam, with respect to its mode purity and noise properties [37, 50]. The aLIGO laser systems have DBBs installed which are used to measure the laser beam characteristics before the beam enters the PMC. The controlling and data acquisition can be performed via the CDS. Hence, regular measurements of the important beam parameters can be performed without entering the laser room at aLIGO. Thereby it can be easily verified if disturbances in the interferometer occur already in the laser system. Additionally, irritations in the laser parameters that indicate for example a degradation of components can be found fast in this way. Also stand-alone variants of the DBB are existing. They are computer controlled as well, but are usually used in smaller experiments, as they can't be controlled completely remote, which makes, for example, nightly measurements of all parameters impossible.
The reference system has one DBB to measure the beam properties ahead of and one to measure them behind the PMC, as it is indicated in the PSL layout schematic Figure 2.1 in Section 2.1. With this configuration not only laser systems that are completely integrated in the PSL can be characterized, but it also allows to use a very clean and stabilized laser beam to test optical components like amplifiers, as it will be presented in Section 3.1, or fibers, like the hollow core fiber that will be presented in Section 4.2.
The schematic layout of the optical components in the DBB is shown in Figure 2.5. The central component of the DBB is its three mirror ring cavity with a round-trip length of $420\,\mathrm{mm}$, a finesse of 356 and a FSR of $715\,\mathrm{MHz}$. It is needed for the HOM

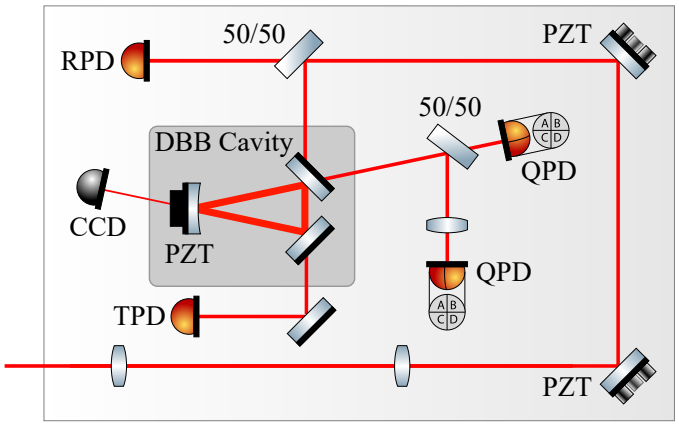

Figure 2.5.: The DBB is used for the characterization of the injected laser beam. The laser beams RPN, frequency noise, relative pointing noise and HOM content can be identified with the control loops and sensors around the DBB cavity.

content, frequency noise and relative pointing noise measurements. Two lenses are used to match the incoming laser beam's waist size and position to that of the cavity eigenmode. This process will also be called mode matching in the following. A charge-coupled device (CCD) camera in the low-power output port of the cavity can be used for the initial alignment and mode matching as well as to determine the resonant laser mode. The DBB measurements will be briefly explained in this section, starting with the RPN. A more detailed description of the DBB can be found in [50] and Chapter 2.2 of [57].

Relative power noise measurement

The relative power noise of the laser beam injected to the DBB is measured with the relative power noise photodiode (RPD), which is located in transmission of a $50/50$ beam splitter in the beam path to the cavity [37, 50]. The power fluctuations are measured as an ASD over the Fourier frequencies and calibrated with the direct current (DC) voltage measured on the photodiode. The resulting RPN is then measured and calibrated via a software script that is started with the CDS. The measurement is displayed as ASD in units $1/\sqrt{\mathrm{Hz}}$ in a measurement range from $1\,\mathrm{Hz}$ to $10\,\mathrm{kHz}$. It is averaged over several measurements dependent on the chosen measurement time.
The RPD also provides a fast output channel, which can be used to measure the high frequency RPN with an external spectrum analyzer.

Higher order mode content measurement

The HOM content of the laser beam is measured with the transmission photodiode (TPD) of the cavity, while the length of the cavity is scanned over a full FSR via the PZT that is attached to the curved cavity mirror [37, 50]. This so called modescan measurement shows the cavities transmission relative to the total laser power, on a logarithmic scale, measured over the cavity length. A $40\,\mathrm{dB}$ and an $80\,\mathrm{dB}$ amplified channel in addition to the standard $0\,\mathrm{dB}$ channel in the TPD allow

for a full coverage of the HOM peaks. The final output is averaged over several measurements.
The triangular DBB cavity has different eigenmodes, which are resonant at different cavity length. Therefore, the peaks in the modescan measurement can be assigned to the different spatial modes. For example the HG_{01} and HG_{10} mode are resonant at individual frequencies. A increased laser power in them indicates a misalignment of the laser beam to the cavity. Other laser modes as for example the second order modes HG_{02} and HG_{20} are resonant at the same frequency. They can indicate mode mismatches. This separation allows not only to determine the content of higher order modes in the laser beam but also to distinguish between the modes or mode orders. The assignment of the modes in the measured modescan and the calculation of the HOM content is automated in a measurement script. Due to possible misalignment and mode mismatches of the laser beam to the DBB cavity, the calculated HOM content must be considered as an upper limit.

Frequency noise measurement

To measure the frequency noise of a laser beam a stable frequency reference is needed. The DBB measurement uses the cavity length as a reference [37, 50]. The cavity length is stabilized to the laser frequency with the dither locking scheme [82]. The dither locking scheme is very similar to the Pound-Drever-Hall scheme with the only difference that the phase modulation sidebands are not imprinted on the laser beam injected to the cavity but on the beam circulating in it. This is done by dithering the length of the cavity at the modulation frequency with the PZT attached to the curved cavity mirror. In the DBB setup, this PZT is also used as actuator in the frequency stabilization feedback control loop. The sum signal of the four channels of one of the quadrant photodiodes (QPDs) in reflection of the cavity is used as sensor in this loop.
The frequency noise measurement results from the error signal and control signal of the frequency control loop, calibrated with the error signal and control signal slope in $\mathrm{Hz\,V^{-1}}$, respectively. The measurement as well as the calibration is performed in a measurement script that is started over the CDS. The error signal gives the frequency noise below the feedback control loop's unity-gain frequency and the control signal above. Similar to the relative power noise the frequency noise is presented as ASD with the units $\mathrm{Hz}/\sqrt{\mathrm{Hz}}$ over the Fourier frequency.

Relative pointing noise measurement

The relative beam pointing noise of a laser beam is described relative to a reference beam. In the DBB the relative pointing noise of the injected laser beam is measured in relation to the eigenmode of the cavity [37, 50]. The laser beams position is stabilized to the reference cavity eigenmode via auto-alignment feedback control loops that use the differential wave front sensing technique [83]. The same phase modulation sidebands as for the length stabilization of the cavity are used. The two QPDs, located with $90°$ Gouy phase difference, in reflection of the cavity are used as sensor to measure the tilt and translation of the beam, each in the horizontal and vertical axis. After demodulating the QPD signals with the phase modulation sideband frequency an error signal with linear slope around the optimal beam position is gained for each of the four degrees of freedom. The error

signals are filtered and amplified and then fed back to the two two-axis PZT mirrors ahead of the cavity. The mirrors are located at the same Gouy phase positions as the QPDs two enable a pure tilt and translation correction.
The relative pointing noise for each degree of freedom can then be extracted of the feedback control loops error signal, below the unity-gain frequency, and control signal, above it. The lateral shift is normalized to the beam waist and the transversal shift to the beam divergence. The calibration of the signals as well as the data acquisition is performed with a measurement script and controlled via the CDS. It is described as ASD over the measurement frequency in the unit $1/\sqrt{\mathrm{Hz}}$ for each of the four degrees of freedom.

3. High power laser systems for gravitational wave detectors

Current ground-based interferometric gravitational wave detector (GWD) laser systems are based on stable non-planar ring oscillator (NPRO) lasers at a wavelength of $1064\,\mathrm{nm}$ [49], whose power is sequentially amplified, as described in Section 1.3.1. The systems used in the third GWD network's observing run, could deliver power levels up to $100\,\mathrm{W}$ behind the pre-mode-cleaner (PMC), which is way below the aLIGO requirement of $180\,\mathrm{W}$ at the same position. As described in Section 1.2, the next generation of gravitational wave detectors will require an even higher laser power, which currently can't be reached by a single laser amplifier chain.

This chapter is dedicated to the development of high power laser sources suitable for the usage in ground-based interferometric GWDs. Different laser systems based on laser amplification or coherent beam combination (CBC) are tested in the scope of this thesis. The first system that will be described in Section 3.1 is based on sequential solid-state laser amplifiers. The research focus for this experiment is on the effects of the second amplifier on the properties of the amplified laser beam. Based on these results, the laser system that aLIGO will use for the GWD network's fourth observing run was developed and is also presented in Section 3.1.4.

The second system is based on the coherent combination of two laser beams amplified by solid-state amplifiers in a Mach-Zehnder interferometer configuration, and will be presented in Section 3.2. The system is integrated in the reference system, as described in Chapter 2, and characterized regarding the impact of the coherent combination on the laser beam's noise properties.

As a next step towards higher laser power, a very similar CBC laser system, with fiber instead of solid-state laser amplifiers is presented. This system was installed in a cooperative work in the Laser Zentrum Hanover e.V. and the characterization of the combined laser beam is presented in Section 3.3.

Finally, a proof-of principle experiment on the coherent combination of two laser beams with different laser power that origin from different seed sources is described in Section 3.4. To compensate the expected combination losses due to the different laser power the beams are combined on a beam splitter with variable ratio of reflection and transmission. Here, the experimental layout and a conclusion on the possible combination efficiency with a variable beam splitter are presented.

3.1. Sequential solid-state laser amplifiers

An option to increase the available laser power for GWDs could be to rely on the known solid-state laser amplifier technology, but include additional amplification stages (see Section 1.3.1). Therefore, a system of three sequential solid-state laser amplifiers is presented in this section. The optical layout of the system is designed to characterize the influence of the last amplification stage on the laser beam with respect to the noise properties beam profile and power, and thereby unmask possible limitations. In this configuration the maximal reachable laser power with beam properties suitable for GWDs (see Section 1.2) is 195 W. The results of this work are published in [55] and major parts of this section will be very similar to the content of the publication. The results of this work led to the integration of the used amplifiers in the aLIGO laser system for the fourth observing run [56], which is assembled as a prototype at the aLIGO Livingston site.
This section starts with the description of the experimental layout, including a short introduction to the used amplifiers. It is followed by the characterization of each laser parameter of the system and the discussion of the results including possible limitations. The results will then be summarized and the scientific relevance will be stated. Finally the laser system for the GWD networks fourth observing run will be presented briefly.

3.1.1. Experimental layout

The experimental layout to characterize the sequential amplifier laser system is shown in Figure 3.1. The three amplifiers are placed at different positions of the

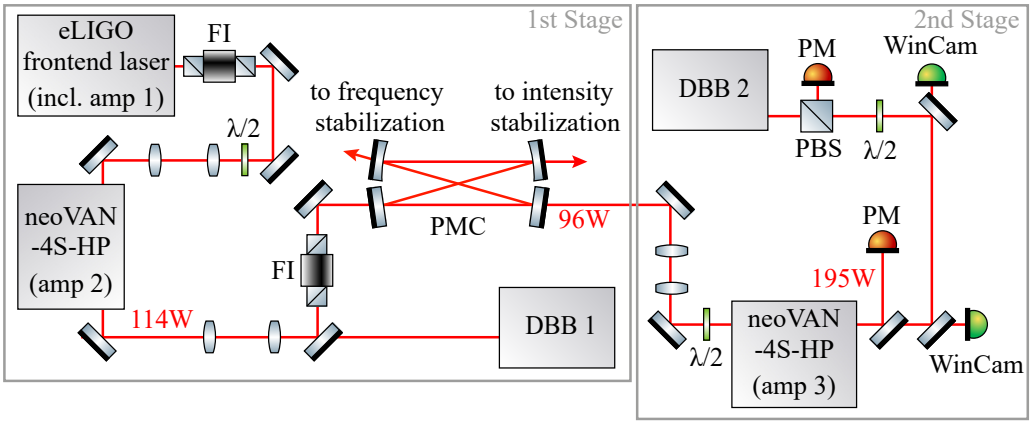

Figure 3.1.: The laser system consists of a first and a second stage. The first stage contains a diagnostic breadboard (DBB 1) to characterize the beam coming from the first neoVAN- 4S-HP laser amplifier (amp 2). The pre-mode-cleaner (PMC) performs spatial filtering to the laser beam. Its two low-power outputs are guided to the optical components needed for the frequency and power stabilization, respectively. The output beam of the second neoVAN-4S-HP laser amplifier (amp 3) in the second stage is characterized with a second diagnostic breadboard (DBB 2) and several cameras (WinCam) and power detectors (PM). Modified figure from [55].

aLIGO PSL reference system environment. The eLIGO frontend laser, as first component of the system, contains a $2\,\mathrm{W}$ NPRO laser and the first of the three Nd:YVO_4 solid-state laser amplifiers. It has a maximal output power of $35\,\mathrm{W}$ and is described in Section 2.1.1. In this experiment the output power of the frontend laser was reduced to $27\,\mathrm{W}$ to optimize the laser beams higher order mode content (HOM) to $2.7\,\%$.
The frontend laser's beam power is amplified in two sequential neoVAN-4S-HP solid-state laser amplifiers manufactured by the company neoLASE that are located at different positions in the pre-stabilized laser system (PSL) reference environment, described in Chapter 2. Each of the amplifiers consist of four Nd:YVO_4 crystals in series as shown in Figure 3.2. Each crystal is pumped by a laser diode operating at a wavelength of $878\,\mathrm{nm}$ with a maximum laser power of $65\,\mathrm{W}$ [54]. The diodes are wavelength stabilized via volumetric Bragg gratings. Hence, the diode temperature does not have to be adjusted for different pump currents to ensure the operation at the optimal pump wavelength. The light of the pump diodes is send to the amplifier module via fibers, where lenses focus the pump light, through dicroic mirrors, into the amplifier crystals. The pump diodes and their electronics, as well as the Nd:YVO_4 crystals are water cooled to avoid damage from overheating. When the seed laser passes the pumped crystal it gets amplified by stimulated emission at the seed laser wavelength as described in Section 1.3.1. For sufficiently high seed power levels the amplifier is saturated and up to $95\,\mathrm{W}$ of laser power at a wavelength of $1064\,\mathrm{nm}$ can be extracted from a single neoVAN-4S-HP laser amplifier.
The reached amplification and the spatial profile of the amplified beam depend on the size and position of the laser beam that passes the solid-state crystals. An

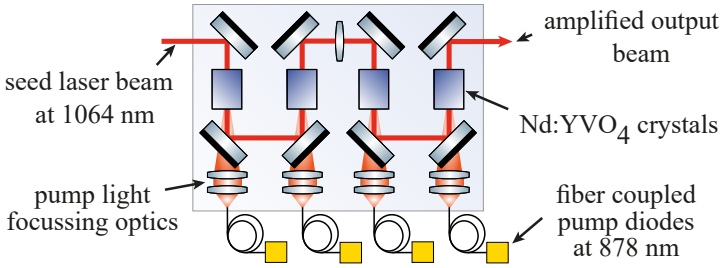

Figure 3.2.: Layout of the neoVAN-4S-HP laser amplifiers. The seed laser beam passes four Nd:YVO_4 crystals in series. Fiber coupled diodes, at a wavelength of $878\,\mathrm{nm}$ with a maximal power of $65\,\mathrm{W}$, are used to pump the crystals such that a power extraction of up to $95\,\mathrm{W}$ is achievable. Modified figure from [55].

optimal Gaussian seed beam profile at the amplifier input is defined by the crystal sizes as well as a lens that is installed insides the amplifier by the manufacturer. Therefore, mode-matching lenses ahead of each amplifier are implemented. A precise alignment with two mirrors ahead of each amplifier is necessary to guarantee that the laser beam passes the crystals centered and hence allow for an uniform amplification. The polarization of the seed beams is adjusted to the birefringent amplifier crystals via half-wave plates ($\lambda/2$).
The first neoVAN-4S-HP, labeled amp 2 in Figure 3.1, is located behind the frontend laser. A small fraction of the amplified beam is send to the first diagnostic bread board (DBB 1) for characterization. The main fraction of the beam coming

from amp 2 passes the PMC that performs filtering of the laser beam and provides two low power beam samples that can be used for the frequency- and power stabilization (see Section 2.1.2). This first stage of the presented laser system was previously characterized, as described in [54]. It generates a laser power of $114\,\mathrm{W}$ in front and more than $100\,\mathrm{W}$ in transmission of the PMC.
Up to $96\,\mathrm{W}$ from the beam filtered by the PMC serves as seed for the second neoVAN-4S-HP (amp 3) in the second stage of the setup. This high power seed laser beam with an almost perfect TEM_{00} spatial laser mode is an optimal laser source to characterize the third amplifier. In addition to the high spatial mode purity the power and frequency of this seed beam can be stabilized to analyze the noise added by a neoVAN-4S-HP to a low noise seed beam. The second diagnostic bread board (DBB 2) is used to characterize the output beam of amp 3. To avoid light from amp 3 travelling backwards into amp 2 an additional Faraday isolator (FI) is installed in front of the PMC.

3.1.2. Characterization and possible limitations

The laser system described in Section 3.1.1 is characterized with respect to its laser power, spatial mode profile and laser noise. The findings are presented in this subsection. The measurement results are discussed for each important laser parameter (see Section 1.2) and possible limitations of the laser system are uncovered. The noise behaviour and mode profile was measured regularly during the long term tests shown in Section 3.1.2 and no significant changes could be observed.
The noise performance of the laser beam that is amplified by amp 3 is characterized and compared to the beam transmitted by the PMC. All measurements were performed at the maximal power levels of $95\,\mathrm{W}$ from amp 2 behind the PMC and $195\,\mathrm{W}$ from amp 3, respectively. The higher order mode content measured behind amp 3 at this power level is $<14\,\%$.

Laser power and beam profile

The maximal output power measured behind the third amplifier is $195\,\mathrm{W}$ with a HOM content $<14\,\%$, that is measured with DBB 2. A half-wave plate and thin film polarizer behind amp 3 are used to measure the content of linear polarized light which is used to calculate a polarization extinction ratio (PER) of $>18\,\mathrm{dB}$. Output power measurements of both neoVAN-4S-HP laser amplifiers are taken by varying their seed power at a constant pump power level. The corresponding slopes for both neoVAN-4S-HP amplifiers are presented in Figure 3.3. The seed power for amp 2 and amp 3, respectively, is adjusted with half-wave plates together with a polarizing beam splitter for amp 2 and a thin film polarizer for amp 3. The polarizing beam splitter as well as the thin film polarizer transmit only light in parallel polarization. Rotating the half-wave plate is also rotating the polarization angle. Hence, the laser power transmitted by the polarizing beam splitter and thin film polarizer depends on the degree of rotation of the half-wave plates.
By subtracting the seed power from the output power the extracted power is calculated. For both amplifiers, the extracted power first increases with the seed power and then saturates to a nearly fixed value due to gain saturation. In a gain saturated amplifier the seed power reaches a value for which the transition rate from the upper to lower laser state saturates the population difference between the laser

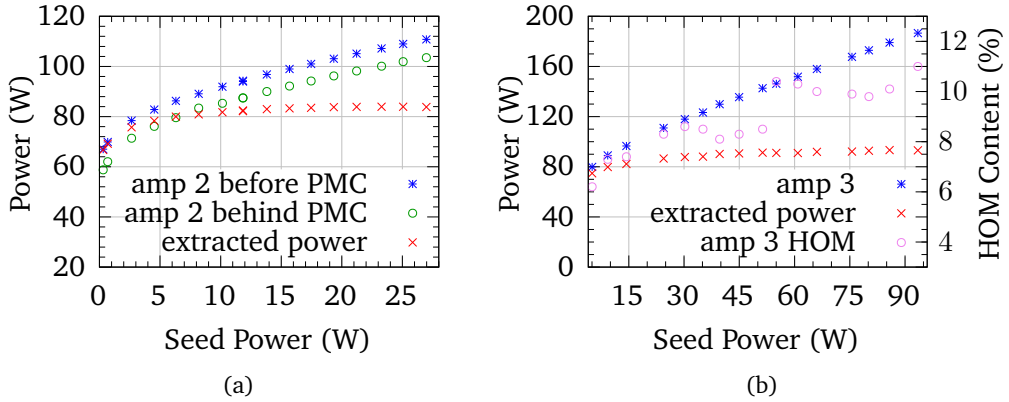

(a) (b)

Figure 3.3.: (a) Amplified power, PMC transmission and extracted power as a function of the seed power of the first neoVAN-4S-HP. The extracted power settles to about $84\,\mathrm{W}$ (data from [54]). (b) Amplified power, extracted power and higher order mode content as a function of the seed power of the second neoVAN-4S-HP. The extracted power settles to about $95\,\mathrm{W}$. Modified figure from [55].

states (see chapter 7.6 of [84]). The measurement curves for the first neoVAN-4S-HP laser amplifier (amp 2), shown in Figure 3.3a are published in [54] and shown here for completeness. The extracted power from amp 2 is $\sim 84\,\mathrm{W}$ for seed powers $\geq 5\,\mathrm{W}$. All power levels for amp 2 are measured with calibrated photodiodes. The PMC is mode selective. Thus, the almost constant difference of output power and PMC transmission shows that the mode shape doesn't change significantly. The mode matching and alignment to amp 2, that is used for all measurement steps, is optimized for a seed power of $27\,\mathrm{W}$.
The measurements of the second neoVAN-4S-HP (amp 3) are shown in Figure 3.3b. They are performed after the long term measurement shown in Figure 3.4, in which the output power decreased. Hence, a maximal output power of about $186\,\mathrm{W}$ is reached in this plot. The laser power level of the seed beam for amp 3 is the power of the beam transmitted by the PMC minus the power that is reflected at two thin film polarizers in between in PMC and the amplifier. The power in reflection of the first thin film polarizer, used for power attenuation, is measured at a water-cooled thermal power sensor. The second thin film polarizer is installed for an additional polarization clean-up of the laser beam. For seed powers $\geq 20\,\mathrm{W}$ the extracted power is $\sim 95\,\mathrm{W}$. DBB 2 measurements of the higher-order mode (HOM) content for increasing seed power show an increase from about 6% to 11% which can most probably be explained by saturation and thermal effects in the amplifier optics. It should be noted that due to possible alignment and mode matching mismatches the DBB HOM content measurements show an upper limit for the actual HOM content of the laser beam. The HOM content of the beam amplified by amp 3 depends also strongly on the alignment and mode matching to the amplifier. It can thus not be ruled out that a lower HOM content can be reached with a better alignment and especially mode matching. Here, the mode matching and alignment to amp 3 is optimized for the maximal measured seed power and not changed during the seed power variations. The orientation of the half-wave plate in front of the amplifier, however, needs to be optimized during the measurement sequence as the ampli-

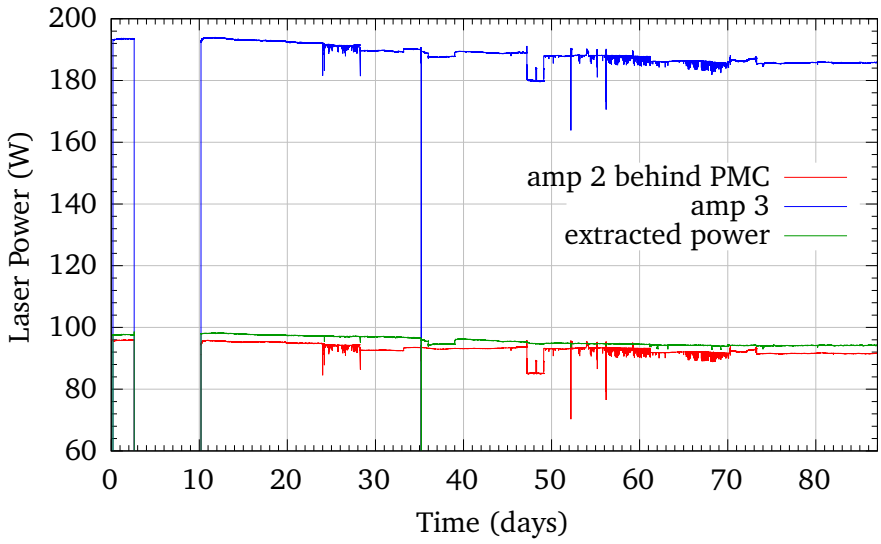

Figure 3.4.: Output and seed power of the third amplifier as well as the extracted power measured over 88 days. The systems power decreases slightly until it gets to a stable operation point at about 185 W. Modified figure from [55].

fier crystals are birefringent and thus the cross section for stimulated emission is strongly dependent on changes in the input polarization. Such changes are caused by absorption in the half-wave plate leading to a power dependent temperature and hence, a power dependent retardation.
Figure 3.4 shows an 88 day measurement of the output power of amp 3, its seed power in red and the difference of both. Both time series are measured with calibrated water cooled power meters. A slight drop in both power levels can be observed and after about 60 days both values settle. The times at which an upwards step can be seen in both curves correspond to a manual realignment of the beam coming from amp 2 and going to the PMC. Due to the constant extracted power at high seed powers, it is expected that the power of amp 3 changes by the same amount as its seed. However, the power loss of amp 3 is twice the power reduction of amp 2 over the full measurement time. This can only be explained by at least partly independent power degradation mechanisms as, for example, due to moving components in front of amp 2 and amp 3 and decreasing diode output power, respectively.

Relative power noise

Figure 3.5 shows the DBB 2 measurements of the relative power noise (RPN) of the beam coming from amp 2, that is transmitted by the PMC, and the beam coming from amp 3, plotted as ASDs over the Fourier frequency. The RPN of an amplified laser beam can be described as a combination of the RPN of the seed laser and of the pump diodes.
To estimate what fraction of the noise is associated to the power noise of the seed laser, the transfer function from seed laser modulations to output power modulations of amp 3 is measured and shown as a Bode plot in Figure 3.6 The seed laser power modulation is imprinted to the seed beam with an AOM in between

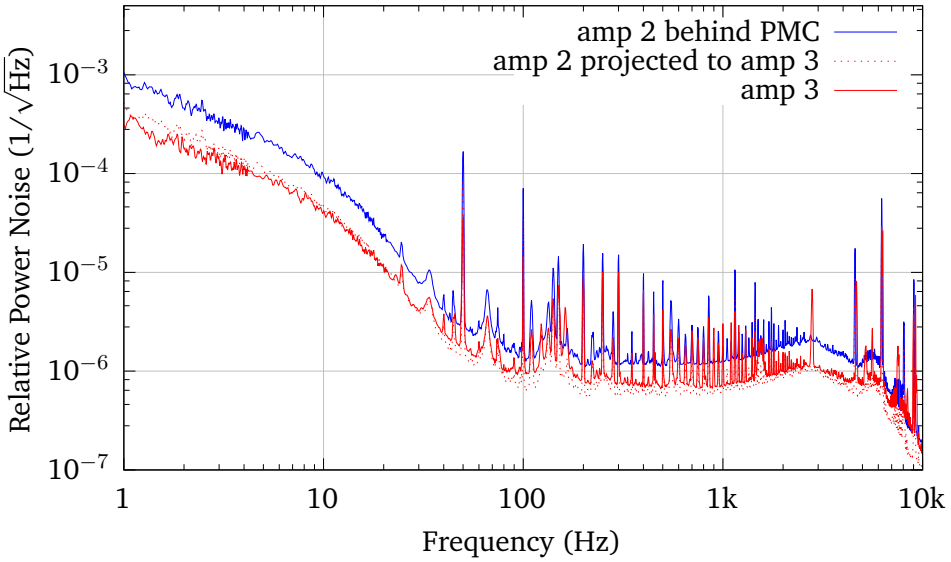

Figure 3.5.: DBB 2 measurements of the RPN from beam 2 behind the PMC and beam 3. Only small deviations between the measured relative power noise of amp 3 and the RPN of beam 2 which is projected the output of amp 3 via the amplifier transfer function can be observed. Modified figure from [55].

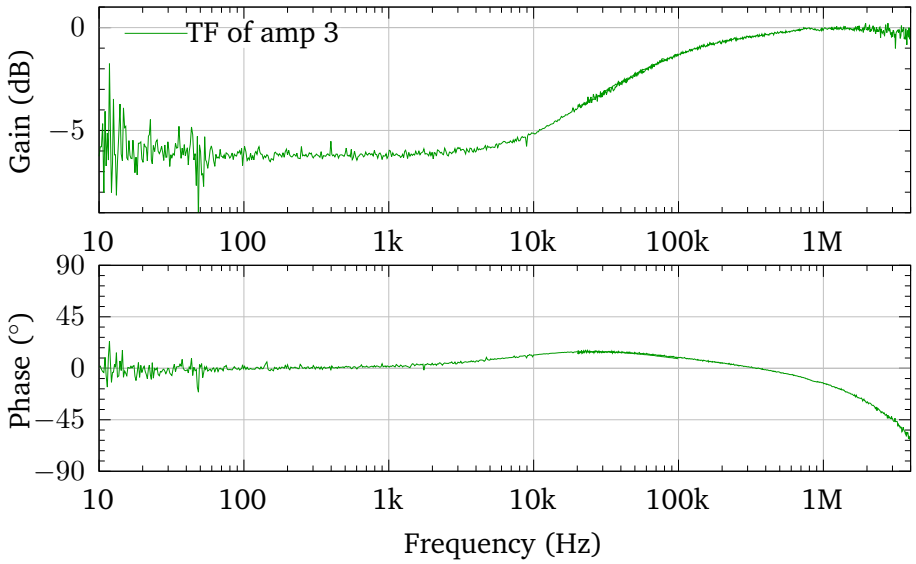

Figure 3.6.: The amplifiers transfer function displays the ratio between the RPN of the beam amplified by amp 3 to the RPN of its seed. Its value at low frequencies ($\approx -6\,\mathrm{dB}$) is equal to the power ratio between seed and amplifier output. At high frequencies the amplification follows the modulation and the gain raises up to a value of $0\,\mathrm{dB}$. Modified figure from [55].

amp 2 and the PMC and the power modulation before and behind amp 3 are measured with calibrated photodiodes. The measured amplifier transfer function shows

the expected frequency dependence for solid-state laser amplifiers: at low Fourier frequencies, up to several kHz the dynamical processes in the amplifier are fast enough to maintain a steady state situation of the gain saturated operation. Hence, the output power follows the seed power according to the blue measurement points in Figure 3.3b and the transfer function measurement gain at low frequencies of $\approx -6\,\mathrm{dB}$ is equal to the power ratio between the seed and amplifier output beam of $96\,\mathrm{W}$ to $195\,\mathrm{W}$. At higher frequencies the inversion of the laser transition is too slow to adapt to the changing seed power. Thus, a constant amplifier gain applies and the curve rises to $0\,\mathrm{dB}$. More details about the amplifier gain dynamics can be found in [85, 86].
The measured amplifier transfer function is used to project the measured RPN of the laser beam coming from amp 2 to the expected RPN of the beam coming from amp 3. The curve of the projected and measured RPN of the laser beam coming from amp 3 deviate less than a factor of ≈ 1.5 from each other over the measured frequency band. This indicates that the free running RPN of the beam coming from amp 3 is dominated by the seed laser contribution at most frequencies in the measurement band. The small offset between the curves at frequencies above $3\,\mathrm{Hz}$ could be caused by the pump diode's RPN contribution.
To verify the assumed pump noise contribution at the named measurement frequencies and to further investigate the amplifier's impact on its seed beam's relative power noise, the PSL power stabilization loop, described in Section 2.1.3, is enabled. In this experimental layout an acousto-optic modulator (AOM) located

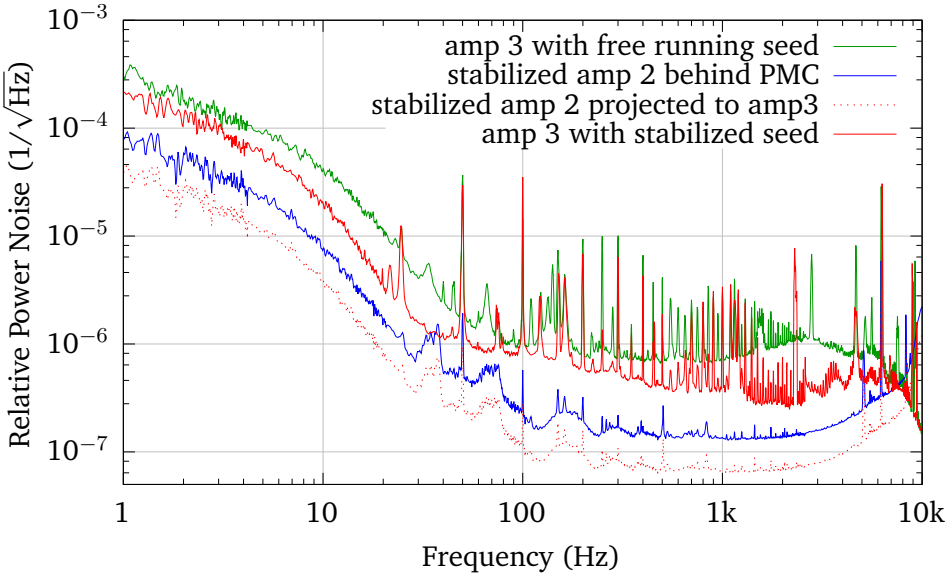

Figure 3.7.: RPN measurements of amp 3 with free running seed, the stabilized amp 2 and amp 3 with stabilized seed. A projection of the RPN of amp 2 to the RPN of amp 3 shows the expected RPN of amp 3 if the seed noise dominates. The relative power noise of the second stage is no longer seed dominated, when the seed is stabilized. Modified figure from [55].

between the first neoVAN-4S-HP and the PMC is used as an actuator for the power stabilization. In Figure 3.7 the RPN of the stabilized beam coming from amp 2 behind the PMC is shown together with the expected contribution of this noise to the

RPN of amp 3 in dotted lines determined via the described projection technique. The resulting power stabilized beam in transmission of the PMC is then used to seed amp 3. Furthermore, the measured RPN of the amplified light behind amp 3 is shown. For comparison also the RPN of amp 3 with free running seed is plotted again. All measurements are taken with DBB 2 and plotted as ASD over the Fourier frequency.
The measured RPN of amp 3 is lower than its RPN when the seed is not stabilized but clearly above the projected RPN contribution of its stabilized seed. This shows that noise is added by this amplifier, which is most likely due to the power noise of its pump diodes. At frequencies around $100-200\,\mathrm{Hz}$ and $>3\,\mathrm{kHz}$ the stabilized and free-running amp 3 beams RPN is at a very similar level. These frequency regimes fit to the regimes in which the expected and measured in RPN in Figure 3.5 differs which supports the assumption that the difference appears due to a coupling of the amplifiers pump noise.

Frequency noise

The frequency noise measurements of amp 2 behind the PMC and of amp 3 are shown in Figure 3.8. Both measurements are captured with DBB 2 and plotted as ASD over the Fourier frequency. As expected from previous measurements with a single-pass amplifier [54], the frequency noise of the beam amplified by amp 3 is not higher than that of its seed beam. Both measurement are close to the expected NPRO laser frequency noise projection, also visible in Figure 3.8. Slight

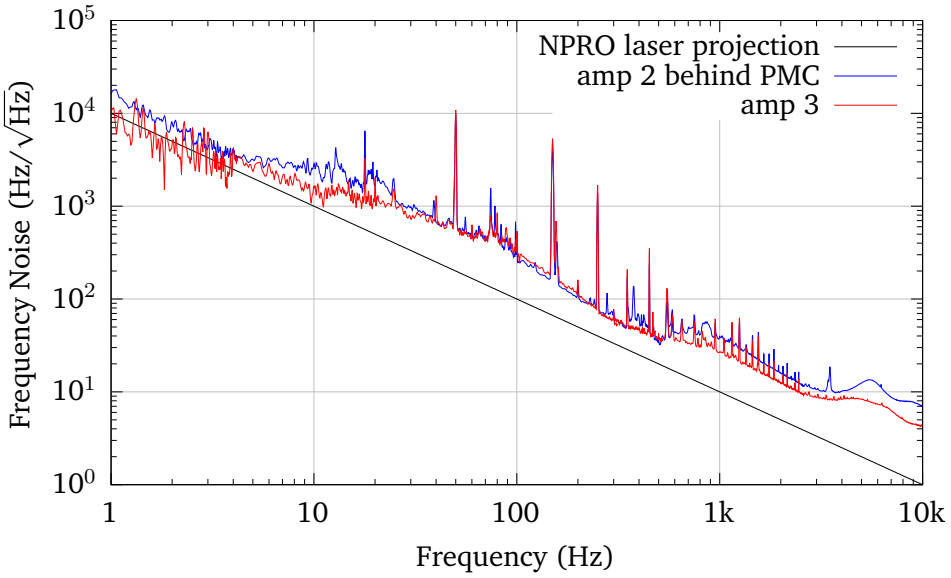

Figure 3.8.: Frequency noise measurements of amp 2 and amp 3, both measured with DBB 2 behind the PMC. The frequency noise curves of amp 3 and its seed are very similar, which leads to the conclusion, that the third amplifier doesn't add frequency noise to its seed. The small offsets below $30\,\mathrm{Hz}$ and above $600\,\mathrm{Hz}$ result most likely from environmental changes that effect the DBB measurement. Modified figure from [55].

offsets between the two curves can most probably be explained by different environmental perturbations, like for example acoustic noise that effects the DBB 2

cavity length stability. A further investigation of the possible influences from amp 3 to its seed laser beam's frequency noise is possible by enabling the PSL frequency stabilization, which is described in Figure 2.4. The corresponding frequency noise measurements are captured with DBB 2 and presented as ASD over the Fourier frequency in Figure 3.9. The figure shows the frequency noise measurement of amp 3

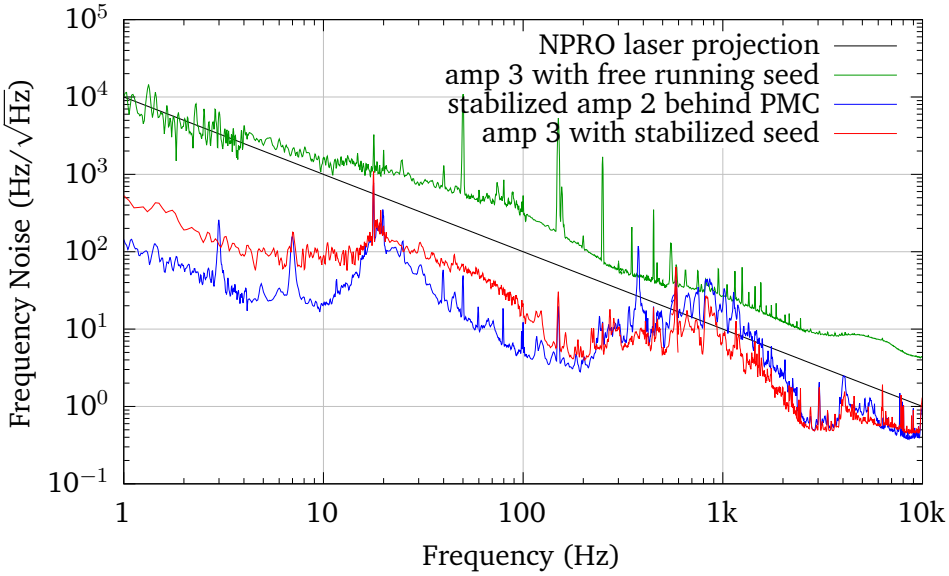

Figure 3.9.: Frequency noise of the stabilized seed, and amp 3 with free-running seed and stabilized seed. The frequency noise of the amp 3 is seed dominated at high frequencies. At low frequencies the frequency noise added by the amplifier is higher than the seeds frequency noise. Modified figure from [55].

with free running seed, of the frequency stabilized amp 2 beam after the PMC and of the amp 3 output beam, when seeded with this stabilized light from amp 2.
The frequency noise curves of the stabilized amp 2 and amp 3 with stabilized seed are lower than the noise of the third amplifier with free running seed. This shows that the limitation in earlier frequency noise measurements was given by the seed. For Fourier frequencies above $100\,\mathrm{Hz}$ the curves of the beam from amp 3 and its seed are about the same. Hence, the amplifier does not add additional frequency noise to its seed beam in this frequency range. Here, the measurement is limited either by the frequency stabilization loop or the diagnostic breadboards internal measurement noise, most likely caused by length fluctuations of its reference cavity.
Below $100\,\mathrm{Hz}$ a difference between the two frequency noise measurements is visible. This could be due to the amplifier adding noise to its seed. Another possible explanation for this difference could be that the environment and with it the DBB sensor noise is changing over time.

Relative pointing noise

DBB measurements of the relative beam pointing noise (see Section 1.2.4) are presented in Figure 3.10. The four curves per beam pointing measurement are each representing one of the four degrees of freedom, translation and tilt in horizontal

and vertical direction at the position of one of the mirrors and are presented as ASDs over the Fourier frequency.
The measurement of the relative pointing noise Figure 3.10 of the second amplifier in front of the PMC is taken with DBB 1 and the other two measurements are performed with DBB 2. The upper limits for the relative pointing noise measurements

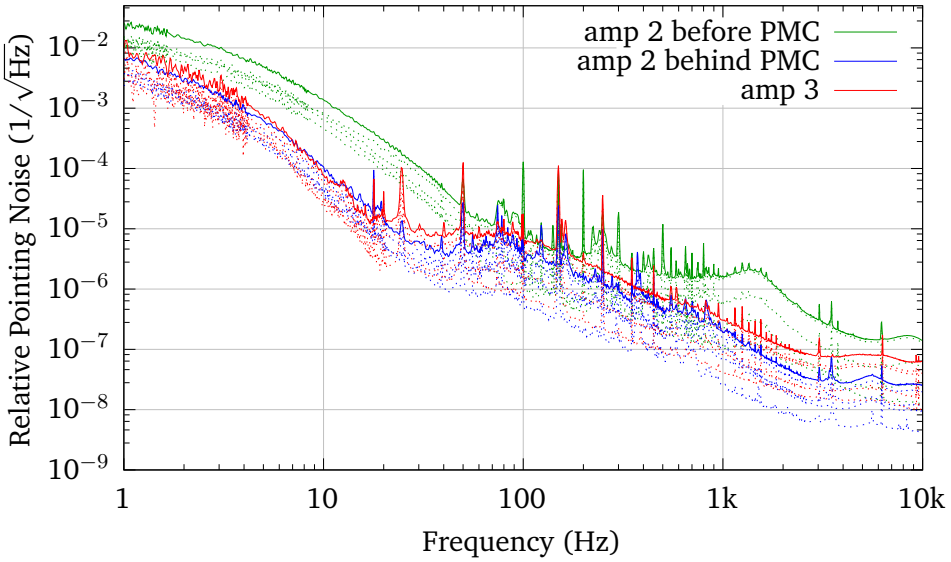

Figure 3.10.: Relative pointing noise measurements of amp 3 as well as amp 2 measured before and behind the PMC. The curves representing the four independent degrees of freedom for each measurement are plotted in the dotted version of the color used for the corresponding upper limit. The low PMC filtered beam pointing is slightly increased when measured behind amp 3. Modified figure from [55].

are derived by the uncorrelated sum of the four pointing degrees of freedom per measurement and highlighted as solid lines in the figure. The curves for the four independent degrees of freedom are plotted in a dotted version of the upper limit value's color. They deviate less than a factor five from the mean value.
When comparing the relative beam pointing noise of amp 2 before and behind the PMC a filtering effect of the PMC can be observed as described in Section 2.1.2. Thus, the beam pointing noise measurement of the second amplifier behind the PMC shows reduced noise as it is expected from the PMC's passive filtering. The relative pointing noise suppression is at most measured frequencies below the expected factor of 63. Possible reasons for this can be environmental disturbances like acoustic noise or vibrations that couple to the pointing of the beam between the PMC and DBB. Also unstable components in this beam path or sensor noise of the DBB itself can not be excludes as origin of the additional relative pointing. It should be noted that the PMC's spatial filtering is typically associated with a correlated enhanced power noise in transmission of it.
The pointing of the beam behind amp 3 is similar to the PMC filtered beam pointing of the beam coming from the amp 2. At measurement frequencies below $20\,\mathrm{Hz}$ the two measurements are on the same level. Above $20\,\mathrm{Hz}$ an increase below a factor of two of the amplified beam is visible compared to its seed beam.
The pointing noise of amp 2 before the PMC as shown here, is not increased with

respect to its seed, as it is described in [54]. In that earlier measurement, both, the seed and the amplified beam's relative pointing noise were measured before filtering due to the PMC, which results in the conclusion that the amplifier doesn't add relative pointing noise above the free-running seed beam's noise level. In the measurements for amp 3 shown in Figure 3.10, its seed beam's relative pointing noise is filtered by the PMC. The fact that the increase in the relative pointing noise of the amplified beam compared to it's seed, visible in Figure 3.10, does not exceed the free-running relative pointing noise measurement of the beam from amp 2 measured before the PMC, fits to the conclusion from the measurements in [54]. It also indicates that the increase could be explained by an addition of this small amount of pointing noise by the amplifier, which could for example origin from thermal effects on the optics in or behind the amplifier.
Another explanation for the increased noise could be environmental changes in between the measurements that affect the DBB 2 pointing noise measurements. The relative pointing noise measured behind amp 3 is below the free running relative pointing noise measured behind amp 2 before the filtering by the PMC.
An increased relative pointing noise in a laser beam can often be explained by vibrations on the laser table. As mentioned in Section 3.1.1, the pump diodes and the crystals of the amplifiers are water cooled. As water cooling can cause vibrations on the optical table, as little flow as necessary should be used. To determine the minimal required water flow to cool amp 3, DBB measurements with different flow rates are taken. Water flows from $3\,\mathrm{L/min}$ down to $0.14\,\mathrm{L/min}$ are used to cool the crystals. With decreasing flow the laser head temperature, as displayed by the control unit, increased from about $21\,^{\circ}\mathrm{C}$ to about $26\,^{\circ}\mathrm{C}$, which isn't exceeding the safe operation temperature range, given by the manufacturer. No dependence of the flow rate on the relative power noise, frequency noise and relative pointing noise in the investigated flow rate interval can be measured. Without changing the mode matching and alignment to the amplifier, fluctuations in the higher order mode content of $\pm 2.5\,\%$ and a power loss of $2\,\mathrm{W}$ of output power are observed, when decreasing the water flow. The input polarization to amp 3 needs to be slightly readjusted to keep the higher order mode content within this range.

3.1.3. Conclusion and classification

A long term stable laser system based on solid-state laser amplifiers integrated in a pre-stabilized laser environment is presented. The results of the presented laser system build the basis for the laser system that will be used in aLIGO fourth observing run (O4), which is presented briefly in Section 3.1.4.
The amplifiers are highly reliable, fault tolerant and robust against changes in their surroundings. The system delivered an output power of $195\,\mathrm{W}$ with a PER $>18\,\mathrm{dB}$ and a higher order mode content $<14\,\%$ which corresponds to $>168\,\mathrm{W}$ in the TEM_{00} laser mode. A lower HOM is expected to be possible with a better mode matching and alignment to the amplifier. Nevertheless, the generated result exceeds the laser power that was available in the last GWD networks observation run of $70\,\mathrm{W}$ for aLIGO [56] and $100\,\mathrm{W}$ for Advanced Virgo [87] and could provide the originally anticipated $165\,\mathrm{W}$ in transmission of the PMC to reach the aLIGO design sensitivity.
It is shown that the RPN and the frequency noise added by the second stage of the setup is below the free-running noise of the first stage. Especially with a power and

less significantly also with a frequency stabilized seed beam, an increased noise was measured due to the amplification with the neoVAN-4S-HP. This limitation leads to the suggestion to include all amplifiers within the stabilization feedback control loops before the corresponding sensors, to not spoil the achieved stability of the pre-stabilized laser system with the added noise of an amplifier behind the stabilization sensing points. As the free-running noise is not increased it can be expected that the power and frequency stabilization of the aLIGO PSL can suppress the noise as good as for the aLIGO laser systems used up to the third observing run [56, 57]. The relative pointing noise of the amplified beam is increased with a factor of < 2 in comparison to its seed at frequencies above $20\,\mathrm{Hz}$. The increase can origin from the amplifier or environmental perturbations. Nevertheless, the relative pointing noise of the beam coming from amp 3 is below the free running noise of its seed beam measured ahead of the PMC. For an integration of the second neoVAN-4S-HP before the PMC it is thus expected that the relative pointing noise is not increased in the amplification process, as already shown for the single neoVAN-4S-HP laser amplifier in [54] and two amplifiers in the aLIGO O4 test laser system [56].
It is also shown that a small amount of water flow is enough to cool the neoVAN-4S-HP amplifiers without any degradation of beam profile or the laser noise. This is beneficial with respect to vibrations on the laser table especially in comparison to the original aLIGO laser system with a high power oscillator configuration [34, 57].
Furthermore, the presented laser amplifiers are good candidates for sub components of laser systems for third generation gravitational wave detectors such as the Einstein Telescope (ET) [20] where laser powers exceeding $500\,\mathrm{W}$ will be required. Here they could be used as pre-amplifiers for following high power stages or in coherent beam combination topologies.

3.1.4. The O4 laser system

The aLIGO laser system that will be used for the GWD's fourth observing run (O4) was developed in a collaborative effort with the aLIGO research groups. The first test system was installed in the so called test and training facility at the aLIGO Livingston site during this thesis and the results were published in [56]. The aLIGO Livingston test and training facility is a laboratory installed at the aLIGO Livingston site, but in a separate building as the GWD. It is used to perform tests on prototypes or copies of the GWD laser systems and train people to work on them without disturbing the GWD observing run.
The O4 laser system is designed on the basis of the results on the sequential neoVAN-4S-HP amplifiers presented in the last subsections and the characterization of a single neoVAN-4S-HP laser amplifier presented in [54]. The information that are presented in this subsection are to a great extent published in [56].
The laser system consists of a $2\,\mathrm{W}$ NPRO laser as seed followed by two neoVAN-4S-HP laser amplifiers as shown in Figure 3.11. All components are integrated in the aLIGO PSL environment like it is described in Chapter 2. A prototype of this laser system, installed in the test and training facility, has an output power of $140\,\mathrm{W}$ with a HOM content of $<4.5\,\%$. For the pre-stabilization of this laser system, the PMC is be replaced by the all-bolted PMC, with mechanically fastened instead of glued mirrors. The aim of this change is to avoid potential mirror contamination from the glue, ease the fabrication process and allow an easy mirror swap if necessary

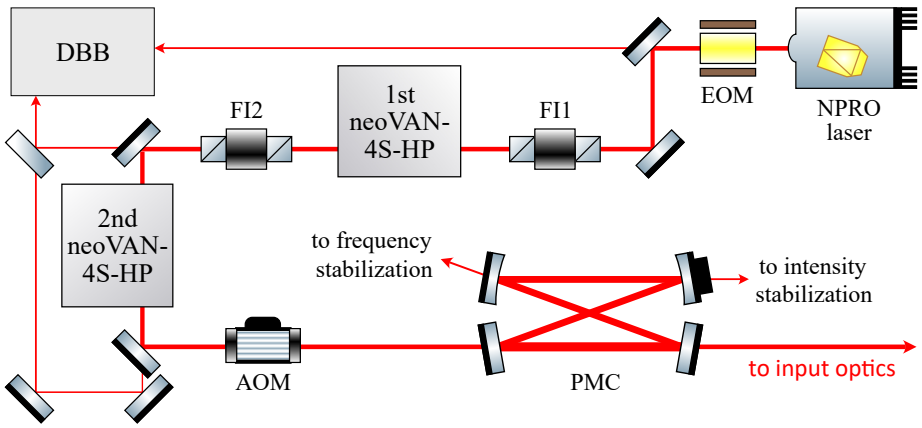

Figure 3.11.: Simplified setup of the aLIGO O4 pre-stabilized laser system. A NPRO laser seeds two sequential neoVAN-4S-HP laser amplifiers. The pre-stabilization concept is equal to the one used in O3.

[80]. At the aLIGO detector in Hanford, Washington this exchange was already performed during a the third observing run.
Apart from this change, the PSL layout is very similar as described in Chapter 2. The frequency stabilization is realized with a temperature feedback to the NPRO laser crystal, the control of the NPRO crystal length with a PZT and an EOM installed between the NPRO laser and the first amplifier as actuators.
A current shunt power actuator similar to the one demonstrated in [54] is integrated in the neoVAN-4S-HP laser amplifiers. This current shunt allows direct modulation of the pump light and thus the neoVAN-4S-HP laser amplifier's output power. Hence, the current shunt could replace the AOM as actuator for the power stabilization. This would bring the advantage of eliminating the AOM as a transmissive optical device in the high power beam path [88]. On the other hand, changes in the diode current could potentially also lead to changes in the beam parameters, especially the RPN and HOM content. The systems that are integrated in the aLIGO PSLs use the AOM as the O4 baseline actuator, as it shows a slightly better low frequency behavior compared to the current shunt in the tests performed in the test and training facility, and it has shown its reliability during prior observing runs.
The noise characterization that is performed with a DBB in the test and training facility shows over all no significant deviations from the findings that are presented in Section 3.1.2 as well as [54] and [55]. Some additional noise compared to the O3 laser system can be explained by environmental distractions due to for example acoustic noise or air fluctuations in the test and training facility which is much more noisy than the laser rooms for the actual detectors. Hence, it is not expected that this environmental noise is seen in the O4 laser systems. The relative pointing noise measurements before and behind the second neoVAN-4S-HP amplifier confirm the statement made in Section 3.1.3 that no additional pointing due to the second amplifier is expected in a configuration with all amplifiers ahead of the PMC. A detailed description of the system and evaluation of its noise behaviour can be found in [56].

3.2. Coherent combination of two beams amplified by solid-state laser amplifiers

The coherent combination of several laser beams is a promising method to provide a high power laser beam with a noise characteristic and beam profile sufficient for the needs of ground-based GWDs (see Section 1.2). The basic CBC concept can be found in Section 1.3.2. A laser system at a wavelength of $1064\,\mathrm{nm}$ based on the coherent combination of two laser beams amplified by solid-state laser amplifiers in a Mach-Zehnder interferometer configuration is presented in this section. Some preliminary results on the first stages of the work presented here were presented in the Master thesis of Christoph Gentemann [89].
The system is integrated in the aLIGO pre-stabilized laser system (PSL) reference system environment described in Chapter 2 and examined with regard to its noise performance and mode quality, as well as possible couplings from the coherent combination to the noise properties.
First, the experimental layout and the phase lock control loop of the system will be described in Section 3.2.2 and afterward the systems will be characterized in Section 3.2.3. This part finishes with a conclusion and classification of the results in Section 3.2.4.

3.2.1. Experimental layout

A simplified schematic of the described laser system is depicted in Figure 3.12. Most of the beam steering mirrors for the beam alignment, as well as lenses for the mode matching, are left out in this picture for simplicity. In this configuration, a single seed laser is used. The laser source is the reference system's eLIGO frontend laser which consists of an NPRO laser and a solid-state laser amplifier, as further described in Section 2.1.1. As it is advantageous for the beam profile to pump the frontend laser amplifier below the maximal output power, it operates only with $28\,\mathrm{W}$ output power. The frontend laser's output beam is split by a $50/50$ beam

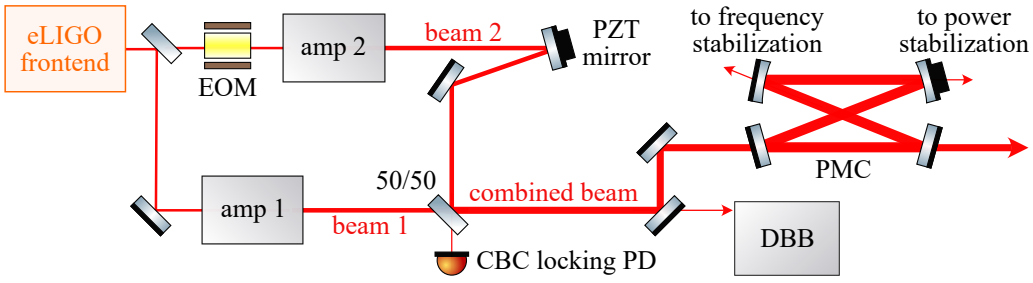

Figure 3.12.: Simplified layout of the CBC experiment. The eLIGO frontend is used as seed source for two neoVAN-4S-HP laser amplifiers, one in each arm of a Mach-Zehnder interferometer. The system is integrated in the reference system environment. The reference systems PMC and the DBB cavity are used as spatial mode reference.

splitter and each output builds one arm of a Mach-Zehnder interferometer.
One neoVAN-4S-HP laser amplifier is installed in each arm of the Mach-Zehnder interferometer. The amplifiers are described in more detail in Section 3.1.1 as well as in [54, 76]. In the first Mach-Zehnder arm, the seed beam is guided directly

through a neoVAN-4S-HP laser amplifier, which is called amp 1 in the following. The amplifier has a maximal output power of about $80\,\mathrm{W}$ in this configuration. The laser power of the beam from amp 1 can be attenuated with a half-wave plate followed by a thin film polarizer. The thin film polarizer only transmits p-polarized light. By rotating the polarization angle with the half-wave plate, it can thus be adjusted how much power the thin film polarizer transmits. A second thin film polarizer filters out any residual light in the unwanted polarization, and thereby guarantees a clean polarization of the laser beam. The power of the beam from amp 1 is attenuated to be at the same power level as the the beam coming from the second amplifier. This attenuated beam is called beam 1 in the following and is guided to the second $50/50$ beam splitter of the interferometer, which is called combination beam splitter here.
The second beam path includes an electro-optical modulator (EOM). The modulator consists of two $8\,\mathrm{mm} \times 8\,\mathrm{mm} \times 35\,\mathrm{mm}$ lithium niobate crystals. When it is operated with a laser beam above a certain intensity, thermal lenses and a photorefractive effect [90] in the crystals induce a deformation of the laser beam profile (see [91]). Thus, the laser beam sent to the EOM is attenuated to about $2\,\mathrm{W}$. The beam from the EOM is then send to a second neoVAN-4S-HP laser amplifier, which is called amp 2 in the following. The output beam of amp 2 is also guided through a half-wave plate and two thin film polarizers. The half-wave plate is adjusted in order to transmit as much light as possible. The resulting beam 2 is p-polarized and has an output power of $52.6\,\mathrm{W}$. Beam 2 is guided to the second input port of the combination beam splitter via a piezo-electric element (PZT) driven mirror, which is used as phase actuator.
The first requirement for a successful filled aperture combination is a spatial overlap of the two laser beams at all positions along the propagation axis, as described in Section 1.3.2. In this experimental layout, the PSL pre-mode-cleaner (PMC) (see Section 4.1), as well as the DBB's resonator (see Section 2.2), serve as mode-matching and alignment reference to define a common propagation axis as well as a similar waist position and size for beam 1 and beam 2. The tilt, translation, as well as waist size and position of the two beams are separately matched to the eigenmode of the PMC. With this procedure, only a small readjustment to equalize thermal effects due to the higher laser power is necessary when both beams are send to the combination beam splitter at the same time.
The coherently combined laser system is integrated in the PSL reference system environment described in Chapter 2. The combined beam is send to the aLIGO PMC, and the PMC's low power output beams are send to the frequency and power stabilization sensors. The DBB ahead of the PMC is used to characterize both input beams separately, as well as the coherently combined output beam.

3.2.2. The CBC phase lock loop

The second step to obtain a coherent combined laser beam, is the spectral overlap of the two laser beams. As the two laser beams in this setup origin from the same seed laser, they operate at the same laser frequency. Hence, only the phases of the two beams have to be matched to each other. The Mach-Zehnder interferometer is stabilized to the dark fringe with a phase lock feedback control loop. Thereby, a bright port with the summed laser power is generated at the second combining beam splitter output.

The feedback control loop design used in the presented work, is shown in Figure 3.13. Here the phase of beam 2 is stabilized to the phase of beam 1. The first

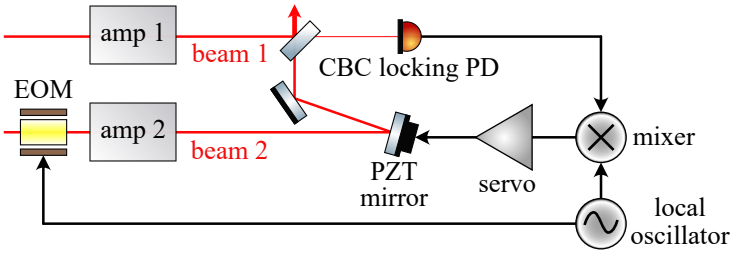

Figure 3.13.: Schematic overview of the main components used for the CBC phase lock feedback control loop. Phase differences are sensed as amplitude modulation on the CBC locking photodiode (PD) in a Pound-Drever-Hall like locking scheme. After demodulation of the PD signal, the error signal is amplified and filtered by the servo electronics. The resulting control signal is send to the PZT driven mirror, which is used as phase actuator.

component of the feedback-control loop is a phase sensor. A $1\,\mathrm{mm}$ InGaAs photodiode with transimpedance amplifier is placed at the dark port of the interferometer. This photodiode is called CBC locking PD in the following. The photodiode can only detect the power of the light at the dark port, but is insensitive to the phase of the laser field. Phase changes around the dark fringe lead to a rising power independent on the sign of the phase change. Therefore, the power measurement at the dark port can not be directly used as an error signal for the phase stabilization. To overcome this problem, a locking scheme similar to the Pound-Drever-Hall method [44] is used. Phase modulation sidebands at a frequency of $25\,\mathrm{MHz}$ are imprinted on beam 2 with the EOM located before amp 2. Those phase sidebands produce an amplitude modulation at the phase modulation frequency in the two output fields of the $50/50$ beam splitter, whenever the differential phase between the two beams is no integer of π. The CBC locking PD senses the dark port laser beam and therewith the amplitude modulations. The signal measured with the locking photo diode is then demodulated with a LO at the phase modulation frequency at the analog mixer. The mixer is followed by a low-pass filter to suppress residual signals at the modulation frequency, which is not shown in Figure 3.13 for simplicity. The demodulated signal has a linear slope over the phase difference between the two beams with zero crossing at the dark and the bright fringe phase position of the interferometer. Therefore, it is used as error signal in the phase lock feedback control loop. This error signal, is also used for the calibration of the differential phase noise and therefore shown in Figure 3.26.
The error signal is filtered and amplified with analog operational amplifiers and a high voltage amplifier with $375\,\mathrm{V}$ output range to drive the PZT. Some parts of the analog electronics, like gains and offsets, can be controlled and monitored with the CDS system. All the filtering and amplifying control units are summarized as servo in the schematic. The amplified output is the control signal.
A PZT driven high reflective mirror is inserted in the path of beam 2. If a voltage is applied to the PZT, its length and hence the optical path length of beam 2 changes. To enable phase changes in both directions, the PZT is operated at a control signal offset of $200\,\mathrm{V}$. This PZT driven mirror, is installed in the long range actuator

mounting that was used in the original aLIGO high power oscillator [92]. The mounting also contains a stepper motor which could enhance the actuation range, when needed. The mirror is installed under a very small angle of incidence to avoid

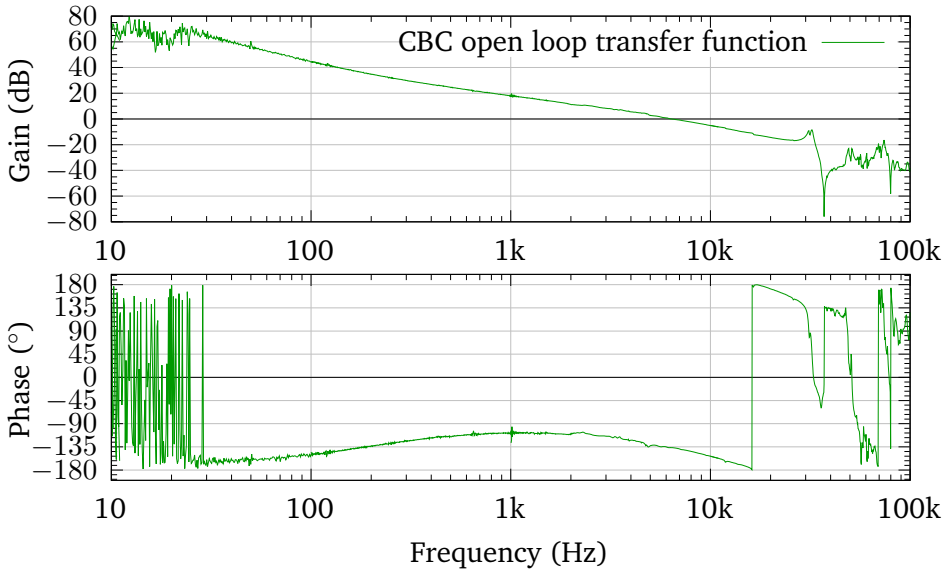

Figure 3.14.: Bode plot of the CBC phase lock loop's open-loop transfer function. The control loop's bandwidth is limited by the actuator resonance at $\sim 35.5\,\mathrm{kHz}$. The unity-gain frequency is $5\,\mathrm{kHz}$.

beam displacement due to the longitudinal actuation of the mirror position. The phase lock control signal is sent to the PZT.
The bandwidth of the phase look loop is determined by the unity-gain frequency of the open-loop transfer function. Figure 3.14 shows the Bode plot of this open-loop transfer function. The unity-gain frequency is $5\,\mathrm{kHz}$. The gain margin is $14.3\,\mathrm{dB}$ and the phase margin $46°$. The peak at around $30\,\mathrm{kHz}$ appears due to the partly filtered resonance of the PZT driven mirror. This resonance is also the unity-gain frequency limitation in the used configuration. With this control loop, a long-time stable phase lock cold be provided.
The combined beam reaches a laser power of about $100\,\mathrm{W}$ from the two $52.6\,\mathrm{W}$ single beams. This corresponds to a combination efficiency of about $95\,\%$. The efficiency is limited by a mismatch of the waist size and position of the two laser beams, as well as mode imperfections, as it will be described in 3.2.3.

3.2.3. Characterization and stabilization

The characterization aims to highlight influences of the coherent combination on the beam quality of the combined beam in comparison to the two single laser beams. The combined beam's HOM content, relative power noise (RPN), frequency noise and relative pointing noise is discussed in comparison to the two single beams' performances in this subsection. Furthermore, the differential phase noise is measured, and projections from it to the power and frequency noise will uncover possible limitations.
A power and frequency stabilization of the combined laser beam is performed to investigate the presented system's suitability as a laser source for GWDs.

Spatial beam quality

The spatial beam quality of the two single laser beams, as well as the combined beam, are determined with a modescan measurement taken by the DBB, as it is described in Section 2.2. The measurement gives an upper limit on the higher-

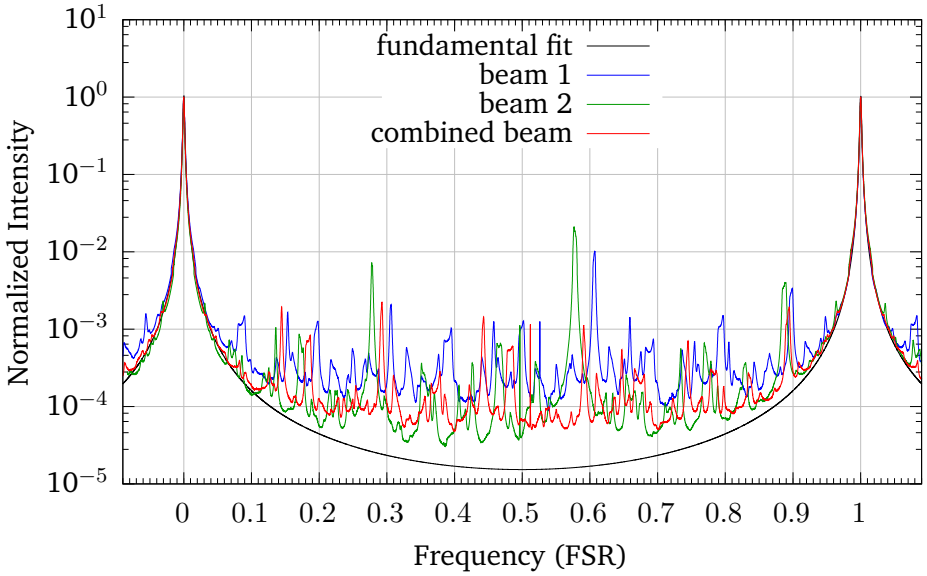

Figure 3.15.: Modescan measurements of the single beams and the combined beam. A fundamental fit indicates a beam in the pure TEM_{00} mode for comparison. Beam 1 has a HOM content of $<4.0\,\%$ and beam 2 of $<4.2\,\%$. The combined beam's HOM content is reduced to $<1.8\,\%$.

order mode (HOM) content of a laser beam as the mode matching and alignment to the DBB resonator also could result in HOMs. Figure 3.15 shows the DBB modescan measurements of beam 1, beam 2 and the combined beam as well as a fit for the fundamental mode in one FSR of the DBB resonator. The two big peaks at 0 and 1 FSR represent the TEM_{00} mode. All small peaks in between are representing higher order modes.
The higher order mode content is $<4.0\,\%$ for beam 1 and $<4.2\,\%$ for beam 2. The main prominent higher order mode peak at 0.3 FSR represents the two second order Hermite Gauss modes and the peak at 0.6 FSR the HG_{40} and HG_{40} modes. Their powers are minimized if the beam waist is at the same position and has the same diameter as the DBB resonators eigenmode. The residual power in these two modes is possibly to a small extent due to a non perfect mode matching. Most of the residual power in the higher order modes indicates a slightly disturbed beam profile due to for example astigmatism. The slight mismatch between the HOM positions for the three beams, especially visible at around 0.3 FSR and 0.6 FSR, could be due to a non-linearity of the DBB PZT.
The combined beam's measured HOM content of $<1.8\,\%$ is decreased in comparison to the single beams. In Figure 3.15 it is visible that some of the HOM peaks of the combined beam and the single beams differ significantly. Especially notable is the peak at 0.6 FSR, which is decreased for the combined beam by about one order of magnitude in comparison to the single beams. This decrease can be explained by a destructive interference between the corresponding HOMs of the two single

beams. As a $50/50$ beam splitter is used as combining element in this layout, even constructive interference can lead to a reduced power in a HOM in the combined beam if the HOM power in the two single beams is different (see Section 3.4). Both effects can lead to a decrease in the combined beam's HOM in comparison to the HOM contents of the two single beams.
The difference of $2.16\,\mathrm{W}$ in the combined beam's power compared to the total seed power can be partly traced back to the decreased HOM content of the combined beam. A slightly imperfect alignment and size of the beam waists of the two single beams relative to each other would increase the combination losses further and are the most probable origin of the residual $3.04\,\mathrm{W}$ at the combining beam splitter's dark port.

Relative power noise

The relative power noise of the combined laser beam, as well the single beams is measured with a photodiode in the DBB, as described in Section 2.2. Figure 3.16 shows the RPN as an ASD dependent on the Fourier frequency. The noise curves of beam 1 and beam 2 are each measured while the other single beam is blocked. From Section 3.1.2 and [54], it is expected that the RPN of the two single beams is mainly dominated by their seed laser's noise, with a small contribution of the laser amplifier pump diode noise above $3\,\mathrm{Hz}$. The RPN of beam 1 and beam 2 are in general at a similar noise level. The small deviations between the curves indicate

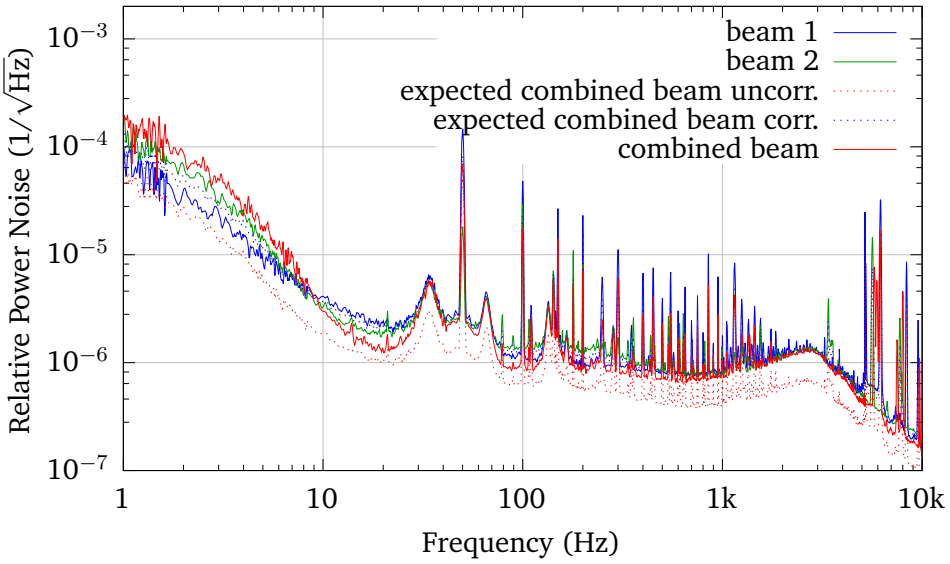

Figure 3.16.: RPN measurements of the combined beam and the two single beams. The combined beam's RPN can be assumed as a mixture of the correlated and uncorrelated sum of the single beam noises. Both sums are depicted in dotted lines.

that the noise, which is added by the amplifiers, is not just uncorrelated but also different. The noise peaks in both curves around $30-70\,\mathrm{Hz}$ and $3\,\mathrm{kHz}$, could be due to environmental noise that couples equally in the two single beams either before or behind the combining element. Therefore, the relative power noise of the two single beams can be assumed as a mixture of the correlated and uncorrelated sum

of the single beam noises.
The expected RPN of a combined beam with uncorrelated and correlated RPN of the single beams is derived in Appendix A.2. In first order, the RPNs of beam 1 RPN_1 and beam 2 RPN_2 are expected to be correlated as they origin from the same laser source. Assuming the same laser power for beam 1 and beam 2 ($P_{\text{in}} = P_1 = P_2$) the corresponding RPN of the combined beam RPN_{CBC} is calculated with:

$$RPN_{\text{CBC}} = \frac{1}{2}(RPN_1 + RPN_2). \tag{3.1}$$

The RPN contribution in the single beams, which origins from the amplifier pump diodes, is not correlated. Also environmental perturbations could couple independently in the two arms and thereby add uncorrelated noise. Therefore, a partly uncorrelated coupling of the RPN of beam 1 and beam 2 can be expected. For uncorrelated RPN of beam 1 and beam 2 and the same laser power for the two beams $P_{\text{in}} = P_1 = P_2$, the expected RPN of the combined laser beam is calculated with:

$$RPN_{\text{CBC}} = \frac{1}{2}\sqrt{1 - 2\frac{P_{\text{in}}}{P_{\text{CBC}}} + 2\frac{P_{\text{in}}^2}{P_{\text{CBC}}^2}}\sqrt{RPN_1^2 + RPN_2^2}. \tag{3.2}$$

The simulated RPN of the coherently combined laser beam, in cases of correlated and uncorrelated couplings of the single beam RPNs, are shown in addition to the measurements in Figure 3.16. It is visible that the combined beam's RPN fits to the expected noise with correlated single beam RPNs when the single beam curves match to each other. At the measurement frequencies in which the RPN of beam 1 and beam 2 are not at the same level, a partly uncorrelated noise coupling can be expected. In this frequency regimes, it is visible that the combined beam's RPN is shifted towards its expected curve for the uncorrelated RPN coupling between beam 1 and beam 2 as expected.
At frequencies below $10\,\text{Hz}$ the RPN of the combined beam is increased in comparison to the expectations and also in comparison to the single beams. One reason for this disagreement could be increased stray light for the combined beam's measurement in comparison to the single beams' measurements. This could be due to different attenuation levels required for the combined beam's and single beams' measurements. Another reason could be differential pointing between the two laser beams, which couples to the RPN dependent on the spatial alignment between the two single beams.
The possible pointing coupling will be further investigated in the following. According to the spatial geometry of a Gaussian laser beam, the differential pointing to power noise coupling increases when the alignment between the beams is not optimal. Measurements that depicts the influence of the alignment between the two beams on the combined beam's RPN are shown in Figure 3.17. The orange curve shows the combined beam's relative power noise for an intentional misalignment between beam 1 and beam 2, which is visible due to the increased dark port power of $5.8\,\text{W}$ in comparison to $5\,\text{W}$ for good alignment. An increased RPN at low frequencies due to the misalignment is visible.
An automatic alignment between the two single laser beams, based on differential wavefront sensing [83], is installed to reduce the influence of differential pointing noise on the combined beam's RPN. The important optical and electronic components that are used for this auto-alignment are depicted in Figure 3.18.

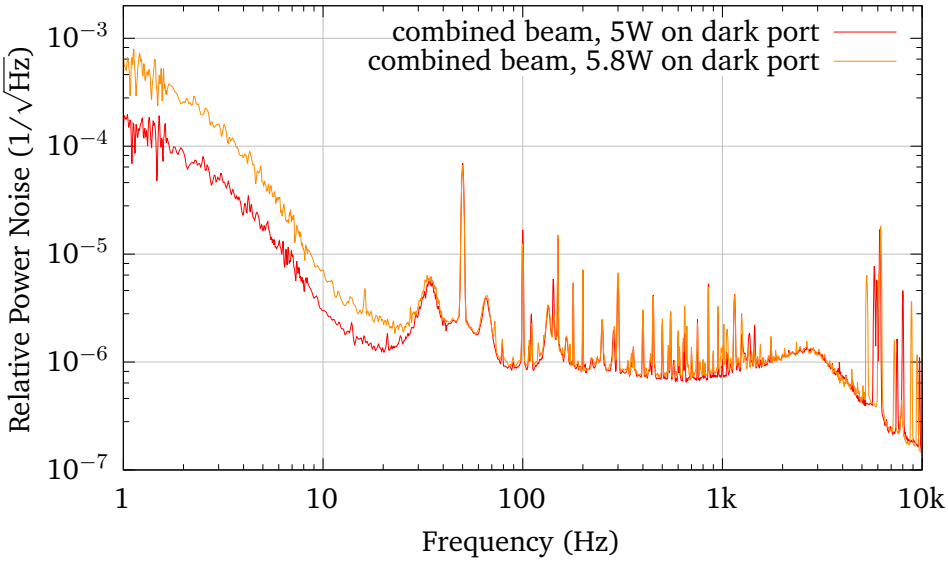

Figure 3.17.: RPN measurements of the combined beam with different alignments between beam 1 and beam 2, indicated by the dark port power. An increase of the RPN of the combined beam with intentional misalignment at frequencies below 30 Hz shows the influence of misalignment between the single beams.

The 25 MHz phase sidebands that are used for the CBC phase lock, are also used in the auto-alignment scheme. The phase sidebands in one arm cause an amplitude modulation on the two depicted quadrant photodiodes (QPDs) whenever the phasefronts of the two beams are tilted relative to each other. To resolve in which direction the beam is tilted or translated, the difference between the amplitude modulation signals on the quadrants of each QPDs are calculated. The difference between the two upper and lower quadrants gives the vertical (y), and the difference between the two left and right quadrants the horizontal (x) direction. The

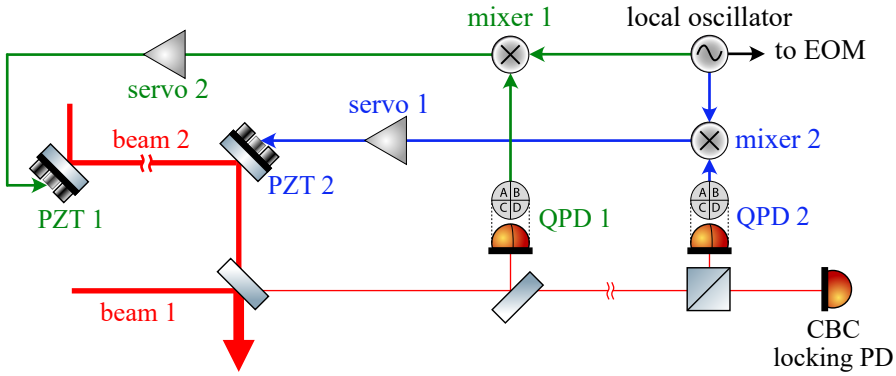

Figure 3.18.: Optical and electronic components for an auto-alignment between the two single beams. Two QPDs are used as sensors, and two two-axis PZTs driven steering mirrors as actuators.

four resulting QPD signals, one for the x and y direction, each, are demodulated with the 25 MHz LO signal via mixers to produce the four corresponding error sig-

nals, which are amplified and filtered in the servo. Low-pass filters directly behind the mixers suppress residual signals at the modulation frequency and are not depicted in Figure 3.18, for simplicity.
The resulting control signals are then fed back to the two PZT driven steering mirrors, which actuate on the propagation direction of beam 2. The positions of the

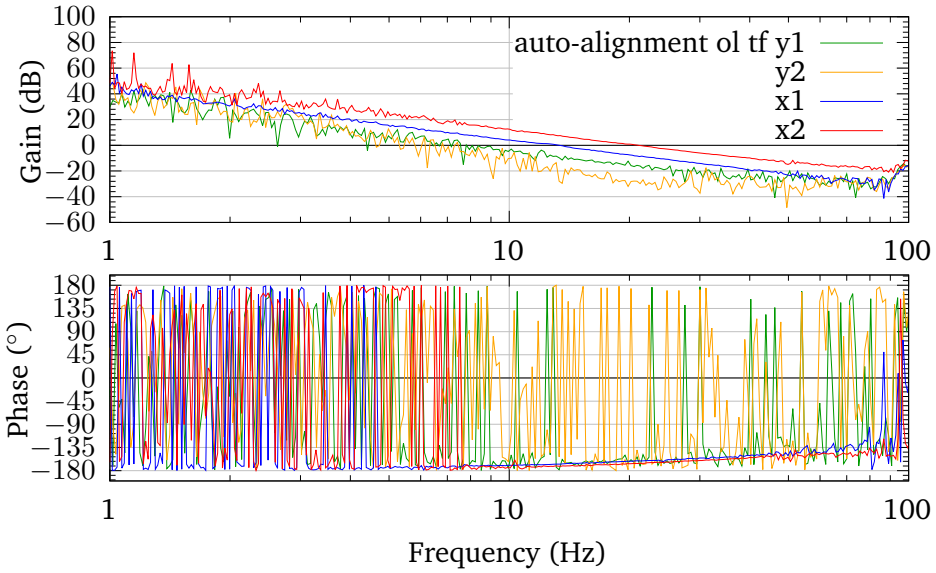

Figure 3.19.: Auto-alignment open-loop transfer functions of all four control loops, displayed in a Bode plot. The unity-gain frequencies are in the range of $7-12\,\mathrm{Hz}$. The small injected signals did not allow for a high resolution which results in the noisy phase signals.

PZT driven mirrors and QPDs are chosen such that the x and y control signals produced via QPD1 can be fed back to the x and y direction of PZT1 and the signals produced via QPD2 to PZT2, respectively. In this layout, QPD1 and PZT1, as well as QPD2 and PZT2, are located at roughly the same Gouy phase position in order to decouple the four control loops.
The open-loop transfer functions of the four auto-alignment feedback control loops are shown in Figure 3.19. The unity-gain crossings of the loops are in the range of $7-12\,\mathrm{Hz}$. The two y loops are very sensitive to disturbances. Because of that, the injected sweep signal is very small, and thus, especially the phase measurements of the y-signals are very noisy. Below $10\,\mathrm{Hz}$, the phase of all four loops is very close to $-180°$. The apparent noise at those frequencies appears due to phase jumps between $180°$ and $-180°$, which could not be compensated for in the plot script, as the resolution of the peaks is probably too small. All four curves are measured separately, with just the specific control loop engaged.
Figure 3.20 shows the RPN measurement of the combined beam with intentional alignment offset, as already used in Figure 3.17, as well as the combined beam's RPN with the same initial alignment offset, but all four auto-alignment feedback control loops engaged. For comparison, also the combined beam's RPN with optimal alignment and a dark port power of $5\,\mathrm{W}$, as already presented in Figure 3.16, is shown.
It is visible that the auto-alignment reduces the misaligned combined beam's RPN to the level of the optimal aligned combined beam in the bandwidth of the auto-

alignment control loops. The additional noise at frequencies slightly above 10 Hz is due to servo bumps in the auto-alignment control loops. The offset between the optimally aligned curve and the auto-aligned curve at measurement frequencies from 8−13 Hz indicates that the alignment between the two single beams performed with the auto-alignment is not as good as the optimal manual alignment. Nevertheless, in the control loop bandwidths, the combined beam's RPN with en-

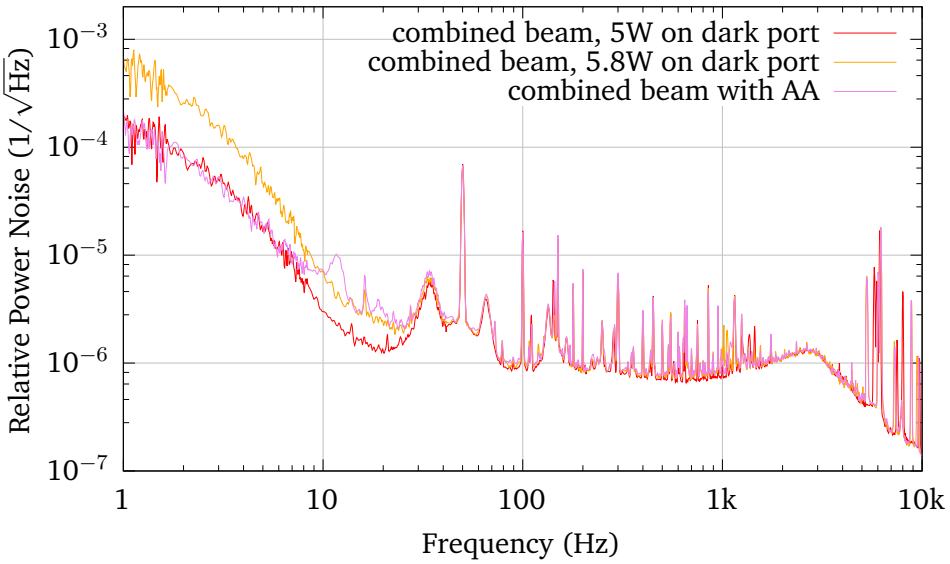

Figure 3.20.: RPN measurements of the combined beam with and without an intentional misalignment and an engaged auto-alignment. A decrease of the combined beam's RPN below 10 Hz is visible if the auto-alignment loops are engaged.

gaged auto-alignment is on the same level as the combined beam's RPN for optimal aligned single beams. As the auto-alignment loops compensate for the differential pointing between the single beams, this result confirms that the increased combined beam's RPN for misaligned single beams is due to a coupling from differential pointing noise between the single beams.
In addition to this confirmation, the measurement also shows that the combined beam's RPN does not decrease below the measurement for optimal alignment, even if the differential pointing noise is suppressed. Therefore, it can be concluded that the increased low frequency RPN of the combined beam compared to the single beams' RPNs is most probably due to stray light on the sensors.

Power stabilization

The PSL power stabilization loop is described in Chapter 2. Its in-loop photodiode is used to measure power fluctuations in the combined beam behind the PMC. The combined laser beam's power is then stabilized by controlling the power level with two current shunts in the diode power supply of the neoVAN-4S-HP laser amplifier that amplifies beam 1. The current shunts actuate on the diode current and therewith also on the output power of the amplifier.
A power stabilization with one of this current shunts as actuator is presented in [54]. The addition of a second current shunt allows for a higher actuation range,

helps to provide a long-term stable power stabilization. The power stabilization electronics are optimized for the specific needs of the presented system.
The in-loop (il) and out-of-loop (ool) RPN measurements of the power stabilized combined beam, are depicted as ASD over the Fourier frequencies in Figure 3.21. Also the RPN of the combined beam without engaged power stabilization, mea-

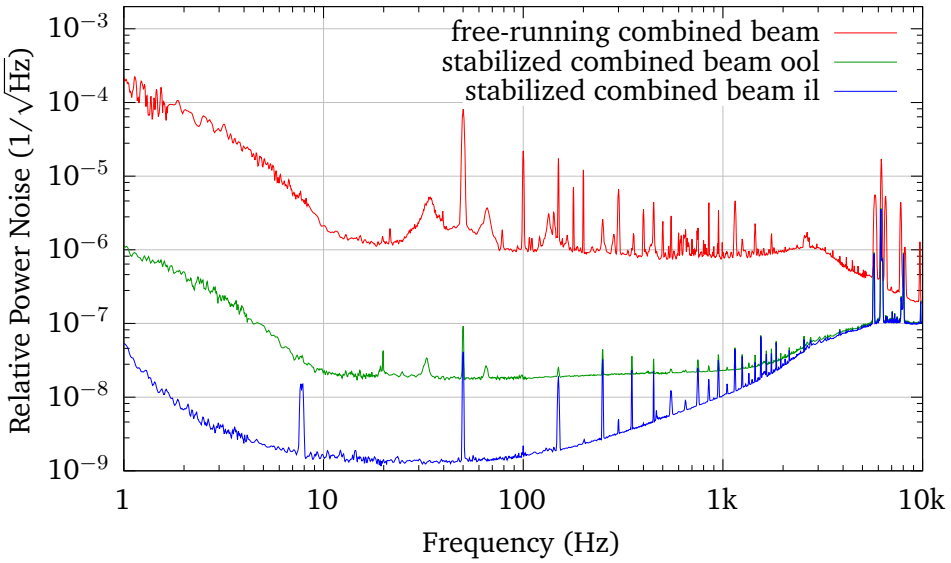

Figure 3.21.: RPN measurements of the free-running and stabilized combined laser beam. The stabilized beam's curves are measured with the reference system's in-loop and out-of-loop photodiode. The free-running RPN is measured with the DBB.

sured with the DBB, is shown for comparison. The stabilized RPN is shot noise limited between about $10\,\mathrm{Hz}$ and $1\,\mathrm{kHz}$. The out-of-loop photodiode detects a photocurrent of $2.8\,\mathrm{mA}$ and the in-loop detector a photocurrent of $2.8\,\mathrm{mHz}$. This corresponds to a combined shot noise level of $1.6 \cdot 10^{-8} 1/\sqrt{\mathrm{Hz}}$. The increase of the RPN from the shot noise below $10\,\mathrm{Hz}$ is due to the sensor noise of the two sensors in the feedback control loop.
The power stabilization control loop's unity-gain frequency is at around $50\,\mathrm{kHz}$ and the control loop's gain decreases below $40\,\mathrm{dB}$ above $1\,\mathrm{kHz}$. Therefore, the control loop gain limits the stabilization at high frequencies. The overall out-of-loop RPN curve is very close to the measurements that were performed with an AOM the aLIGO O3 prototype presented in [54] and at high frequencies even lower than the measurements with one current shunt in the same publication.

Frequency noise

Within the CBC phase lock loop, it is expected that beam 2 follows the instantaneous frequency of beam 1 and thus compensates for differential noise behavior. As shown in Figure 3.8 and [54], no significant frequency noise is added by the used solid-state laser amplifiers. As here a single seed laser beam is used for both amplifiers, it is expected that the frequency noise curves for beam 1 and beam 2, as well as the combined beam, are on a similar level.
The frequency noise of all three beams is captured with the DBB, as described in

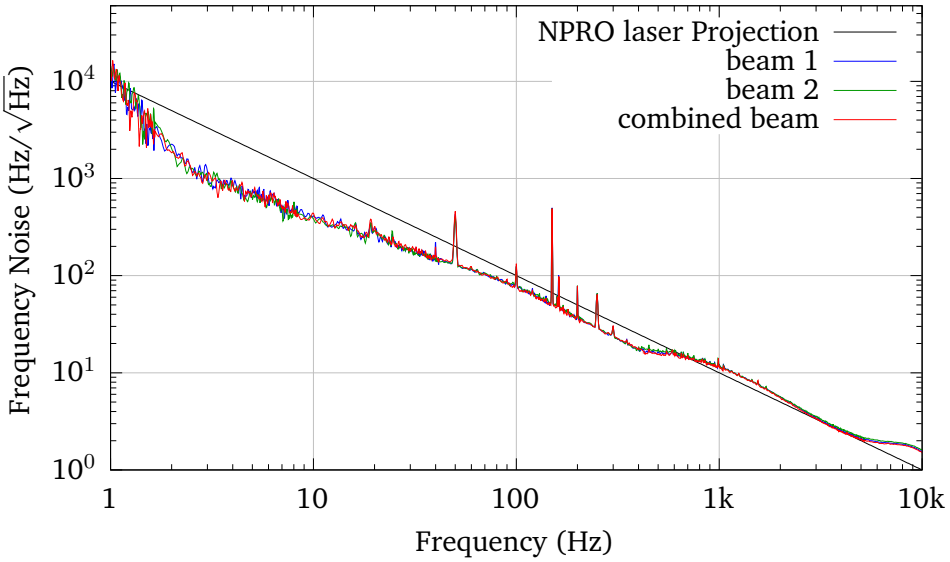

Figure 3.22.: Frequency noise measurements of beam 1, beam 2 as well as the combined laser beam. The NPRO laser projection is shown for comparison. All measurements are captured with the DBB and displayed as ASDs. No significant deviations between the measured curves are visible.

Section 2.2, and presented as ASD over the Fourier frequency in Figure 3.22. All three curves are measured directly after one another with very similar power levels injected to the DBB. They match each other almost perfectly, which is consistent with the assumption that no significant frequency noise is added by the amplifiers and the CBC phase lock control loop.
All curves follow the NPRO laser noise projection, also displayed in the plot, as it is expected when neither the amplification of the seed beams nor the coherent combination add significant frequency noise.

Frequency stabilization

The PSL reference system's frequency stabilization loop described in Section 2.1.4 can be engaged for the here presented system without changes in the locking electronics. The NPRO crystal temperature as well as the PZT attached to the NPRO crystal are used as frequency actuators.
This simultaneous control of the seed laser frequency for both single laser beams is possible if the CBC process does not add frequency noise above the single beams' noise levels. In Figure 3.22, it is shown that this is the case for a free-running frequency noise of the two single beams. With a sufficient CBC phase lock feedback control loop gain, it is also expected that beam 2 follows the instantaneous frequency of beam 1 if the frequency stabilization is engaged.
The frequency stabilization works reliably in the CBC layout. Frequency noise measurements of the free-running and frequency stabilized frequency noise of the combined beam are captured with the DBB and presented in Figure 3.23. A decrease in the noise is clearly visible, but the measurements are limited by the DBB cavity's length noise as in Section 3.1.2. As no additional out-of-loop frequency sensor

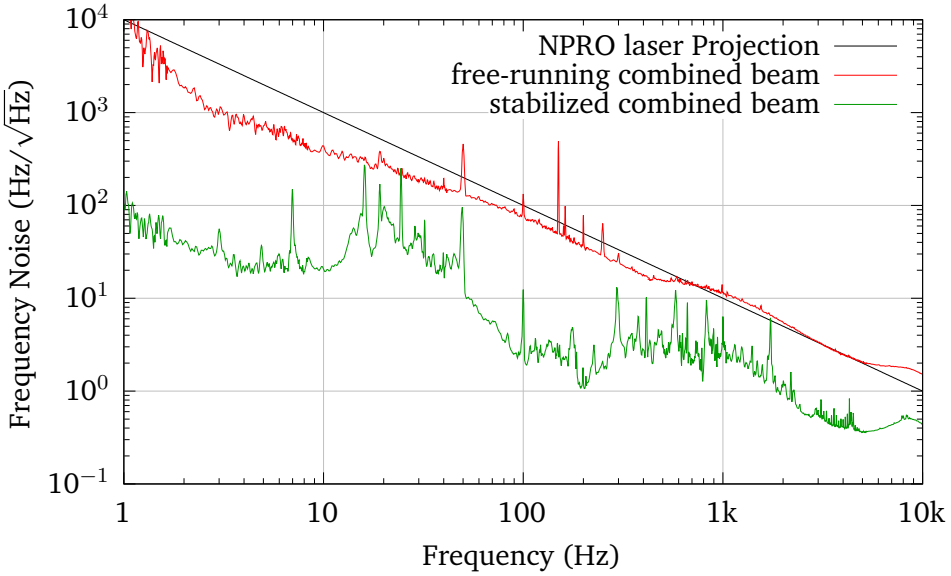

Figure 3.23.: Frequency noise measurements of the free-running and frequency stabilized combined laser beam. A decrease of the stabilized combined beam's frequency noise is visible. The frequency noise measurement is limited by the DBB length noise.

with higher stability than the DBB cavity is available in the reference system, no quantitative statements of the stabilized frequency noise can be made.

Relative pointing noise

In Figure 3.24, the relative pointing noise measurements for the two single beams, as well as the combined beam, are shown. All measurements are captured shortly after one another, with very similar laser power levels for each beam, with the DBB, as described in Section 2.2. The results are displayed as ASD over the Fourier frequency. For clarity, the upper bounds for each beam are represented by the uncorrelated sum of all four curves of relative pointing noise in the solid lines. The four actual measurements, one each for tilt and translation in the horizontal and vertical direction, respectively, are plotted in dotted lines of the same color as the upper bound.
All three upper bounds are very close to each other, indicating that the combination process imprints no additional relative pointing noise above the single beams' noise levels. It also indicates that the relative pointing noise of all beams at most measured frequencies has the same origin.
For uncorrelated relative pointing noise of beam 1 and beam 2, a decrease of the DBB measurement of the combined beam's relative pointing noise in comparison to the single beams is expected. At frequencies below around $20\,\mathrm{Hz}$, a decrease of the relative pointing noise upper bound for the combined beam in comparison to the single beams is visible, which indicates some differential pointing noise between the two single beams at those frequencies. This observation matches the increase in the combined beam's RPN measurements presented in Section 3.2.3 due to differential pointing noise that couples if beam 1 and beam 2 are misaligned.
The noise peak around $70\,\mathrm{Hz}$, which is mainly visible in the measurements of the

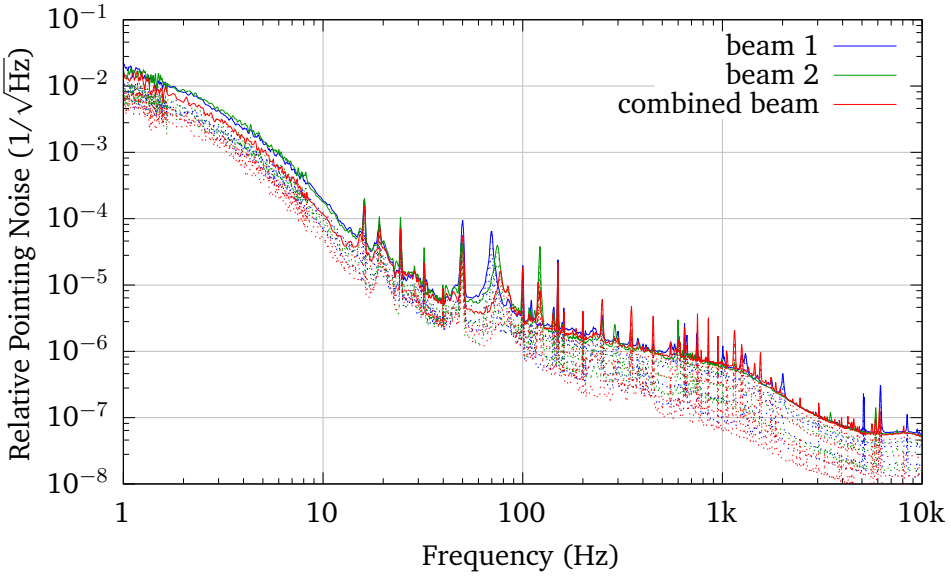

Figure 3.24.: DBB relative pointing noise measurements of the two single beams as well as the combined laser beam. For each curve an upper bound of the four relative pointing measurement is shown as a solid and the actual measurement data as dotted lines.

relative pointing noise of the single beams, most likely has an environmental origin, such as vibrations due to another experiment or an electrical device in the laboratory or building. The environmental perturbations may couple differently to the relative pointing noise of beam 1 and beam 2 prior to their combination and therefore are not correlated.
The overall relative pointing noise performance of all three beams is comparable to and partly even better than the results that were presented for a single amplifier [54], as well as the aLIGO laser system up to the third half of O3 [57], and the following systems [56].

Differential phase noise

Figure 3.25 shows the differential phase noise between the two single laser beams. The differential phase noise measurements are captured with a Stanford Research System SRS785 fast Fourier transform (FFT) analyzer. The generated measurement data is given as ASD in units $\mathrm{V}/\sqrt{\mathrm{Hz}}$ over the Fourier frequency. The calibration curves needed to plot the differential phase noise in units of $\mathrm{rad}/\sqrt{\mathrm{Hz}}$ are presented in Figure 3.26. This measurement is captured originally as a time series of the signal voltages with an oscilloscope. The time signal is calibrated to the differential phase with the CBC locking PD signal. One period of the measured sine signal defines a phase difference of 2π between the single beams. The corresponding measurement time is used to calibrate the x-axis of the plot. With that, Figure 3.26 is shown as a scan of the phase difference between the two single beams. The photodiode signal is inverted and thus the maximum represents the dark fringe operation point for the locking beam splitter port, in this figure.
The high voltage monitoring signal (HV mon) represents the attenuated signal used to drive the differential phase via the PZT driven mirror in the path of beam 2. The

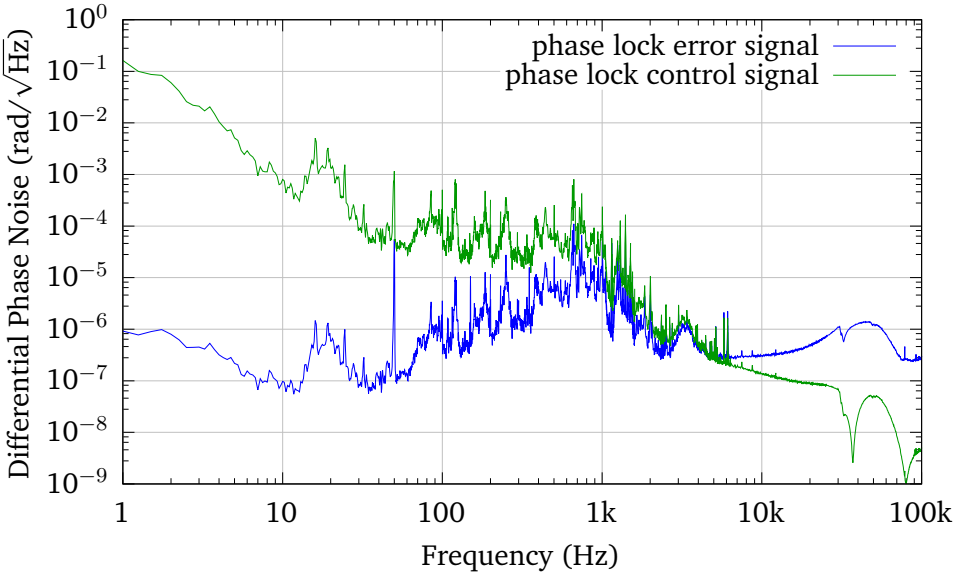

Figure 3.25.: The differential phase noise between beam 1 and beam 2 is described by the CBC phase lock control loops calibrated control signal below and error signal above the unity-gain frequency, respectively. It decreases with the measurement frequency, as expected from earlier measurements.

slope of this high voltage signal in units $\mathrm{Hz\,V^{-1}}$ is transferred to the units $\mathrm{rad\,V^{-1}}$, which is used as the calibration factor for the control signal in the differential phase noise measurement. The control loop error signal has a zero crossing at the dark fringe when the power on the photodiode is minimal. The slope of the error signal at the zero crossing in units $\mathrm{Hz\,V^{-1}}$ is transferred to the error signal calibration factor in units $\mathrm{rad\,V^{-1}}$.
The two calibrated differential phase noise measurements shown in Figure 3.25 cross at the CBC phase lock control loops unity-gain frequency of $5\,\mathrm{kHz}$. The control and error signals give the free-running differential phase noise below and above the unity-gain frequency, respectively. Below the unity-gain frequency, the error signal gives the differential phase noise after suppression by the CBC phase lock loop. Overall the free-running relative phase noise decreases with the measurement frequency insight the measurement band, as expected from earlier publications [73]. At higher frequencies, a saturation effect can be observed in the measurement. This effect can be traced back to the electronical sensor noise of the control loop error signal. The sensor noise is suppressed be the CBC phase lock loop gain below the unity-gain frequency in the in-loop error signal, such that this error signal is not necessarily a good representation of the out-of-loop phase noise.
The feature at about $30\,\mathrm{kHz}$ is caused by a resonance of the PZT driven mirror, which is used as the actuator for the phase lock control loop and is also visible in the control loops open-loop transfer function shown in Figure 3.14.
The differential phase noise between the two single beams couples in the power and frequency noise of the combined beam when it is not suppressed sufficiently. To verify that the used control loop is sufficient, the impact of the differential phase noise on the relative power and frequency noise is mathematically modeled.
For equal single beam laser powers $P_1 = P_2 = P_{\mathrm{in}}$ the laser power of the coherent

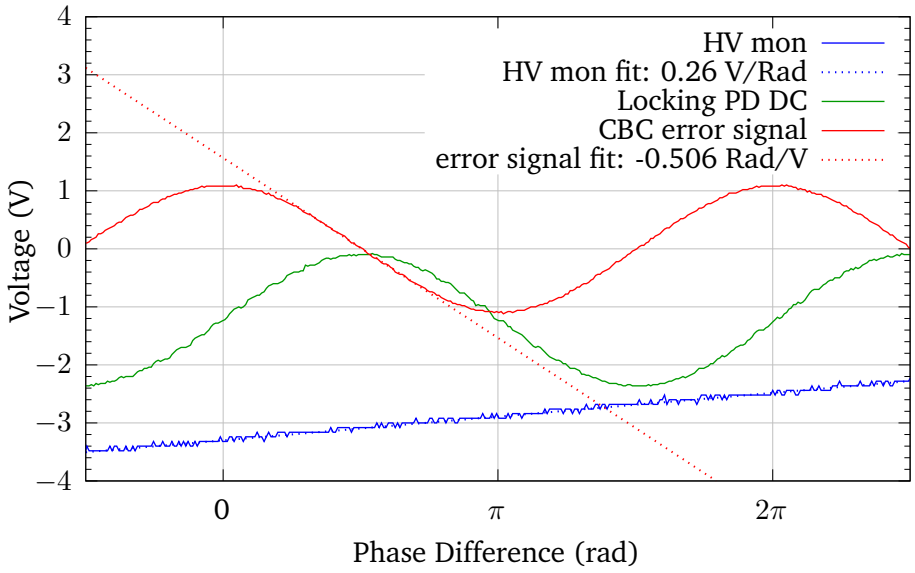

Figure 3.26.: The error signal's differential phase noise contribution is calibrated with the CBC control loop error signal slope and the control signal differential phase noise contribution with the slope of the high voltage amplifier signal sent to the phase actuator, respectively.

combined laser beam P_{CBC} for the assumption of a perfect mode overlap, can be described as (see Appendix A.1):

$$P_{\mathrm{CBC}} = P_{\mathrm{in}}(1 - \sin(\Delta\varphi)). \tag{3.3}$$

To calculate from Equation (3.3) how differential phase fluctuations convert into power fluctuations in the combined beam, the differential phase $\Delta\varphi$ is substituted by $\Delta\varphi = \varphi_0 + \varphi_{\mathrm{m}} \sin(\omega_{\mathrm{m}} \cdot t)$, which includes a phase modulation term with amplitude φ_{m} and frequency ω_{m}.
The phase difference between the single beams at the bright port is $\varphi_0 = (3/2)\pi$. After some simplification Equation (3.3) can be written as:

$$P_{\mathrm{CBC}} = P_{\mathrm{in}}(1 + \cos(\varphi_{\mathrm{m}} \sin(\omega_{\mathrm{m}} \cdot t))). \tag{3.4}$$

Assuming small phase modulations of $\varphi_{\mathrm{m}} \ll 1$, this evolves into:

$$P_{\mathrm{CBC}} = P_{\mathrm{in}}(2 - \frac{\varphi_{\mathrm{m}}^2}{2} \sin^2(\omega_{\mathrm{m}} \cdot t)). \tag{3.5}$$

This can be rewritten as $P_{\mathrm{CBC}} = P_{\mathrm{CBC,DC}} + \Delta P_{\mathrm{CBC}}$, with the DC power $P_{\mathrm{CBC,DC}} = 2P_{\mathrm{in}}$ and the modulation term:

$$\Delta P_{\mathrm{CBC}} = -P_{\mathrm{in}} \frac{\varphi_{\mathrm{m}}^2}{2} \sin^2(\omega_{\mathrm{m}} \cdot t) \tag{3.6}$$

$$= -P_{\mathrm{in}} \frac{\varphi_{\mathrm{m}}^2}{4} (1 - \cos(2\omega_{\mathrm{m}} \cdot t). \tag{3.7}$$

What becomes clear in Equation (3.7) is that a phase modulation at a frequency of ω_{m} drives a power modulation the doubled frequency. The amplitude of the power

modulation depends on the squared phase modulation amplitude, but not on the modulation frequency. Only a noisy transfer function measurement was possible, which, however, seems to be consistent with the calculated coupling.
With the calculated dependency a projection of the differential phase noise to the relative power noise can be performed as shown in Figure 3.27. It is visible that the

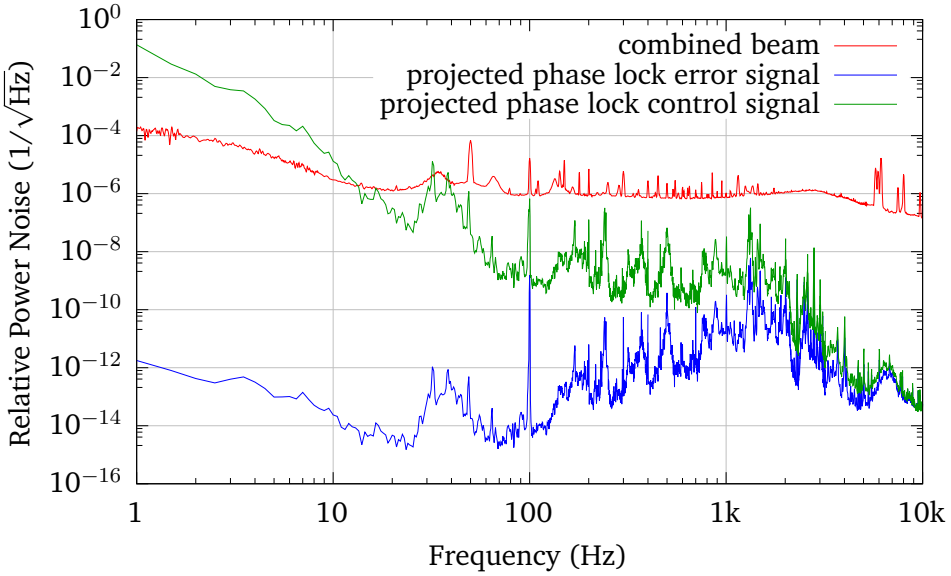

Figure 3.27.: Projection of the differential phase noise to the RPN measurement of the combined beam. The stabilization of the differential phase noise in the CBC feedback control loop prevents it from coupling to the combined beam's RPN.

free-running differential phase noise would couple to the combined beam's relative power noise at low frequencies. At frequencies of $50\,\mathrm{Hz}$ and higher, the decrease of the differential phase noise prevents a coupling. The CBC phase lock feedback control loop suppresses the differential phase noise induced RPN to a factor of 10000 below the RPN of the combined beam. Figure 3.16 confirms that no RPN is added by the combination.
The same mathematical modeling can be performed for the combined beam's frequency noise. The differential CBC phase is described as $\Delta\varphi = \varphi_0 + \varphi_\mathrm{m}\sin(\omega_\mathrm{m}\cdot t)$, as before. The corresponding frequency modulation is derived by calculating the derivative $\Delta\omega = \Delta\varphi/\Delta t$:

$$\Delta\omega = \varphi_\mathrm{m}\omega_\mathrm{m}\cos(\omega_\mathrm{m}\cdot t). \tag{3.8}$$

With $\nu = \omega/2\pi$ this becomes:

$$\Delta\nu = \varphi_\mathrm{m}\nu_\mathrm{m}\cos(\omega_\mathrm{m}\cdot t). \tag{3.9}$$

Hence, a modulation of the differential phase would drive a frequency modulation of the combined beam at the modulation frequency with an amplitude dependent on the modulation amplitude and modulation frequency. As for the RPN, only a noisy transfer function measurement was possible, which, however, seems to be consistent with the calculated coupling. The projected frequency noise curves gen-

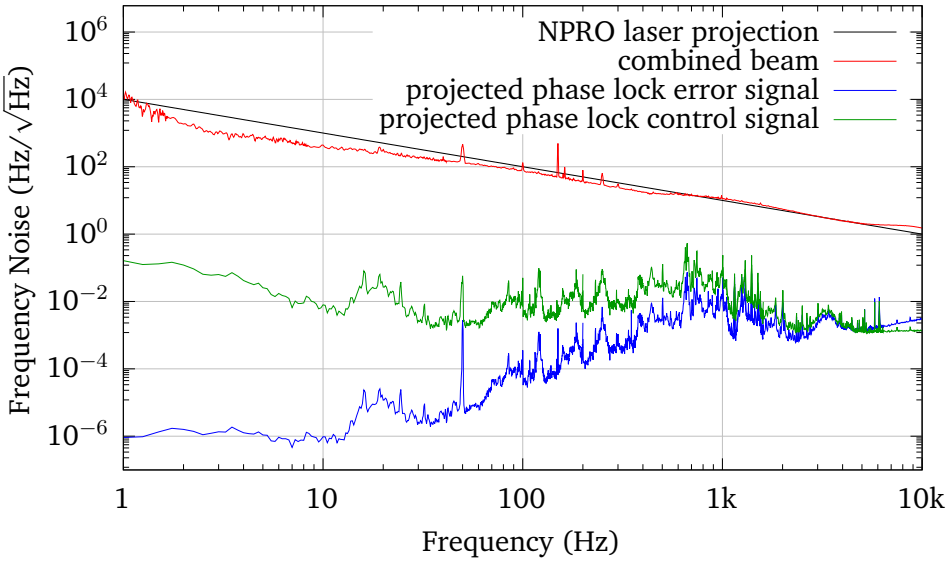

Figure 3.28.: Projection of the differential phase noise to the frequency noise measurement of the combined beam. No coupling from the differential phase noise to the combined beam's frequency noise is expected and can be observed in the measurement band. Nevertheless, a coupling at RF frequencies can be expected.

erated with this calculated coupling are presented in Figure 3.28. The combined beam's frequency noise generated by the differential phase noise is in the measurement range, clearly below the measured combined beam's frequency noise. Which is confirmed in Figure 3.22.
Interesting here could be the behaviour at RF frequencies. If the differential phase noise converted to frequency noise keeps decreasing with the measurement frequency less than the combined beam's frequency noise, it could become dominating at high frequencies. The active frequency stabilization loops described in Figure 2.4 suppress frequency noise up to around a few kHz. The GWD modecleaners as well as the coupled cavity of the power recycling mirror and the arm cavities are passive filters for frequency noise above their pole frequency and up to their FSR frequency and thus suppress the noise partially (see Section 1.2.5).

3.2.4. Conclusion and classification

This section presented a filled aperture CBC of two laser beams amplified by solid-state laser amplifiers in a Mach-Zehnder interferometer configuration. The phase of one of the beams is stabilized to the phase of the other beam in a phase lock control loop, with an unity-gain frequency of about $5\,\mathrm{kHz}$. With two $52.6\,\mathrm{W}$ input beams, a generation of $100\,\mathrm{W}$ in the coherent combined output is demonstrated. The output power in the arm of the interferometer that includes an EOM is limited by the maximal power that can be guided through this EOM. For the used layout designed to combine equal power levels on a $50/50$ beam splitter, this limits also the total power level. For future experiments in a similar layout, it is thus recommended to use a different EOM material or to enable the combination of different power levels by using a variable beam splitter design as it will be explained in Sec-

tion 3.4.
The CBC laser system is integrated in the aLIGO PSL reference system, which is a very realistic environment for the system's characterization regarding its suitability for GWDs.
The higher order mode content of the combined laser beam presented in Section 3.2.3 improves compared to the two single beams due to destructive interference between and different power levels of the single beams' HOMs. This effect can be beneficial in the usage of GWDs as it decreases the power that has to be filtered at the pre-mode-cleaner (see Section 1.2.3), but it doesn't change the total power loss. About $2\,\mathrm{W}$ loss of the total $5.2\,\mathrm{W}$ between the sum of the single beams and the combined beam can be explained by this effect. The additional $3.2\,\mathrm{W}$ could be explained by a non-perfect contrast of the Mach-Zehnder interferometer due to a slight mode-mismatch between the two single beams, especially in the waist position and size along the propagation axis.
The combined beam's relative power noise is characterized in detail and understood well on the basis of theoretical modeling. A mixture of correlated and uncorrelated noise has to be assumed to describe the combined beam's relative power noise, which is above frequencies of $20\,\mathrm{Hz}$ always below or on the same level as the single beams. Additional noise at low frequencies is most likely due to coupling from stray light.
The installation of a simple auto-alignment control loop based on differential wavefront sensing confirms the consideration that the combined beam's relative power noise increases when the single beams are misaligned because, in that case, differential pointing noise couples to the relative power noise.
There are two approaches to handle a possible increase in relative power noise due to drifting alignment for the usage of coherent combined systems in GWDs. The first option is to install an auto-alignment loop as it is presented in this thesis. This solution would require additional feedback control loops, which on the one hand make the system more complex but on the other hand are proven technology. It is also beneficial that the existing phase sidebands, that are used for the coherent combination phase lock loop, can be reused in a differential wavefront scheme as presented here.
The second option is to ensure a precise and long term stable alignment by choosing the initial alignment as precise as possible and choose stable mirror mounts. As the combined laser system would be integrated in the GWDs power stabilization systems, a sufficient suppression in the power stabilization feedback control loops, can most probably compensate for a slightly increased power noise at low frequencies, if needed.
The power stabilization within the reference system uses two current shunts in the solid-state laser amplifier in one of the laser arms. This configuration is very similar to how it is used with just one amplification chain and should also be applicable if more than two beams are combined, as it will be presented in Section 4.1. The stabilization electronics are optimized for this actuator and are still linked to the CDS, which allows a usage of the digital control. The power stabilization feedback control loop performance is comparable and, at some frequencies, even better compared to earlier experiments with only one amplifier with a current shunt and AOM as actuator [54, 57].
No additional frequency noise was added in the coherently combined beam compared to the two free-running single laser beams. As it is expected if the same laser

source is used for both arms and one arm is phase locked to the other, the two single beams' and the combined beam's frequency noise follow almost the same curves. The frequency noise is close to the projected NPRO laser frequency noise. The reference system's frequency stabilization is engaged with the actuators located in the frontend laser system before the beam is split in the two Mach-Zehnder interferometer arms. The locking procedure to the reference cavity is the same as for a single amplifier. The frequency noise measurement captured with the DBB is limited by the DBB cavity's length stability as it is expected from earlier measurements. Nevertheless, it is the only measurement that can be captured in the reference system as no other out-of-loop frequency sensor is available. The high performance of the stabilization in this configuration further confirms, that the frequency noise of the two single beams and the combined beam is dominated by the frontend NPRO laser.
Also, the combined beam's relative pointing noise behaves as expected. It is below or equal to the two single beam pointing noise measurements at all measured frequencies. The measurement allows the conclusion that the single beams' RPNs are mostly correlated. At low frequencies, a slight decrease in the combined beam's relative pointing noise can be a hint for uncorrelated noise, which fits to the conclusion on the relative power noise measurements.
In the last part of the laser system characterization, the differential phase noise measurement is presented. The measured differential phase noise is projected to the combined beam's RPN and frequency noise to identify its possible impact on them. The differential phase noise decreases with increasing measurement frequency, as it was shown for an earlier CBC experiment presented in [85]. Above the unity-gain frequency, the error signal sensor noise limits the measurement.
A coupling of the frontend laser beam's frequency noise to the differential phase noise via arm length differences in the Mach Zehnder interferometer is not expected in this layout. This expectation follows from another CBC experiment performed in the scope of this thesis and presented in Figure 3.37. There the arm length difference is about $40\,\mathrm{m}$, which highly exceeds the $<0.5\,\mathrm{m}$ in the here presented layout. No coupling is observed in the system that is presented in Figure 3.37 and thus, also no coupling is expected here.
Theoretical considerations, confirmed by transfer function measurements, allowed a comparison between the measured relative power or frequency noise and the expected relative power or frequency noise generated by the differential phase noise, respectively. The noise projections confirm that the CBC phase lock control loops gain is sufficient to suppress the relative power noise generated by the differential phase noise far below the free-running relative power noise of the combined beam. At high frequencies, the decrease of the differential phase noise with the measurement frequency ensures that the coupling to the relative power noise is not dominant in the measurement range.
Similar projections are computed for the combined beam's frequency noise and confirmed with a transfer function measurement. The projected noise is well below the combined beam's measured frequency noise in the measurement range. At high frequencies it could be expected though, that the frequency noise generated by the differential phase noise becomes limiting. This effect should be further investigated in future CBC experiments. The GWD frequency stabilization control loops suppress this noise in their control range, but an increased loop gain might be needed. For frequencies between their pole frequency and FSR also all mode-

cleaners as well as the coupled cavity between the power recycling mirror and arm cavities in the GWDs act as passive filters for frequency noise [37, 47].
Summarizing, this work presents the first stabilized laser system based on a CBC scheme. The system's performance is comparable to the current and past aLIGO laser system and in some parameters even better [54, 57]. Noise couplings due to the CBC are well understood and the theoretical considerations meet the experimental data.
Based on these results, follow up research can be performed to increase the laser power. This could be realized, for example, by using two solid-state laser amplifiers or high power fiber laser amplifiers in each arm, as demonstrated in Section 3.3. Additionally, a combination of more than two laser beams could be performed in different configurations, as presented in a proof-of-principle experiment in Section 4.1.
An alternative approach would be the coherent combination of two laser beams from independent laser sources, as described briefly in Section 3.4. This layout could be beneficial for the systems reliability as even if one system fails, the other one could still be used to keep the GWD operating. A drawback could be the increased system complexity, as not just the phase but also the frequency between the two single beams would need to be stabilized.

3.3. Coherent combination of two beams amplified by fiber laser amplifiers

Fiber laser amplifiers are a promising technology to increase the laser power above the level that can be reached with solid-state laser amplifiers, as it is discussed in Section 1.3.1. In this section, a laser system based on the coherent combination of two laser beams amplified by fiber laser amplifiers in a Mach Zehnder interferometer configuration, similar to the system presented in Section 3.2, is investigated. This project is a cooperative work with the Laser Zentrum Hanover e.V. and was assembled in one of their laboratories. The results that are presented in this section are to great extent published in the PhD Thesis of Felix Wellmann [75] and the shared corresponding author paper [74].
The layout phase lock control loops of the experiment will be described in Figure 3.29 and Figure 3.30. It follows a characterization of the combined beam in comparison to the single beams in Section 3.3.3. At the end of this section a conclusion and classification of the work, as well as an outlook into the next steps for the research, are given in Section 3.3.4 and Section 3.3.5.

3.3.1. Experimental layout

A simplified schematic of the fiber laser amplifier coherent beam combination (CBC) system is depicted in Figure 3.29. A 2 W NPRO laser at a wavelength of 1064 nm serves as seed laser for the system. Its laser beam is split in two equal

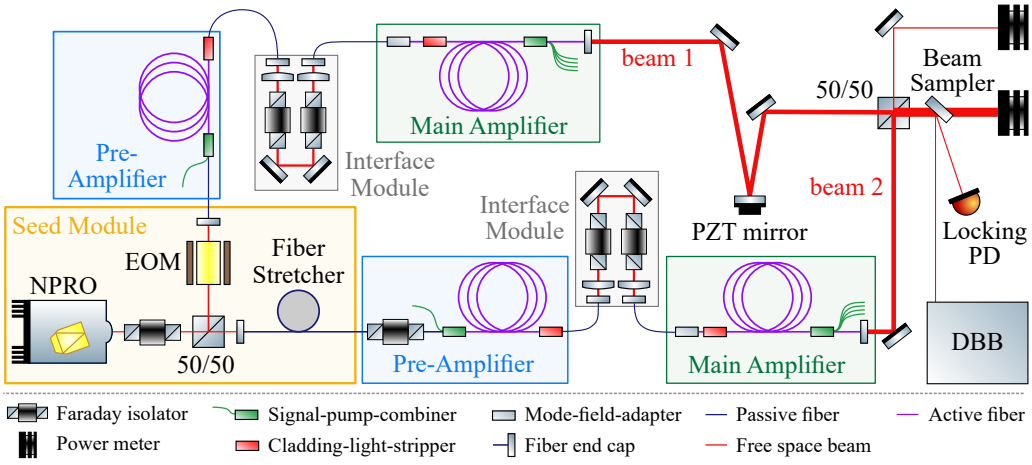

Figure 3.29.: Two laser beams from the same seed source amplified by fiber laser amplifiers are combined in a Mach-Zehnder configuration. The DBB cavity serves as alignment and mode matching reference for both beams and the combined beam is characterized with the DBB.

parts by a 50/50 beam splitter. The first part is called beam 1 and the second part beam 2 in the following. Beam 1 is guided through an EOM and fiber coupled. Beam 2 is fiber coupled to a fiber stretcher which is used as low frequency phase actuator.
Each beam is then send to a fiber pre-amplifier, a free-space interface module and a fiber main-amplifier. All modules are developed by the Laser Zentrum Hannover e.V. in close collaboration with the Albert Einstein Institute Hanover. The used

fiber laser amplifier systems are characterized and long-term tested at the Laser Zentrum Hannover e.V., and the corresponding results are published in [59, 60]. The amplifiers used in this experiment are amplifier 2 and amplifier 4 from [60].
The pre-amplifiers consist of Ytterbium doped active fibers that are forward pumped with $30\,\mathrm{W}$ laser diodes at a wavelength of $1064\,\mathrm{nm}$ via the signal-pump combiners. Residual cladding light is removed with cladding-light-strippers. Two Faraday isolators that protect the pre-amplifiers from back reflections are parts of the free-space interface modules. Each of the main-amplifier's first component is a mode-field-adapter, to match the passive incoupling fiber's diameter to the larger active fiber's diameter. The active fiber consists of Ytterbium doped fused silica similar to the pre-amplifier. It is backward pumped with up to two pump laser diodes with maximal $150\,\mathrm{W}$ output power at a wavelength of $976\,\mathrm{nm}$ for beam 1 and up to 3 pump diodes with the same specifications for beam 2. To avoid that stimulated Brillouin scattering limits the maximal laser power, the fiber length of the main amplifier is effectively separated in two parts by inducing a thermal gradient as described in Section 1.3.1. Therefore, the first part of the fiber is on a spool with $40\,^{\circ}\mathrm{C}$ and the second part on a spool with $15\,^{\circ}\mathrm{C}$. Both spools are located above each other.
Both main amplifiers deliver a laser power of $200\,\mathrm{W}$ with a PER of $>20\,\mathrm{dB}$. Beam 1 is guided to a PZT driven mirror. This mirror is used as fast phase actuator. It is installed under a small angle of incidence to avoid a vertical or horizontal displacement of the reflected beam due to the actuation. Both beams are then guided to the two input ports of the combining $50/50$ beam splitter. The three mirror cavity insides the DBB, described in Section 2.2, is used as alignment reference for the two laser beams. By aligning both beams separately to the DBB, an initial spatial overlap between them is provided. As thermal effects couple to the alignment if the beams are combined, a final alignment optimization is performed while the beams are combined at full power. The differential phase between the two laser beams is stabilized in a phase lock feedback control loop in order to produce a dark and a bright output port. The corresponding components and loop design are described in Section 3.3.2. The beam splitter's bright output port is called the combined beam. A small fraction of the combined beam is guided to the DBB for characterization.

3.3.2. The CBC phase lock loop

The spectral coherence between beam 1 and beam 2 is obtained with a phase lock feedback control loop. All important components of the control loop are displayed as a simplified schematic in Figure 3.30. A combined beam with maximal power is generated by stabilizing the differential phase between the two single laser beams to the bright fringe of the Mach-Zehnder interferometer. The phase stabilization scheme is very similar to the one described in Section 3.2.2. Phase sidebands at a frequency of $12\,\mathrm{MHz}$ are imprinted on beam 1 with the EOM via the local oscillator (LO) voltage signal. The locking photodiode (PD) senses a small portion of the bright port laser beam, and its signal is demodulated with the LO signal at the mixer to provide a linear error signal at the bright fringe. The mixer is directly followed by a low-pass filter to suppress residual signals at the modulation frequency, which is not shown in Figure 3.30 for simplicity.
The error signal is filtered and amplified in an analog servo. The resulting control signal is fed back to the PZT driven mirror and the fiber stretcher. The fiber

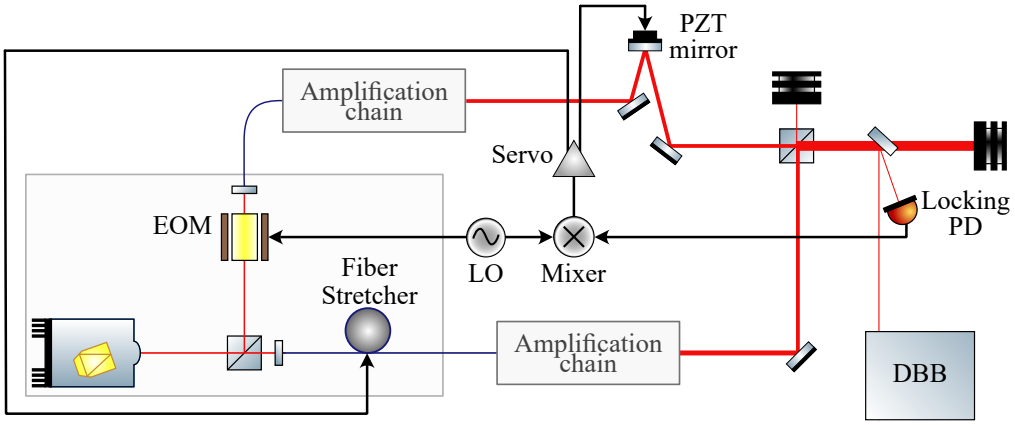

Figure 3.30.: A photodiode at the combining beam splitter's bright output port is used as sensor for the CBC phase lock loop. Its signal is demodulated, filtered and amplified and then feed back to the PZT driven mirror for fast and the fiber stretcher for slow phase actuation, respectively.

stretcher (OPTIPHASE, PZ2-PM2) has a fiber length of about $40\,\mathrm{m}$ and a maximum optical path length displacement of $2240\,\mu\mathrm{m}$. It is used as phase actuator up to Fourier frequencies of about $10\,\mathrm{Hz}$. It's first resonance at $18\,\mathrm{kHz}$ is suppressed by low-pass and notch filters as otherwise the large induced phase shifts of more than $30\,\mathrm{rad\,V^{-1}}$ could couple to the phase control at high frequencies. For frequencies higher than $25\,\mathrm{Hz}$ the PZT (PI, P-010.05H) driven mirror is used as phase actuator. The PZT's first resonance frequency as specified by the manufacturer without the

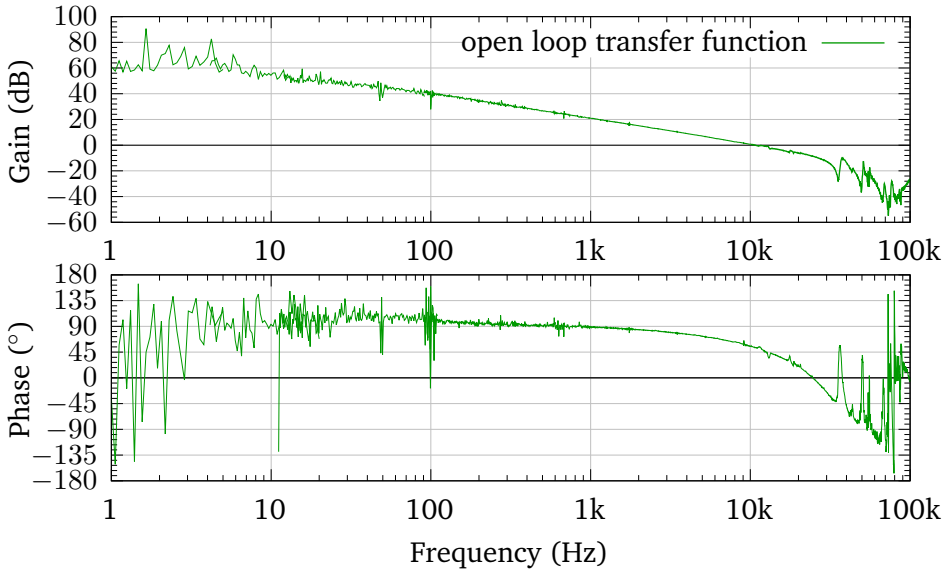

Figure 3.31.: Open-loop transfer function of the CBC phase lock control loop. The unity-gain frequency is located at $10\,\mathrm{kHz}$ with a gain margin of $8.6\,\mathrm{dB}$ and a phase margin of $53°$. Modified figure from [74].

mirror and mounting is at about $84\,\mathrm{kHz}$. In the experimental layout, including the mirror and mounting, it is measured to be at $35\,\mathrm{kHz}$ similar to the PZT used in Sec-

tion 3.2.2. The servo controller is designed to suppress the resonance by low-pass and notch filters.
The control loop open-loop transfer function is depicted as a Bode plot in Figure 3.31. A unity-gain frequency of $10\,\mathrm{kHz}$ with a gain margin of $8.6\,\mathrm{dB}$ and a phase margin of $53°$ is reached in the presented layout. The fiber stretcher's and PZT's first resonances are suppressed below unity-gain. The PZT's resonance limits the control loop bandwidth. The increased measurement noise at low frequencies can be traced back to a limited averaging time.

3.3.3. Characterization of the combined laser beam

The coherently combined laser beam generated in the described experiment is characterized under different aspects. In this section, first, the generated power level and corresponding combination efficiency are presented. The spatial beam profile as well as the laser noise of the combined beam are measured with the DBB and a FFT analyzer and characterized in comparison with the corresponding measurements for the single beams. Finally, the differential phase noise of the two single beams is measured, and the potential coupling of the seed laser's frequency noise to it is described.

Combined power and combining efficiency

Figure 3.32 shows the laser power of the combined beam and the dark port relative to the total laser power, which is derived by the sum of the two single beam powers. The dotted lines are linear fits for the combined and dark port power, which visualize the linear gradient of the curves. Additionally, the combining efficiency is

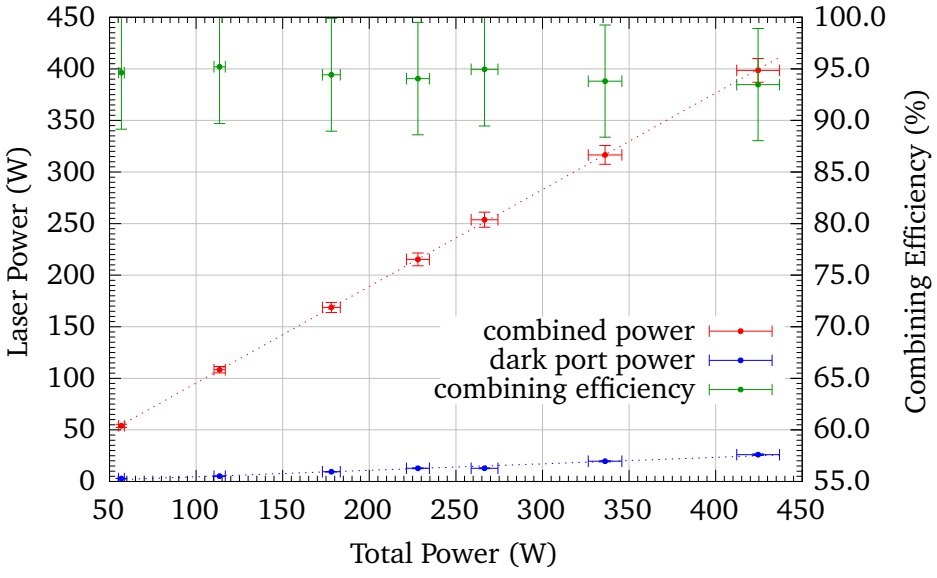

Figure 3.32.: Combined power, dark port power and the resulting combining efficiency in relation to the total input power present at the combining element. The combined power scales linear with the total power and a combining efficiency from $93.5\,\%-95.2\,\%$ is reached. Modified figure from [74].

plotted in percent in the figure. It is calculated by dividing the combined power by the total power. The power measurements of the single beams and the combined beam are performed with high power thermal power meters. The errors of about $\pm 5\,\%$ in the combining efficiency are a result of the error propagation from the thermal power meter signals.
The combined power scales linear with the input power, and the combining efficiency is nearly constant at a level between $93.5\,\%$–$95.2\,\%$. A maximal combined laser power of $398\,\mathrm{W}$ with a corresponding combination efficiency of $93.8\,\%$ is reached in this layout. Losses can be attributed to a alignment and mode mismatches between the two single laser beams, as well as potential offsets in the locking electronics.
A two hour long continuous operation didn't show a degradation in the combined laser power. During this measurement time, power variations of less then $2\,\%$ root mean square (RMS) are detected [74].

Spatial beam profile

The HOM content of the combined beam and the two single beams (beam1 and beam2) are measured with the DBB, as described in Section 2.2, and plotted in relation to the beam power in Figure 3.33. Due to possible alignment and mode mismatches to the DBB, the measurements have to be considered as upper limit for the beam's HOM content. The single beam power scale is depicted on the upper and the combined beam scale on the lower side of the picture, respectively. The scales are chosen to have a factor of two between them to allow for a direct comparison between the HOM contents of the single beams and the combined beam at the related power levels. It is visible that the HOM content of all three beams increases

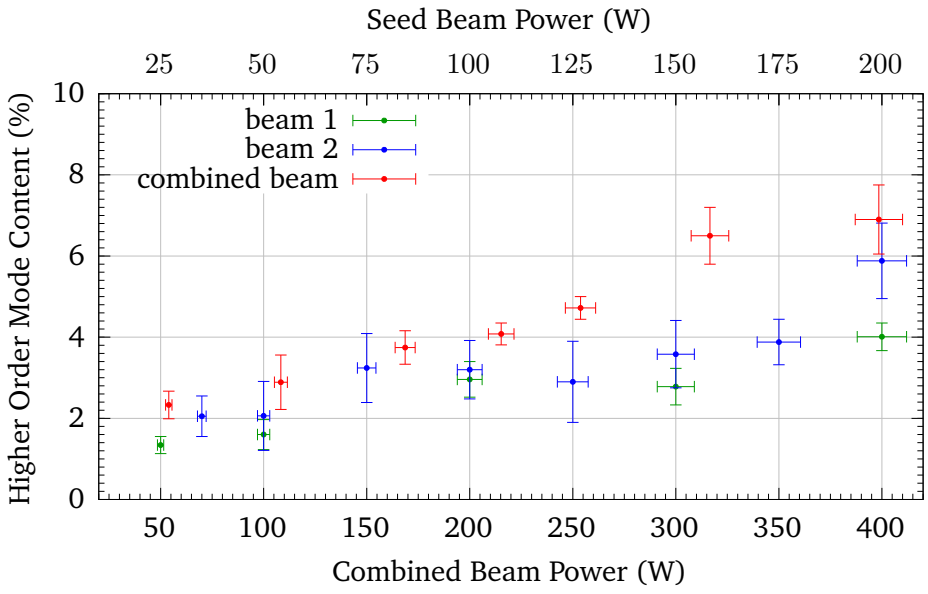

Figure 3.33.: The HOM content of the combined beam and single beams is plotted in relation to the beam power. A scaling between the axes allows for a direct comparison between single and combined beam. The combined beam's HOM content increases compared to the single beams with increasing laser power. Modified figure from [74].

with increasing power. That the HOM content of the combined beam increases stronger than the single beams could be caused by thermal effects on the combining element due to the high laser power. Thermal lensing or a thermal degradation of the combining $50/50$ beam splitter and all components in the high power path afterward, can lead to an increased ellipticity or a deformation of the combined beam's spatial profile.
The total HOM stays below $6.9\,\%$ in the measurement. Therewith a maximal output power of more than $370\,\mathrm{W}$ in a linear polarized TEM_{00} is generated.

Relative power noise

The relative power noises (RPNs) of the combined beam and the single beams are sensed with a photodiode and captured with a Stanford Research Systems SR785 FFT analyzer. All measurements are presented as ASD over the Fourier frequency in Figure 3.34. For the used fiber laser amplifiers it is expected that the pump diode power noise dominates at low and the seed power noise at high frequencies, respectively [85]. But even with a strong attenuation of the pump diode power noise at high frequencies, a coupling is still possible. The slightly different RPN curves for the two amplifiers can most likely be explained by a slightly different pump diode noise for the two amplifiers. The irregularity around $1\,\mathrm{kHz}$ in the beam 1 RPN measurement is most likely due to time depending external noise couplings, which is assisted by the fact that it doesn't show up in the combined beam's RPN.
The combined beam's RPN measurement is at all frequencies at a similar level as

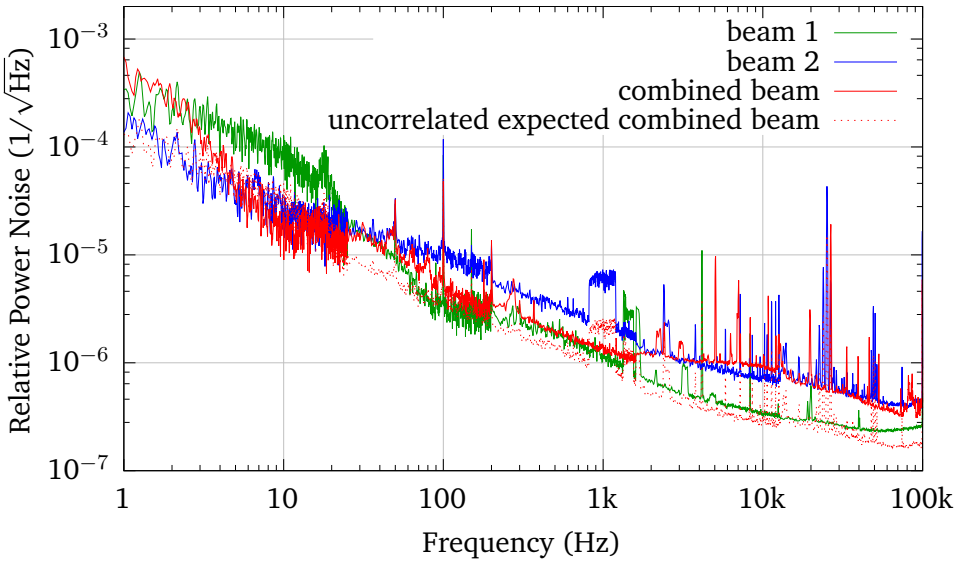

Figure 3.34.: RPN of the two single beams and the combined beam as well as a projection of the combined beam's RPN if the noise origin is uncorrelated. Modified figure from [74].

that of the two single beams. For a purely uncorrelated RPN of beam 1 and beam 2 an uncorrelated summation is expected like explained in Section 3.2.3 and derived in Appendix A.2. The theoretically expected curve for this case is also plotted in Figure 3.34 as a dotted line. At frequencies between $5\,\mathrm{Hz}$ and $20\,\mathrm{Hz}$ as well as $100\,\mathrm{Hz}$ and $1\,\mathrm{kHz}$ the combined beam's RPN is close to the expected noise for un-

correlated RPN contributions of beam 1 and beam 2. The increase at frequencies above $1\,\mathrm{kHz}$ could be due to external perturbations that couple to the measurement, which is assisted by the fact that the noise behaviour is not stationary at that frequency range in between replied measurements. At around $30\,\mathrm{Hz}$ the combined beam's RPN is at the same level as that of the two single beams. Here the RPN could be from an external origin or the seed laser and thus correlated for the three measurements. The increase in the combined beam's RPN at frequencies below $5\,\mathrm{Hz}$ can most likely be explained by stray light that couples to the sensor as explained in Section 3.2.3.
All three measurement curves are measured with slightly different optical components. Hence, a coupling from the optical components resonances and different external perturbations can not be excluded as a possible reason for additional deviations in the three noise curves.

Frequency noise

The frequency noise of all three beams is measured with the DBB, as described in Section 2.2 and shown as ASD over the Fourier frequency in Figure 3.35.
It is not expected that the two fiber laser amplifier chains add frequency noise, which is higher than the noise of the free-running seed laser. Hence, it is expected

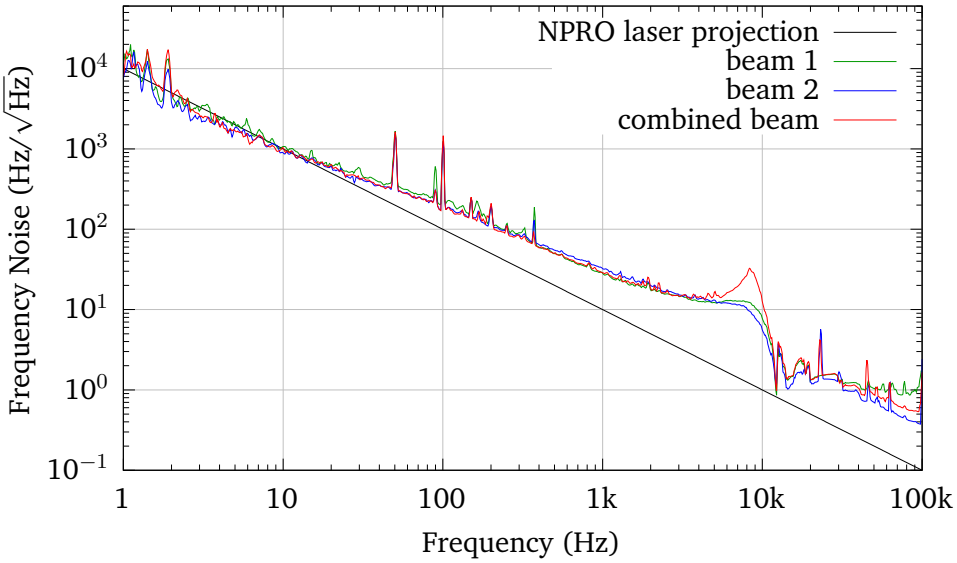

Figure 3.35.: The frequency noise curves of the two single beams and the combined beam are close to the projected NPRO laser frequency noise and very close to each other. Modified figure from [74].

that the frequency noise of beam 1 and beam 2 is at a very similar level close to the NPRO laser noise projection, which is visible in the measurements. The broad bump in all three measurements at around $8\,\mathrm{kHz}$ results from a slightly low phase margin and thereby a servo bump of the DBB cavity length control loop. The small increase in the frequency noise of beam 2 above $50\,\mathrm{kHz}$ is most likely a measurement artifact or a coupling from environmental perturbations.
The combined beam's frequency noise is at the same level as that of the two single beams as it is expected for a sufficiently stable CBC phase lock control loop as

explained in Section 3.2.3. Only the bump around $8\,\mathrm{kHz}$ is a bit higher which can again be traced back to the DBB electronics and not the laser frequency noise.

Relative pointing noise

The relative beam pointing noise of all three laser beams is measured with the DBB, as described in Section 2.2, and plotted as ASD over the Fourier frequency in Figure 3.36. For simplicity, the uncorrelated sum of the four measurements per beam is plotted as solid and the measurements itself as dotted lines, respectively.
For a pure phase actuation of the PZT it is not expected that relative pointing noise is added by the CBC phase lock control loop. A uncorrelated or correlated summation of the relative pointing noises is expected depending if it has the same or independent coupling origins in the amplifier beam paths of beam 1 and beam 2, as explained in Section 3.2.3. At a closer look on the four single relative pointing noise

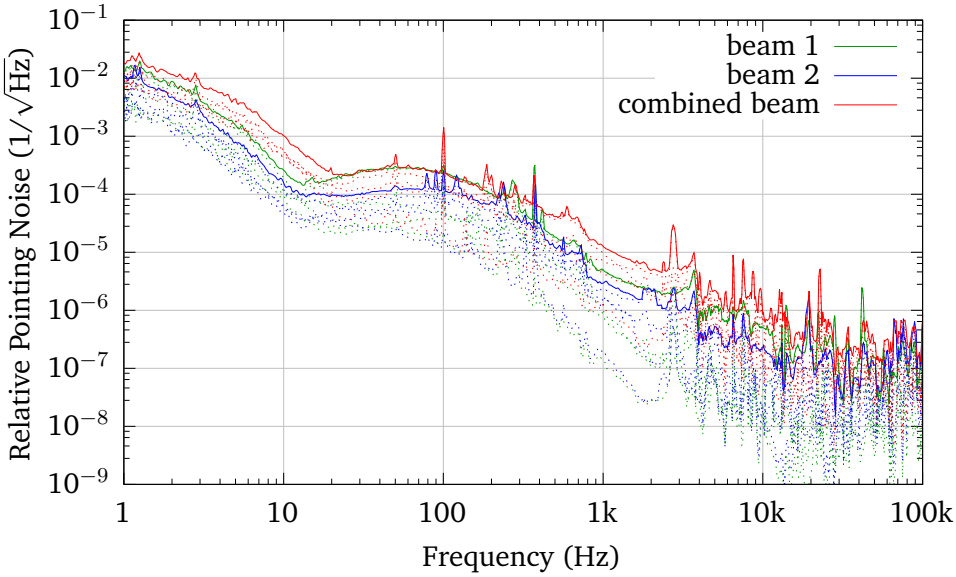

Figure 3.36.: Relative pointing noise measurements of the single beams and the combined beam. The solid line represents the uncorrelated sum of the four noise curves for each measurement. The dotted lines show the individual four curves per measurement. Modified figure from [74].

measurement curves of beam 1 and beam 2, it turns out that the measurement for one vertical direction in both beams is about one order of magnitude lower than the other measurements. Additionally, the increase of the relative pointing noise from beam 1 compared to beam 2 above $10\,\mathrm{Hz}$ can be traced back to an increased pointing in one of the horizontal directions of beam 1, which could origin from the mounting of an optical component in its beam path.
The combined beam's relative pointing noise measurement is at all frequencies similar to the upper curve of beam 1 and 2 or maximal a factor 2 above it. Here, the measurement for the same vertical direction as for the single beams is the lowest. The other three measurements are on a similar level.
The increase in the combined beam's relative pointing noise compared to that of the single beams at frequencies below $20\,\mathrm{Hz}$ and above $200\,\mathrm{Hz}$ could, for example,

be related to environmental perturbations that change in between the measurements. This increase is visible in all four single measurements for the combined beam. Couplings of PZT driven mirror phase actuation to the relative pointing noise in beam 1 are, for geometry reasons, expected to appear only in the horizontal directions and are, therefore, no valid explanation for the increased noise of the combined beam.

Differential phase noise

The differential phase noise between the two single laser beams can be measured via the control and error signals of the CBC feedback control loop. In Section 3.3.2, it is described that the phase lock control loop uses two phase actuators. A fiber stretcher is used for low frequency phase drifts, and a PZT assisted mirror for fast phase fluctuations. Thus, the differential phase noise measurement contains both

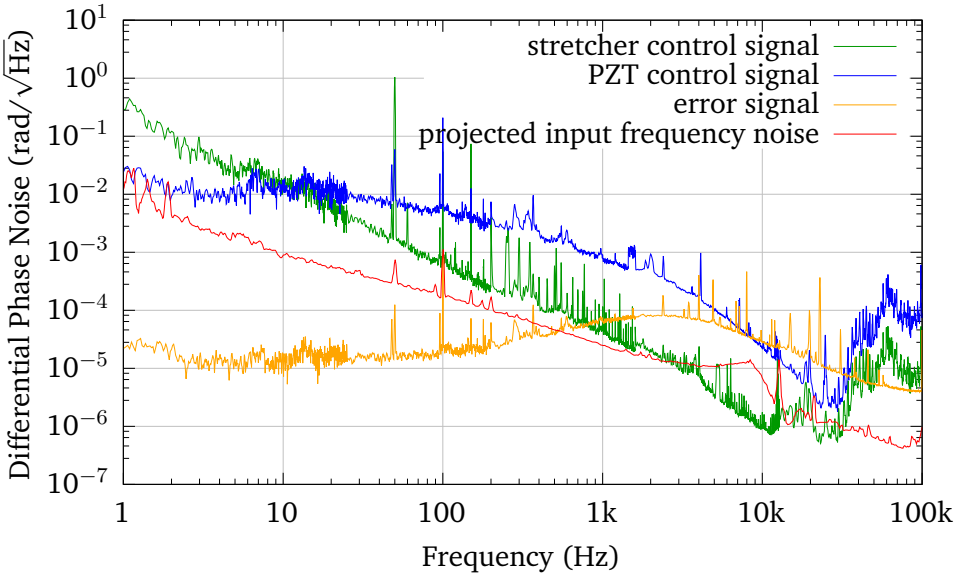

Figure 3.37.: The differential phase noise is described by the calibrated control and error signals of the CBC phase lock loop. The laser source frequency noise does not dominate the differential phase noise. Modified figure from [74].

corresponding control signals. All signal are measured with a FFT analyzer and plotted as ASD over the Fourier frequency in Figure 3.37. Similar to the measurements in Figure 3.25, the original measurement curves have the unit $\mathrm{V}/\sqrt{\mathrm{Hz}}$, and are, therefore, calibrated. The stretcher and PZT control signals are each calibrated with their drivers slope and the error signal is calibrated with the slope of the control coherent beam combination error signal at the bright fringe. All calibration factors have the unit rad/V, as described in Figure 3.37.
The fiber stretcher control signal stabilizes the phase up to a frequency of about $10\,\mathrm{Hz}$. Therefore, the stretcher control signal corresponds to the free-running differential phase noise up to this frequency. From $10\,\mathrm{Hz}$ up to the feedback control loops unity-gain frequency of about $10\,\mathrm{kHz}$, the PZT assisted mirror stabilizes the differential phase. Therefore, the PZT assisted mirrors control signal displays the free-running differential phase noise in that frequency regime. The control

loops error signal represents the free-running phase noise at frequencies above the feedback control loops unity-gain frequency. The measurement of the error signal below the control loops unity gain frequencies shows the differential phase noise suppressed by the feedback control loop.
The total free-running differential phase noise follows a similar behaviour as presented in earlier publications [85] as well as the results generated in Section 3.2.3. The two Mach-Zehnder interferometer arms have an arm length difference of about $40\,\mathrm{m}$ due to the implemented fiber stretcher in the path of beam 2. Additional arm length difference due to the optical layout are below $0.1\,\mathrm{m}$. As described for gravitational wave detectors in Section 1.2.5, arm length differences in an interferometer could lead to a coupling of the laser frequency noise to the differential phase noise. To investigate this effect, the laser frequency noise is projected to the differential phase noise and depicted as additional curve in Figure 3.37. The magnitude of the coupling is calculated with the assumed arm length difference of $40\,\mathrm{m}$.
It is visible that the projected frequency noise is below the free-running differential phase noise in the measurement range and therefore does not influence the coherent combination.

3.3.4. Conclusion and classification

A CBC experiment of two laser beams from the same laser source amplified by fiber laser amplifiers in a Mach-Zehnder interferometer configuration is presented in this section. A combined laser power of $398\,\mathrm{W}$ with a combining efficiency of $93.8\,\%$ could be reached in the presented layout with a feedback control loop with a bandwidth of $10\,\mathrm{kHz}$. This marks highest so far measured laser power of a system with the aim to be suitable for ground-based GWDs.
A small increase of the HOM content of the combine beam in comparison to the two single beams can most likely be explained by thermal effects on the optics in the high power laser beam path. The reached HOM content below $6.9\,\%$ at the maximal combined power is still in the range of current GWD laser systems [56]. This results in more than $370\,\mathrm{W}$ in a linear polarized TEM_{00} laser mode.
The combined beam's RPN is close to that of the two single laser beams. It has to be pointed out that the RPN of laser beams amplified by fiber amplifiers is increased comparison to solid-state laser amplified systems as the pump diode noise dominates up to certain frequencies. This increase is smaller than an order of magnitude. The measured curves are still very close or even improved to what is shown for the free-running laser systems used in aLIGO up to the third observing run [56, 57]. Thus, it can be expected that the power stabilization described in Section 2.1.3 can be used for a system like this, as well.
The frequency noise of the combined laser beam is very similar to that of the two single beams, and to the expected NPRO laser frequency noise projection. It is also very similar to the frequency noise of previously used laser systems for GWDs. This makes it promising that the GWD frequency stabilization systems, as presented in Section 2.1.4 can be used for this system as well.
Also the relative beam pointing noise of the combined beam is very close to that of the two single beams. Small increases could be related to environmental perturbations that change in between the measurements. In comparison to current GWD laser systems [56] and the solid-state laser amplifier based laser systems presented in Section 3.1 and Section 3.2, the measured relative pointing noise is slightly

increased between frequencies of $10\,\mathrm{Hz}$ to $10\,\mathrm{kHz}$. This can be due to higher environmental noise that couples in the relative pointing noise. For example the water cooling system needed for the amplifiers is installed inside the laboratory for the presented experiment, which is not the case at the GWDs as well as the laboratories at the Albert Einstein Institute used for the experiments presented in Section 3.1 and Section 3.2. The cooling devices make high acoustic noise and can also generated vibrations that couple to the laser table.
The differential phase noise measurement substantiates the understanding of the feedback control loops. Moreover, a projection of the laser sources frequency noise to the differential phase noise showed no significant coupling despite the interferometers arm length difference of $40\,\mathrm{m}$.

3.3.5. Outlook

The next steps in the development of a coherent beam combined GWD laser system with $400\,\mathrm{W}$ or more of output power is its integration in a PSL environment.
A very similar system to the presented one is already under construction in the PSL reference system environment of the Albert Einstein Institute Hanover, which is described in Chapter 2. It will use an eLIGO frontend, as described in Section 2.1.1, as laser source for two fiber main amplifiers in the two arms of a Mach-Zehnder interferometer. Here a variable beam splitter, as described tested in Section 3.4, will be used to compensate for small deviations in the laser power of the two single beams. The lithium niobate EOM crystals used in Section 3.2 will by substitute by rubidium titanyl phosphate (RTP) crystals, as used in GEO600 and aLIGO [91], to allow for a higher seed power to the fiber laser amplifier. The combined beam will be pre-stabilized and characterized very similar to the solid-state laser amplifier system presented in Section 3.2.
The usage of a laser source amplified by solid-state amplifiers allows to operate without the fiber pre-amplifiers which could be a benefit for the systems stability and reliability. Additionally, the system will contain several safety loops, including a fast shutdown of the amplifier laser diodes, which will protect the fiber laser amplifiers in case of a seed beam power loss. The fiber laser amplifier and interface modules for this system are very similar to the ones used for the shown experiment and contain sensors for laser powers and temperatures at several positions. If a higher loop gain should become necessary, the anyway needed EOM could be used as a fast phase actuator in one of the interferometer arms.
In this experimental configuration, it will be possible to verify that the fiber laser amplifier based CBC system can be stabilized as well as a solid-state laser amplified system. In addition, the high frequency RPN and frequency noise can be further investigated to verify the predictions made on a possible coupling of the differential phase noise in the solid-state laser amplifier CBC experiment, presented in Figure 3.25. Especially interesting is if the differential phase noise couples to frequency noise in the combined beam at RF frequencies. For a full characterization of the frequency stabilized beam, it could also be of interest to install a second frequency reference.
Even higher laser powers can, in the next steps, be reached, for example, by using specialty fiber laser amplifiers that have shown power levels at and above $350\,\mathrm{W}$ [64, 66], in similar CBC experiments. Another option is to combine more than two laser beams like it is shown in a proof-of-principle experiment in Section 4.1.

3.4. Coherent beam combination of two independent lasers with different power

CBC layouts based on a $50/50$ beam splitter as combining element are strongly dependent on similar laser powers of the to-be-combined laser beams. Whenever the laser beams that should be combined do not have a similar laser power, a perfect summation of the input powers in the combined beam is not possible in this layout. The filled aperture coherent combination of two laser beams with independent seed source could be beneficial in comparison to the combination in a Mach-Zehnder configuration, as the laser noise of the two beams is mostly uncorrelated and thus a reduction in the laser noise by the coherent combination could be possible. A proof-of-principle CBC experiment with two independent laser sources of the same laser power was presented in [76].
A laser system like this would be still operational if problems in one of the combined systems appear. The available laser power would be reduced in that case but the following experiments like a GWD could continue their operation. Additionally, a layout with independent seed lasers could be beneficial for the combined beam's noise behaviour as most of the laser noise would not be correlated. A downside could be an increased system complexity, as not only the differential phase but also the differential frequency between the seed beams need to be stabilized.
In the scope of this thesis, a proof-of-principle CBC experiment with two independent seed sources of different beam power is performed. The focus of this experiment is on the optimal combination of the two laser beams with different power via a variable beam splitter.
The experimental layout and the CBC control loop of this proof-of-principle experiment are presented in Section 3.4.1. A summary of the first results and a prospect for future research in this direction is given in Section 3.4.2.

3.4.1. Optical layout and CBC control loop

A basic schematic layout of the optical components and the phase lock control loop of the CBC experiment is shown in Figure 3.38. The upper beam in the schematic is

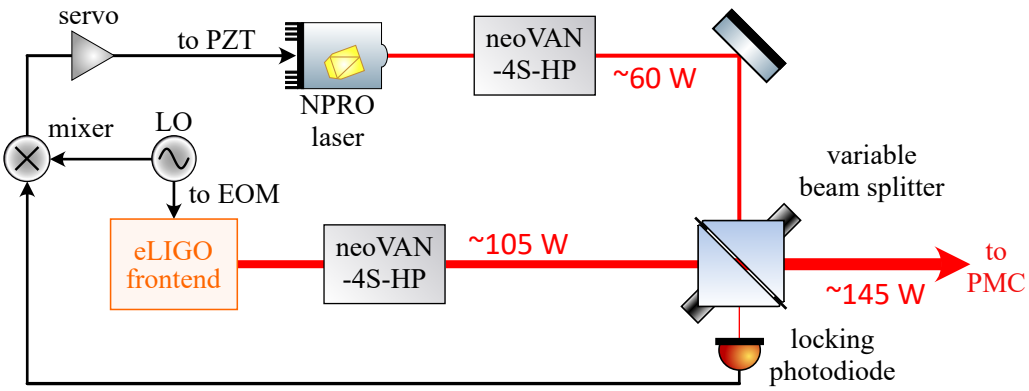

Figure 3.38.: CBC of two independent laser systems. A $105\,\mathrm{W}$ and a $60\,\mathrm{W}$ laser beam are combined on a variable beam splitter via a phase lock feedback control loop. A combined power of $145\,\mathrm{W}$ could be demonstrated.

generated by a 2 W NPRO laser at a wavelength of 1064 nm whose output beam is amplified with a neoVAN-4S-HP amplifier described in Section 3.1.1. The power is amplified to approximately 60 W. An eLIGO frontend, as described in Section 2.1.1, is used to generate the lower beam, which is then also amplified by a neoVAN-4S-HP amplifier. This is the first stage of the sequential amplifier layout described in Section 3.1.1 and delivers an output power of approximately 105 W.
Both beams are sent to a variable beam splitter and the reference system's PMC (see Section 2.1.2) is used as alignment and mode matching reference for both beams.
The basic mechanism of the variable beam splitter was transferred from [93]. The functionality of the beam splitter is based on the frustrated total internal reflection [94, 95] and was first described in [76]. It consists of two prisms with a fixed distance at their corners. The prisms can be bent towards each other with a micrometer screw from one side or a PZT from the other one. Thereby it is actuated on the distance between the prisms in their central area. If the distance between the prisms is bigger than the laser wavelength, a laser beam that is sent to one input of the beam splitter gets total reflected under 90° and an evanescent field exists outside the reflecting surface of the first prism. The field amplitude of the evanescent field decreases with increasing distance from the prism surface. Suppose the distance between the prisms is reduced, the evanescent field couples to the second prism. In that case, a part of the light gets transmitted by the beam splitter. With this scheme almost all laser power of the incident laser beam can get transmitted or reflected by the beam splitter, dependent in the chosen distance between the prisms. In this layout two BK7 prisms are used. As they deform the spatial beam at high laser powers, a next generation of this beam splitter with fused silica prisms is already constructed.
A bright combination port with maximal laser power can only be reached if the dark port does not contain any light. The CBC on a beam splitter with amplitude transmission coefficient and reflection coefficients ρ and τ, and input fields a and a, as well as a bright and dark port output c and d, respectively, is depicted in Figure 3.39. For no light on the dark port, $\rho \cdot a = \tau \cdot b$ must apply. Therewith, the needed ratio between amplitude reflection and transmission coefficient is:

$$\frac{\rho}{\tau} = \frac{a}{b}. \tag{3.10}$$

The power in the input beams is calculated by $P_\mathrm{a} = |a|^2$ and $P_\mathrm{b} = |b|^2$. With this, the relation between the ratio of amplitude reflection $R = \rho^2$ and transmission $T = \tau^2$ of the beam splitter and

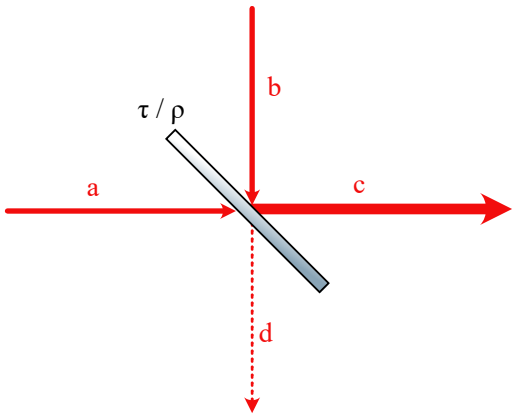

Figure 3.39.: CBC on a beam splitter with amplitude transmission and reflection coefficients τ and ρ. The two input fields a and b are combined to a dark and a bright output field, d and c.

the input powers is written as:

$$\frac{R}{T} = \frac{P_\mathrm{a}}{P_\mathrm{b}}. \tag{3.11}$$

Hence, for two beams with unequal beam power an optimal coherent combination with maximal combination efficiency, defined by the combined power divided by the total available power, can only be reached if the transmissivity and reflectivity of the combining beam splitter is matched to the input powers.
In the presented layout, it is possible to adjust the beam splitter ratio while coherently combining the two seed beams. An optimal combination efficiency is reached by adjusting the beam splitter ratio in order to maximize the combined beam's laser power.
For a successful coherent combination, the frequencies and phases of the two beams have to be matched to each other. The frequency difference between the two beams is adjusted roughly via the temperature control of the upper NPRO laser. Finally, the frequency and phase of the upper beam are stabilized to that of the lower beam with a feedback control loop similar to as described in Section 3.2.2. One advantage in comparison to a system with a single seed laser source, is that the phase sidebands can be imprinted in a low power beam path. Here the frontend's EOM already imprints $35.5\,\mathrm{MHz}$ sidebands for the PMC control loop on the beam which are then also used for the CBC. A photodiode in the dark port is used as sensor. The photodiode's electronic signal is demodulated with the sideband frequency coming from a LO at the mixer, which is directly followed by a low-pass suppress residual signals at the modulation frequency, and is not shown in Figure 3.38 for simplicity. The resulting error signal is fed back to the upper NPRO laser's phase and frequency actuator (PZT) via analog filters and amplifiers which are here summarized as servo.

3.4.2. Experimental results and outlook

The maximal reached output power in this layout is $145\,\mathrm{W}$, which corresponds to a combination efficiency of about $90\,\%$. Losses in the combining efficiency are most likely due to thermal effects in the BK7 prisms of the variable beam splitter as well as alignment and mode mismatches between the two single beams.
By varying the beam splitter ratio, an increase and decrease of the dark and bright port laser powers, respectively, can be observed. Hence, the main goal for this experiment to demonstrate that a variable beam splitter can be used to compensate for different power levels in the combined laser beams, is reached. First noise measurements show that the combined beam's frequency noise is not increased due to the combination process. The relative power noise of the combined beam is increased in comparison to a single beam, which most probably is due to an insufficient CBC feedback control loop.
Future research in this direction could concentrate on optimizing the CBC phase lock loop between two independent laser beams. Thereby, the positive effect on the laser noise due to the mostly uncorrelated noise of the two seed beams could be verified. Additionally, a variable beam splitter with fused silica prisms can be used to avoid the coupling of thermal effects in the prisms to the spatial beam profile of the combined beam. Furthermore, it could be useful to integrate this kind of beam splitter also in experiments with a single seed laser source to compensate

for intended or unintended mismatches in the laser powers of the to-be-combined beams, as it is planned for a future CBC experiment based on fiber amplifiers, described in Section 3.3.5.

4. Novel technologies for gravitational wave detectors

As described in Section 1.2, future gravitational wave detectors (GWDs), like the high frequency part of the Einstein Telescope (ET) [20], require continuous wave laser systems at a wavelength of $1064\,\mathrm{nm}$, which have an excellent beam profile and low laser noise in the $700\,\mathrm{W}$ regime. Currently available solid-state and fiber laser amplifiers, that operate long-term stable and deliver laser beams within the GWD laser system requirements, have maximal laser powers in the $200\,\mathrm{W}$ regime (see Section 3.1 and [55, 59, 60]). Therefore, options to increase the laser power above the $400\,\mathrm{W}$ level, available by coherently combining two high power laser beams, as demonstrated in Section 3.3, need to be investigated.
The insertion of the generated high power laser beams from the laser table into the GWD main vacuum environment is especially challenging. Current GWDs like the two aLIGOs use transparent viewports to insert the PSL laser beam in the interferometer main vacuum systems, and are therefore vulnerable for the coupling of ground movements or air fluctuations to the relative pointing of the laser beam. In addition viewports can produce stray light or thermal effects scaling with the increasing injected laser power that should be used in future detectors.
This chapter is dedicated to two novel technologies that can be used for the generation of high power laser systems and the transportation of the produced laser beam. The CBC scheme was introduced in Chapter 1 and three laser systems based on the coherent combination of two laser beams is presented in Chapter 3. A new possible technology for the coherent combination of more than two laser beams is presented in Section 4.1 of this chapter. Instead of a beam splitter, here an optical bow-tie resonator is used to coherently combine three laser beams in a proof-of-principle experiment.
The question of how to transport high power laser beams from the laser table into the main vacuum system of a GWD is addressed in Section 4.2 of this chapter. Therefore, a hollow core fiber is tested with a laser beam of up to $80\,\mathrm{W}$ and characterized regarding the power throughput and the noise performance of the transmitted laser beam.

4.1. Coherent combination of multiple beams on a resonator

A logical next step in the coherent beam combination (CBC) research is to combine more than two laser beams to increase the generated laser power. This could, for example, be realized with cascaded beam splitters that have reflection to transmission ratios, which are fitted to the beam powers as described in Section 3.4.
In this section, a novel CBC technique that involves a four mirror bow-tie resonator as combining element is presented in a proof-of-principle experiment. This experiment is performed in cooperation with the University of Adelaide, Australia and is installed at the Albert Einstein Institute Hanover. In Figure 4.1 and Figure 4.2 the optical layout and the phase lock feedback control loops are explained, respectively. Afterward, the initial experimental results are presented in Section 4.1.3. Finally, a conclusion on the experiment, a scientific discussion of the results, and an outlook on future research are presented in Section 4.1.4.

4.1.1. Optical Layout

Figure 4.1 shows a simplified schematic of the three beam coherent beam combination (CBC) optical components. All three laser beams origin from an engineering prototype of the eLIGO frontend which is presented in Section 2.1.1. An output

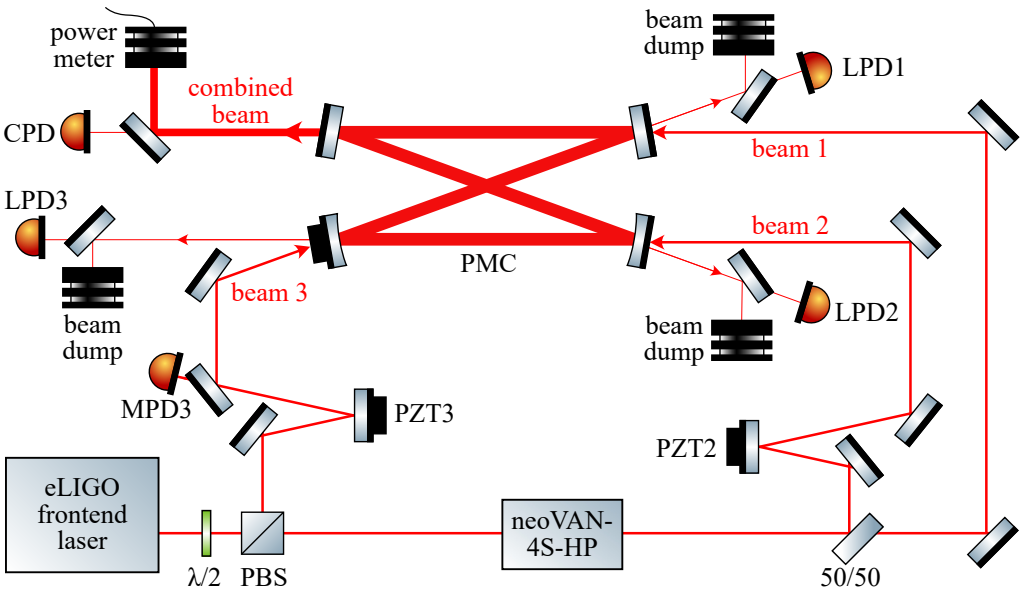

Figure 4.1.: Simplified optical layout of the PMC CBC experiment. The three single beams origin from the same laser source, and are injected to different ports of the PMC. A photodiode and a water-cooled power meter are used to characterize the combined beam.

power of 24 W is generated by the frontend laser and split in one 21 W and one 3 W beam at a polarizing beam splitter (PBS). The high power laser beam is sent to the combining resonator via a PZT driven mirror (PZT3) and is called beam 3 in the following.
The low power beam is guided to a neoVAN-4S-HP solid-state laser amplifier (see Section 3.1.1). The amplified laser beam with a power level of about 60 W is

split up in two beams by a $50/50$ beam splitter. The resulting beams are called beam 1 and beam 2. Beam 1 is guided to the resonator directly and beam 2 via a piezo-electric element (PZT) supported mirror (PZT2). In all three beams paths are power attenuation stages installed, which are not shown in the schematic.
The bow-tie combining resonator is very similar to the aLIGO pre-mode-cleaner (PMC) [38, 43] presented in Section 2.1.2 and will therefore be called PMC in the following. The aluminum spacer has the same mechanical layout as the aLIGO PMC but the mirrors are clamped instead of glued to enable a fast exchange if necessary. For the same reason, the PMC is not located in an enclosure in this proof-of-principle experiment.
The four PMC mirrors are optimized for three input laser beams with the same beam power. Hence, three identical input mirrors are chosen for the cavity. With this parameter given, all four mirror reflectivities are derived with respect to the desired PMC finesse and impedance matching, which are set similarly as for the aLIGO PMC. With that, the three incoupling mirrors have design reflectivities of $99.16\,\%$. The beam 1 input mirror is flat and the beam 2 and beam 3 input mirrors are curved with a radius of curvature of $-3\,\mathrm{m}$ as for the aLIGO PMC. The beam 3 input mirror is clamped to the PMC on a PZT, that allows for an actuation of the PMC length. The flat output mirror has a design reflectivity of $97.5\,\%$. The resonator's Finesse is calculated to be 124 which is very close to the 129 for the aLIGO PMC [38, 43].
The part of each of the three beams that is reflected by the PMC is guided to a photodiode (PD1, PD2 and PD3) via partly transmissive pick-off mirrors. The residual power in this beam paths is dumped on water-cooled beam dumps. The combined output beam's power is measured at a water-cooled thermal power sensor in reflection of a partly transmissive pick-off mirror. A combination photodiode (CPD) senses the beam in transmission of this pick-off mirror.
One advantage of using a resonator as combining element is that no additional alignment reference is needed. All three beams are aligned and mode matched to the PMC, which also guarantees an excellent spatial superimposition between the three beams.

4.1.2. The CBC phase lock control loops

The control schemes needed to coherently combine the three laser beams are depicted in Figure 4.2. As a first step, the laser frequency is locked to the TEM_{00} eigenmode of the PMC in a Pound-Drever-Hall locking scheme [44] as depicted in Figure 4.2a. Phase sidebands at a frequency of $35.5\,\mathrm{MHz}$ are provided by a LO and imprinted on the laser beam with an electro-optical modulator (EOM) in the frontend laser. PD1 senses the PMC reflection of beam 1 and the corresponding signal is demodulated at the sideband frequency with a mixer to produce the Pound-Drever-Hall error signal. All used mixers are followed by low-pass filters to suppress residual oscillations at the sideband frequency. For simplicity, those filters are not depicted here. The mixer signal is filtered and amplified with analog electronics (servo). The resulting control signal is fed back to a PZT attached to the NPRO crystal that actuates on the laser frequency.
The frequency lock of beam 1 also applies for beam 2 and beam 3 as all three beams origin from the same laser source. Therefore, beam 2 and beam 3 are resonant in the PMC as well if beam 1 is locked to it. A constructive interference of

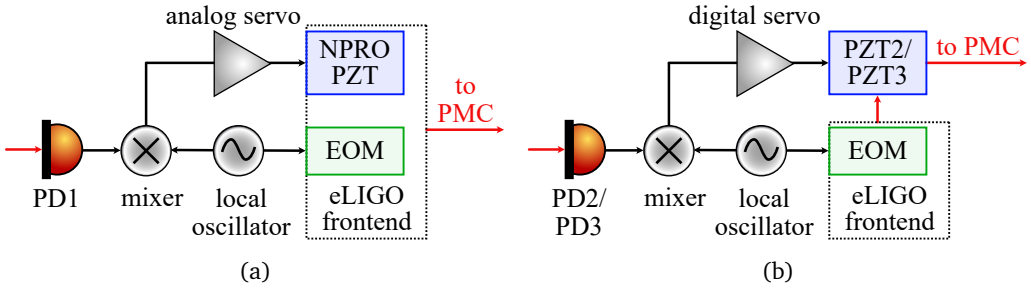

Figure 4.2.: Simplified schematics of the PMC CBC control loops. (a) Beam 1 is frequency stabilized to a PMC resonance via the Pound-Drever-Hall scheme. A photodiode is used as sensor and the PZT that is attached to the NPRO crystal as actuator. (b) Beam 2 and 3 are phase locked to the circulating field inside the PMC via photodiodes as sensors and PZT driven mirrors as actuators.

beam 2 and beam 3 with the circulating PMC field is reached with two phase lock control loops as depicted in Figure 4.2b. The used locking mechanism is very similar to as presented for the solid-state laser amplifier coherent beam combination in Figure 3.13. The $35.5\,\mathrm{MHz}$ phase sidebands imprinted by the frontend's EOM are used for the phase lock loops as well. If the laser frequency is stabilized to the PMC's TEM_{00} eigenmode only light within the PMC linewidth of several MHz is transmitted. Hence, the $35.5\,\mathrm{MHz}$ sidebands are not transmitted by the PMC and the same modulation frequency can be used for all three control loops. The photodiode signals are demodulated with the sideband frequency at analog mixers. The resulting control signals are then send to two digital controllers (Red Pitayas). The controllers filter and amplify the signal and are therefore also labelled as servo. The corresponding control signals are fed back to PZT2 and PZT3 via analog high voltage amplifiers, not depicted here for simplicity. The PZT driven mirrors actuate on the phase of beam 2 and beam 3 in order to produce a combined beam with the maximal power at the combined PMC output port.
The open-loop transfer functions for all three control loops are depicted in Figure 4.3. For beam 1 an unity-gain frequency of $4.5\,\mathrm{kHz}$ with a gain margin of $6.15\,\mathrm{dB}$ and a phase margin of $31.9°$ is reached. The dip at about $15\,\mathrm{kHz}$ is due to a notch filter in the analog electronics. The corresponding phase loss limits the control bandwidth. The used analog electronics are reused from earlier experiments and just slightly adjusted for this experiment. Therefore, it can be reevaluated if this notch is needed or can be replaced in the future.
The open-loop transfer functions for beam 2 and beam 3 shown in Figure 4.3b have a very similar shape. The phase lock control loop for beam 2 has a unity-gain frequency of $187\,\mathrm{Hz}$ with a gain margin of $7.56\,\mathrm{dB}$ and a phase margin of $32.5°$. The unity-gain frequency for beam 3 is at $199\,\mathrm{Hz}$ with a gain margin of $8.39\,\mathrm{dB}$ and a phase margin of $35.6°$. Both loops are limited by a resonance at around $500\,\mathrm{Hz}$. This resonance comes most likely from the PZT driven mirrors that are used as phase actuators in this control loops. The PZT resonance alone would be at a much higher frequency of about $78\,\mathrm{kHz}$ corresponding to the manufacturer. Thus, a coupling in the whole structure of the PZT, the mirror and the adjustable mirror mount can be assumed. The slight difference in the resonance frequencies

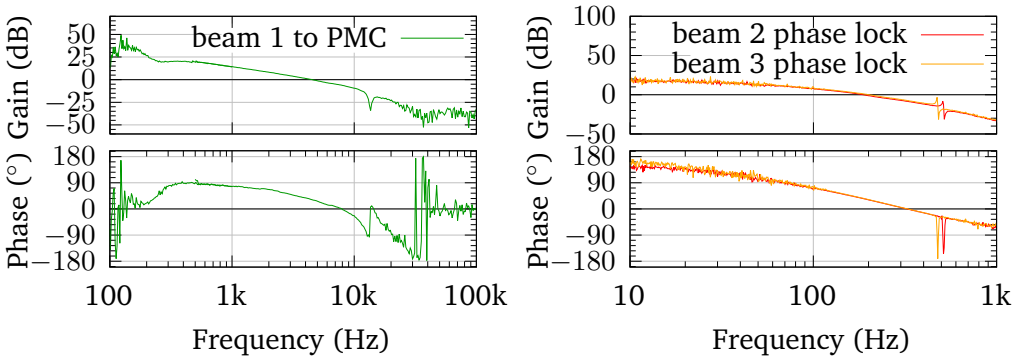

(a) (b)

Figure 4.3.: (a) Open-loop transfer function of the frequency stabilization loop from beam 1 to the PMC length. A unity-gain frequency of $4.5\,\mathrm{kHz}$ is reached with an analog servo. (b) Open-loop transfer functions of the phase lock control loops of beam 2 and beam 3 to beam 1. Unity gain frequencies of $187\,\mathrm{Hz}$ and $199\,\mathrm{Hz}$ are reached for beam 2 and 3, respectively, with digital servos.

for the loop of beam 1 and beam 2 assist this hypothesis, as the two mirror mounts are of the same type but not identical.

4.1.3. Characterization

The presented proof-of-principle experiment is analyzed with respect to the combined laser power and the relative power noise (RPN) of the combined laser beam. Those are the first results in this layout, and a further characterization is planned for the future as it will be described in Section 4.1.4.

Combined laser power

Three laser beams with power levels of $5\,\mathrm{W}$ each are combined in the first step of the presented proof-of-principle experiment. In the described CBC scheme, the frequency of all three beams is stabilized to the PMC TEM_{00} eigenmode. The expected power at the combined output P_{CBC} is calculated by:

$$P_{\mathrm{CBC}} = |\tau_{\mathrm{out}}|^2 P_{\mathrm{circ}} \tag{4.1}$$

with the circulating power P_{circ} and the amplitude coefficient of the transmission of the outcoupling mirror τ_{out}. The circulating field depends on the three input powers P_1, P_2 and P_3 and the transmission and reflection of the four PMC mirrors. More detailed equations as well as the definition of the PMC ports can be found in Appendix B.
As the laser beams injected to the PMC are stabilized to its TEM_{00} eigenmode, all laser power in beam 1, beam 2 and beam 3 that is in other modes is not contributing to the combined output power. Thus, the circulating power in the PMC and with that the maximal combined laser power strongly depends on the HOM content of the three single laser beams in the PMC eigenmode basis.

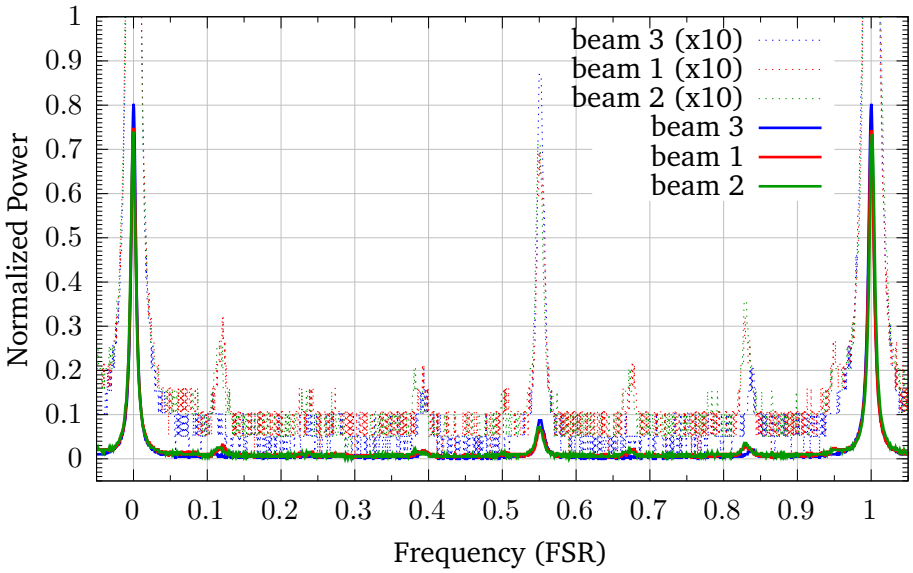

Figure 4.4.: The modescan measurement of all three single beams reveal high HOM contents of about $25\,\%$ for beam 1, $26\,\%$ for beam 2 and $20\,\%$ for beam 3.

For a given PMC length, the HOMs are resonant in the PMC at different frequencies than the TEM_{00} eigenmode. By scanning the laser frequency and measuring the laser power in transmission of the PMC, a modescan measurement is generated for each of the three laser beams individually, while the other two beams are blocked. This measurement is similar to the diagnostic breadboard (DBB) HOM content measurement described in Section 2.2. The corresponding data is captured with an oscilloscope and presented in Figure 4.4. The x-axis is normalized to one free spectral range (FSR) of the PMC, which corresponds to a laser frequency change of $149\,\mathrm{MHz}$. The peaks at $0\,\mathrm{FSR}$ and $1\,\mathrm{FSR}$ represent the TEM_{00} mode, and all other peaks are the HOMs. The y-axis displays the power in the different modes normalized to the sum of all mode peaks per measurement.
The solid curves represent the actual measurements and the dotted lines a zoom-in on the HOMs for each beam by a factor of 10. With this measurement a HOM content of about $25\,\%$ for beam 1, $26\,\%$ for beam 2, and $20\,\%$ for beam 3 are derived. All three beams have laser power in the same HOMs, which is expected as thy from the same laser source and the Gouy phase of the cavity is independent of the used input port. The total HOM content is probably directly related to the frontend laser, which could not be operated at the optimal pump light parameters due to degrading pump diodes. The neoVAN-4S-HP laser amplifier most likely increases the HOM content further, as misalignment and mode matching couples stronger to deformations of the beam profile if the seed beam is not in a pure Gaussian mode. This explains the increased HOM content of beam 1 and beam 2 in comparison to beam 3, which comes directly from the frontend. Additionally, a mismatch in the alignment and mode matching of the three beams with respect to the PMC eigenmode contributes to the modescan measurements.
The HOM content of the three injected laser beams corresponds to total HOM powers of $P_1 = 3.75\,\mathrm{W}$ for beam 1, $P_2 = 3.7\,\mathrm{W}$ for beam 2 and $P_3 = 4\,\mathrm{W}$ for beam 3, each with estimated readout errors of $\pm 1.5\,\%$. The expected combined power cal-

culated with Equation (4.1) is $P_{\mathrm{CBC}} = 11.45\,\mathrm{W} \pm 0.23\,\mathrm{W}$. The measured combined power in this experiment is $11.3\,\mathrm{W}$, which is within the expected value's error range. The main power of the combined beam is measured with a water-cooled thermal power meter. The laser power that is transmitted by the partly transmissive pick-off mirror at the combined output of the PMC is added to reach the final combined power.

Relative power noise

The RPN of the combined beam is compared to the RPN of beam 1 behind the PMC while it is locked to the PMC and beam 2 and beam 3 are blocked. Both measurements are captured with a Stanford Research Systems SR785 FFT analyzer via the CPD at the PMC's output port and are presented as amplitude spectral density (ASD) over the Fourier frequency in Figure 4.5. Up to around $25\,\mathrm{Hz}$ and above

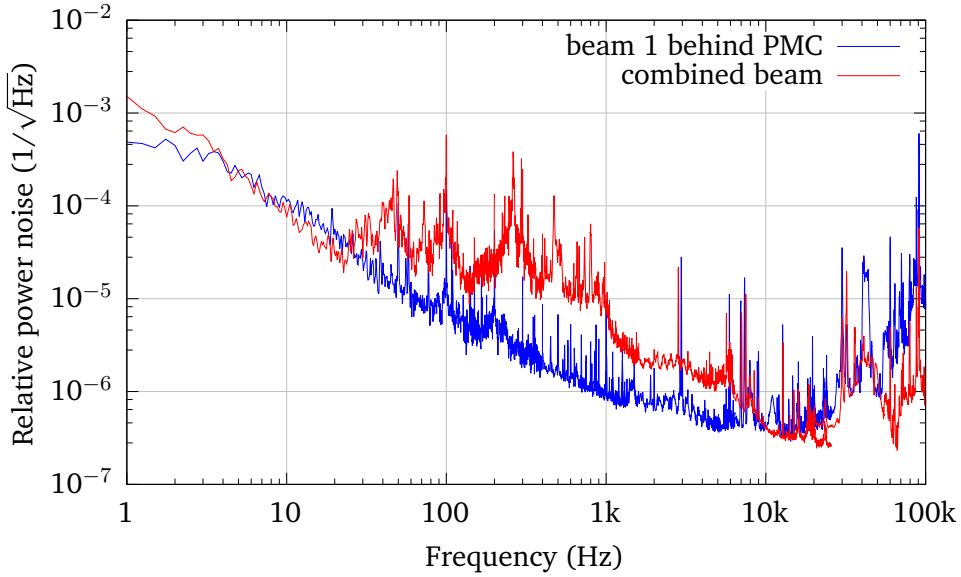

Figure 4.5.: RPN measurements for beam 1 behind the PMC and the combined beam. The increased noise of the combined beam between $20\,\mathrm{Hz}$ and $10\,\mathrm{kHz}$ can most probably explained by a coupling of insufficient suppressed differential phase noise or an increased pointing noise in beam 2 and 3.

$10\,\mathrm{kHz}$ the combined beam's RPN is similar or below the RPN of beam 1. A decrease in the combined beam's RPN could be possible due to the incoherent summation of partly uncorrelated RPN in the three laser beams similar to as described in Section 3.2.3.
Between $20\,\mathrm{Hz}$ and $10\,\mathrm{kHz}$ the RPN of the combined beam is increased in comparison to beam 1. Here the differential phase noise between the three beams could couple to the combined beam's RPN. The unity-gain frequencies for the phase lock control loops of beam 2 and 3 to beam 1 are only at around $200\,\mathrm{Hz}$. Thus, the suppression of the differential phase noise between the three beams is most probably not sufficient. The differential phase noise between the beams could be increased due to for example vibrations in the beam paths, acoustic noise or stray light.
Another reason for the increased RPN could be an increased pointing noise in

beam 2 and beam 3, driven by the phase actuation at the PZT driven mirrors, which would couple to power noise at PMC as described in Section 1.2.2.
Also the small increase of the combined beam's RPN at frequencies below $4\,\mathrm{Hz}$ can be due to a coupling from the pointing noise of the three beams.

4.1.4. Conclusion and outlook

The first results of a proof-of-principle experiment on the CBC of three laser beams with a bow-tie PMC as combining element are presented in this section. Several advantages are expected for the combination of three laser beams on a resonator in comparison to cascaded beam splitters. A practical advantage is that the needed phase sidebands for all three control loops can be imprinted on the low power beam before the common and individual amplification, as all three beams are stabilized to he PMC independently. Therefore, only one low power EOM, and one sideband frequency is needed.
In a GWD pre-stabilized laser system (PSL) layout it could be possible to use a PMC for the combination and as first component of the PSL (see Chapter 2). This configuration could simplify the experimental layout and just one phase sideband frequency instead of two as in Section 3.2 would be needed. Furthermore, the combined laser beam can be expected to have a very pure Gaussian beam profile defined by the resonator eigenmode, and the combined beam's power and frequency noise is filtered between the resonator's pole frequency and FSR (see Section 1.2) in comparison to the single beams.
The PMC is designed and assembled for three laser beams with similar power levels. The three combined laser beams have a laser power of $5\,\mathrm{W}$. The high HOM contents of the three laser beams between $20-26\,\%$ in comparison to the PMC TEM_{00} eigenmode result in a reduction of the injected power for each beam. The combined laser power of $11.3\,\mathrm{W}$ generated in this experiment is in good agreement with the expected $11.45\,\mathrm{W}$.
The next steps in this experiment require a further investigation of the beam quality of the three single beams. The general high HOM content of all single beams can most probably traced back to the frontend laser amplifier's pump diodes, which will be replaced. A DBB on the laser table can be used to characterize the input beams and the combined beam's HOM content further as described in Section 2.2. Thereby, it can be verified that the combined beam has much lower HOM content than the single beams, due to the PMC's HOM suppression. Additionally the available power in all three beams can be increased to about $20-30\,\mathrm{W}$ in the existing layout.
The RPN of the combined beam shows only minor degradation in comparison to a single beam. An increased noise of the combined beam between $20\,\mathrm{Hz}$ and $10\,\mathrm{kHz}$ could be explained by a coupling of insufficient suppressed differential phase noise or an increased pointing noise in beam 2 and beam 3. The phase lock control loops for beam 2 and beam 3 to beam 1 are limited by resonances of the PZT driven mirrors at around $500\,\mathrm{Hz}$. An alternative mounting structure for the PZT driven mirrors can be investigated in the future to suppress the resonance and increase the control loop bandwidths. With the higher possible phase noise suppression a further investigation of the assumed phase noise to RPN coupling would be enabled.
An available DBB on the laser table can, in the next steps of this experiment, be

used to characterize the HOM content, frequency noise and relative pointing noise of the single and combined laser beam as described in Section 2.2.
In future experiments, the developed coherent combination scheme could be used to combine three laser beams amplified by fiber laser amplifiers with power levels in the $200-365\,\mathrm{W}$ regime [59, 64, 66]. Thereby it is a very promising scheme to generate the high laser powers required for future GWDs like ET [20]. A coherent combined laser system based on the presented technique could be the basis for a GWD PSL with only one PMC as combining element and filter for HOM's, relative pointing noise and RF laser noise in one.

4.2. Hollow core fiber for high laser power transportation

An alternative to the currently used viewports to transport the GWD PSL's high power laser beam to the interferometer's main vacuum system could be hollow-core fibers. By using a fiber for the transportation, ground movements or air fluctuations in the laser room can be decoupled from the pointing noise of the laser beam in the vacuum system. The problem of thermal beam deformations and scattering that could appear if a viewport transmits the high-power laser beam could be reduced as well due to the air guiding in the hollow core fiber.
While the usability of fibers with glass cores is limited by stimulated Brillouin scattering if high powers are transported in them over long distances, the structure of a hollow core fiber should overcome this boundary.
In this section, a $3\,\mathrm{m}$ long hollow core fiber is used to transport a laser power of up to $80\,\mathrm{W}$ in a proof-of-principle experiment. First, the experimental layout is described briefly in Figure 4.7. Then the results are described and characterized in Section 4.2.2. Finally, the results are summarized, classified, and an outlook is given in Section 4.2.3.

4.2.1. Experimental layout

The hollow core fiber that is used in this experiment is provided by collaborators from the university of Limoges, France and its parameters are oriented very close on a standard fiber from GLOphotonics (Type: PMC-C-Yb-7C). The fiber is optimized for low losses for an injected laser beam with a wavelength of $1064\,\mathrm{nm}$. Figure 4.6 shows a photography of the cross-section of the fiber, captured with a Vytran glass processor (GPX3400).
The fiber has a core diameter of $60\,\mu\mathrm{m}$ and an outer diameter of $320\,\mu\mathrm{m}$. The fiber length is about $2.8\,\mathrm{m}$, and the fiber losses are optimized to be $<50\,\mathrm{dB/km}$ according to the manufacturer.
The core of step-index fibers, as used in Section 3.3, has an index of refraction that is higher than that of the cladding. Thereby the light is total internal reflected on the cladding and guided in the core [96]. This operating principle is not possible in a hollow core fiber as it's core is filled with air, which has a lower index of reflection than the surrounding glass. Therefor, the hollow core of the fiber is surrounded by smaller air holes as cladding structure. The size and distance of the smaller holes form a photonic bandgap structure for the light injected to the fiber and thereby guarantee that the light is guided in the core [97].

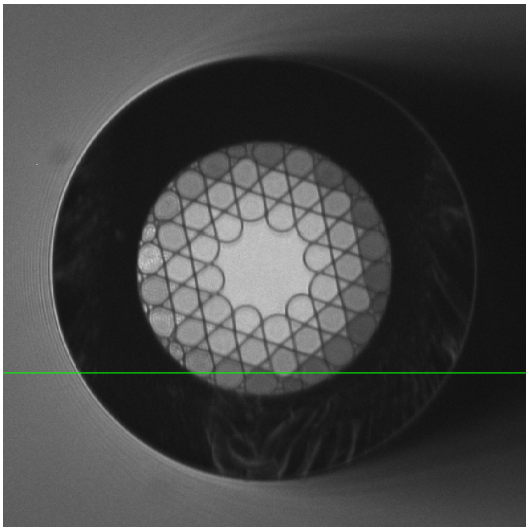

Figure 4.6.: Cross-section of the hollow core fiber. The core is surrounded by smaller air holes, which generate a photonic bandgap structure.

Figure 4.7 shows a simplified schematic of the experimental layout that is used to characterize the hollow core fiber. The PMC transmission of the reference system's

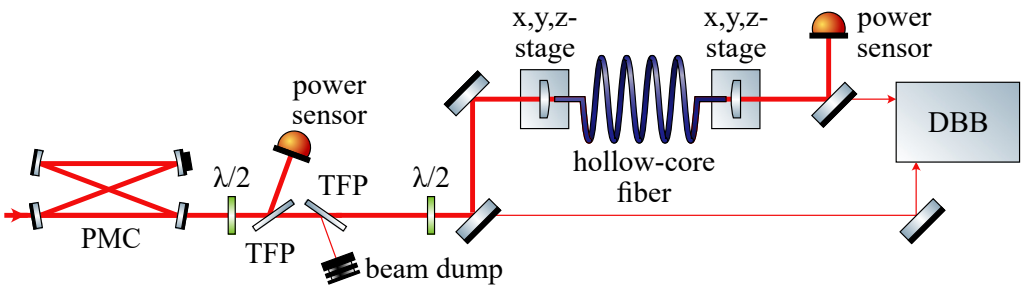

Figure 4.7.: Simplified schematic of the characterization layout for the hollow core fiber. The seed beam comes from the PMC and can be attenuated on it's way to the fiber. The seed beam and the beam transmitted by the fiber are characterized with a DBB.

frontend beam (see Chapter 2), amplified with a neoVAN-4S-HP laser amplifier, is coupled to the hollow core fiber. The seed beam is beam 1 of the coherent beam combination experiment described in Section 3.2. The PMC serves as an ideal starting point to characterize new components, like here the hollow core fiber, as it provides a very clean beam profile and optional power and frequency stabilization. A combination of a half-wave plate ($\lambda/2$) and two thin film polarizers (TFPs) behind the PMC is used to attenuate on the laser power. By rotating the half-wave plate the angle of the already linear polarized beam is changed. The TFP only transmit p-polarization in this configuration and thereby the power sent to the fiber can be attenuated. The second TFP performs a further cleaning of the polarization. With this configuration, not only can the power be attenuated, but it is also assured that the laser beam that is sent to the fiber has a very clean linear polarization. The polarization axis can be changed with respect to the fiber with an additional half-wave plate.
An aspheric incoupling lens is installed in a x-,y-,z-adjustable stage. Thereby it can be optimally adjusted with respect to the incoupling fiber end. The incoupling site of the fiber is taped to a v-groove that is fixed to the rigid part of the x-,y-,z-stage. The outcoupling site of the fiber is assembled similar to the incoupling site, with the only difference, that the fiber is fixed to the groove with soft magnets. The light that is transmitted by the fiber is attenuated and then send into a DBB, described in Section 2.2.
A small fraction from the seed beam that is injected into the fiber is guided to the DBB as well.

4.2.2. Hollow core fiber performance

In this layout laser powers between less than a $1\,\mathrm{W}$ and about $85\,\mathrm{W}$ are sent to the hollow core fiber. An almost constant transmission between $94-96\,\%$ is reached at all input power levels.
An important parameter for the transmission ratio is the fiber bending radius. GLOphotonics specifies a $3\,\mathrm{dB}$ loss for a bending ratio of $5\,\mathrm{cm}$ for their very similar fiber type. The suggested strong dependence between the bending radius and the fiber losses is verified by changing the radius while coupling light to the fiber. An increasing transmitted power is measured while increasing the bending radius. For a bending radius of about $26\,\mathrm{cm}$ and higher, this coupling can no longer be mea-

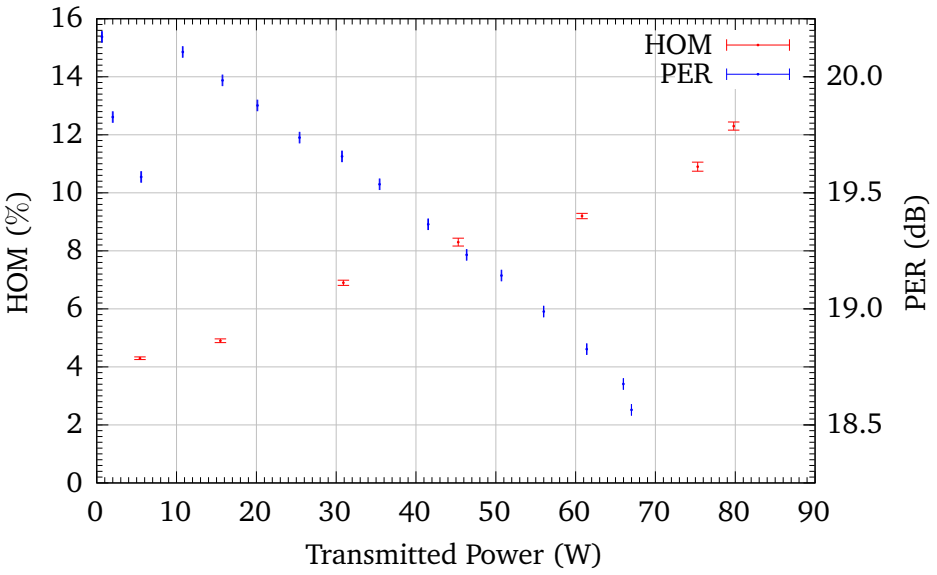

Figure 4.8.: HOM content and PER of the beam transmitted by the hollow core fiber relative to the transmitted laser power. The HOM content increases from about $4.3-12.3\,\%$. The PER decreases slightly from $20.2-18.6\,\mathrm{dB}$ from increasing transmitted powers.

sured. For that reason a bending radius of about $25\,\mathrm{cm}$ is used for all presented measurements.
The HOM content of the seed beam is $<1.2\,\%$, for the shown measurements. Figure 4.8 shows the HOM content and polarization extinction ratio (PER) of the beam transmitted by the hollow core fiber. The increase in the HOM content of the transmitted beam from $4.3\,\%$ at $5.41\,\mathrm{W}$ to $12.3\,\%$ at $79.8\,\mathrm{W}$ can have different origin. One reason for the increased HOM content with increasing laser power can be that the mode matching and alignment to the fiber slightly changes due to thermal lenses before the fiber. This could result in a coupling to higher order fiber modes. The alignment and mode matching is optimized for low seed laser powers and due to the danger of burning the fiber not redone for the high power levels.
Another option is that the higher order modes are exited due to an increased thermal load at the fiber itself that results in a changed fiber eigenmode. Also, thermal effects in the components behind the fiber could change the beam profile.
The general increase of the HOM content of the beam transmitted by the fiber compared to the seed beam is at least partly due to the difference between the fiber eigenmode and the TEM_{00} eigenmode of the DBB cavity, that occurs due to the arrangement of the air holes. Imperfect alignment and mode matching to the fiber is observed to increase the HOM content behind the fiber further.
To measure the PER in transmission of the fiber, a half-wave plate in transmission of the fiber rotates the polarization of the light with respect to a TFP, which only transmits linear polarized light for a certain polarization angle. The polarization extinction ratio (PER) is determined by calculating the ratio between the total laser power transmitted by the fiber and the power of the linear polarized light in transmission of the fiber in dB. The measured PER decreases from $20.2\,\mathrm{dB}$ to about $18.6\,\mathrm{dB}$ with increasing transmitted laser power. The decrease could be a result of thermal effects in the fiber.

Relative power noise

The RPN of the laser beam in transmission of the fiber is measured with the DBB (see Section 2.2) in $15\,\mathrm{W}$ steps, starting at $5\,\mathrm{W}$ and ending at $80\,\mathrm{W}$. All measurements together with a RPN measurement of the seed beam, captured with the same DBB, are presented as ASD over the Fourier frequency in Figure 4.9. Relative pointing noise of the seed beam relative to the incoupling fiber tip position can couple to the RPN in transmission of the fiber, as it induces changes in the alignment to the fiber. The same changes occur if the incoupling fiber end moves with respect to the laser beam. An increase of the RPN of the beams transmitted by the fiber in comparison to the seed's RPN at measurement frequencies below $20\,\mathrm{Hz}$ could be an indication for such a relative movement between the laser beam and the fiber tip. Differences between the transmitted measurements at that frequency range could appear due to small differences in the initial alignment to the fiber, which would influence the coupling from relative pointing to relative power noise. It has to be pointed out that, especially at low frequencies, also environmental disturbances like stray light or acoustic noise couple in the relative power noise measurements, but all these effects have to be considered as very small in the presented measurements.

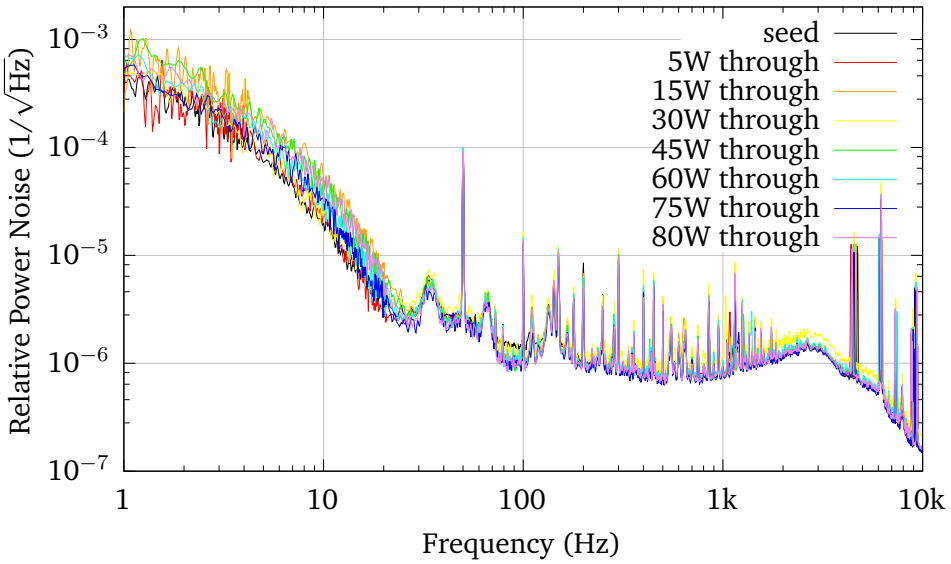

Figure 4.9.: The RPN measurements of the seed beam and the beam transmitted by the fiber at different transmitted powers are at a very similar level.

At all other frequencies the curves look very similar, which fits the expectation, that the fiber does not add RPN to its seed beam. Small deviations especially in the $30\,\mathrm{W}$ curve could be due to a small calibration disagreement in the DBB during the measurement or environmental noise that couples in the measurement.

Frequency noise

The frequency noise of a laser beam is not expected to be influenced if the beam surpasses an optical fiber of a stable length. The DBB frequency noise measurements (see Section 2.2) of the seed beam and the beam transmitted by the fiber at

different power levels are shown as ASD over the Fourier frequency in Figure 4.10. Most of the measurement curves are very similar to each other as well as to the

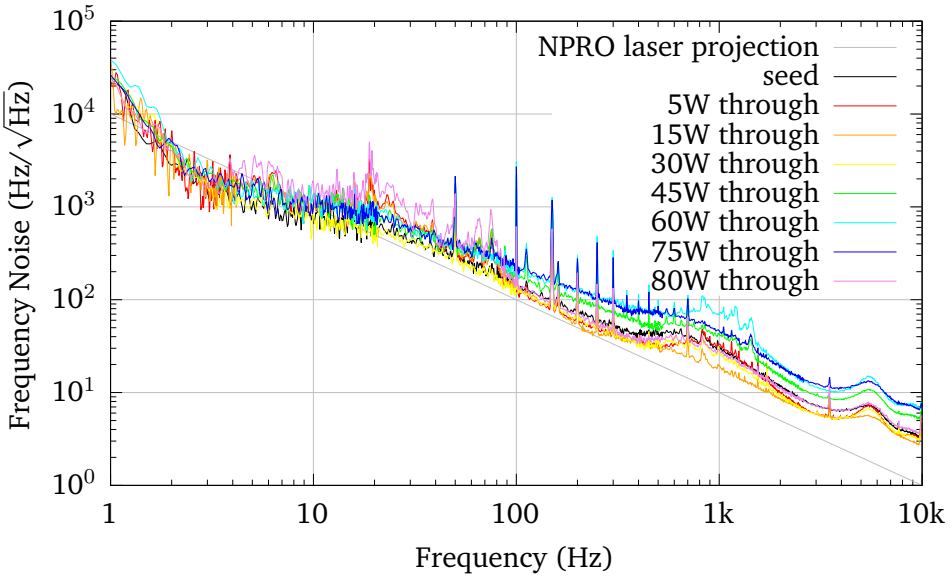

Figure 4.10.: The frequency noise measurements of the seed beam and the beam transmitted by the fiber at different transmitted powers are in general close to each other and the NPRO laser projection. Slight differences at frequencies above 100 Hz can be due to environmental perturbations that couple to the measurement or the fiber.

NPRO laser projection, which serves as a reference line. Deviations around 1 kHz are due to slightly different power levels in the DBB and thereby also slightly different unity-gain frequencies of its frequency control loop.
The measurements at 45 W, 60 W and 75 W show a slightly increased noise above 20 Hz. The reason for could be acoustic perturbations that couple to the fiber or environmental disturbances, that affect the calibration of the DBB measurements.

Relative pointing noise

The relative pointing noise of the seed beam and the beam transmitted by the fiber at different power levels are shown in Figure 4.11. All measurements are captured with the DBB, as described in Section 2.2, and are presented as ASD over the Fourier frequency. For simplicity the curves show the uncorrelated sum of all four degrees of freedom for each of the measurements that are captured with the DBB and thereby represent upper bounds.
The relative pointing noise of a laser beam that is transmitted by a fiber can change due to different mechanisms. A reduction in the pointing noise is possible when the fiber output mounting is more stable than the seed beam position. At frequencies below about 20 Hz this effect might be visible for the measurements from 5 W to 45 W.
At frequencies above 20 Hz the relative pointing noise of the transmitted beams is mostly higher or equal to the seed beams measurement. A split between the curves from 5−30 W and the curves from 45−80 W is visible, where the measurements at higher laser powers have an increased noise. This clear split can origin from a small

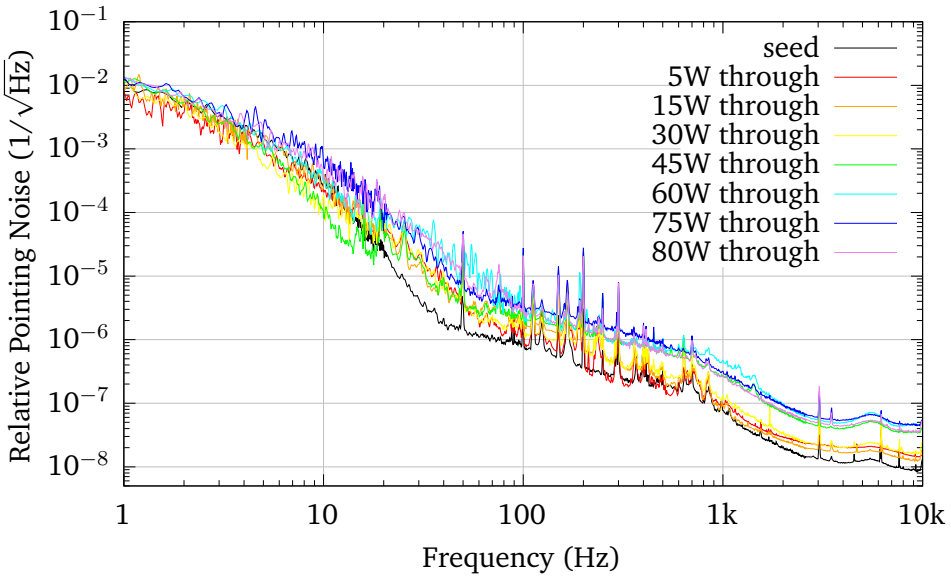

Figure 4.11.: The relative pointing noise measurements of the seed beam and the beam transmitted by the fiber at different transmitted powers is in the same order of magnitude.

unintended change in the out-coupling path of the fiber between the measurements or from environmental influences that appear at different times.
The seed laser follows a different in-coupling path to the DBB which includes less optical components and might therefore also be a reason for differences in the noise curves.

4.2.3. Conclusion and outlook

A proof-of-principle table-top experiment for guiding light powers of up to $80\,\mathrm{W}$ through a hollow core fiber is presented in the section. A hollow core fiber could be a good alternative to the currently used viewports to transport light from the laser table to the GWDs main vacuum system. In comparison to fibers with glass core, no limitation of the transportable laser power and the fiber length due to stimulated Brillouin scattering is expected in hollow core fibers.
A fiber transmission between $94-96\,\%$ could be reached at all input powers and a characterization of the transmitted light with respect to the seed light is performed with a DBB.
Even though the fiber is not polarization maintaining, a PER between $20.4-18.7\,\mathrm{dB}$ could be measured. It decreases to higher laser powers, which could be due to thermal effects in the fiber.
The transmitted beam's HOM content increases with increasing power from $4.3\,\%$ to $12.3\,\%$, which most probably is also due to thermal effects.
The RPN measurements for different power levels are very similar to each other, as expected. Also the frequency noise measurements and the pointing noise measurements are in the same order of magnitude. Small deviations in both noise measurements are most probably due to environmental influences.
All measurements show promising first results. Different tests can be performed in the future to investigate the noise coupling mechanisms of and in this fiber. Ther-

mal effects will be tested, by implementing water cooling at the mounts for the fiber ends as a first step. The general fiber holding mechanism is very basic in this experiments and will be improved in the next version of this experiment. One example to reduce possible disturbances in the hollow fiber core itself, could be to evacuate the fiber core and install small gas tight chambers at the ends. Earlier experiments with other hollow core fibers led to the consideration that small dust particles or water gathered in the hollow core over time and negatively influenced the coupling efficiency [98]. This effect is not seen in the experiments here, but it is not excluded that additional noise could come from the same effect.
In future research the out-coupling fiber end will be inserted to a vacuum tank to investigate possible additional noise couplings in a more realistic scenario.

5. Conclusion

This thesis reports on the development of different laser systems for the generation and an option for the transportation of high power laser radiation at a wavelength of $1064\,\mathrm{nm}$ that can satisfy the stringent and unique requirements of current and future ground-based interferometric gravitational wave detectors (GWDs). As shown in Chapter 1, these detectors need high laser power in the continuous wave regime to overcome shot noise limitations. Laser systems with excellent spatial beam quality and low laser noise are needed to avoid a noise coupling to the GWD output channel, which could decrease the detector's performance.
In view of the needs of current GWDs, the benefits and limitations of a laser system based on the sequential amplification of a laser beam with solid-state laser amplifiers are investigated in Section 3.1. The resulting laser system provided a total laser power of $195\,\mathrm{W}$, sufficient for the needs of current GWDs. The last amplifier's output beam was analyzed regarding its spatial mode profile and laser noise, with free-running as well as stabilized power and frequency of the amplifier's seed laser beam. The system showed free-running noise characteristics comparable to that of current GWD laser systems. Potential limitations were uncovered with a stabilized seed beam and led to suggested improvements on the layout of future laser systems based on these amplifiers. The promising results of this work are published in [55] and built the base for the aLIGO laser system that will be used in the fourth GWD networks observing run (O4) planned to start in the first half of 2023. A first prototype of the O4 system was assembled and tested at the aLIGO Livingston site during a research stay. The prototype's first results, published in [56], confirmed the system's suitability as aLIGO's O4 laser system.
For the next generation GWDs, as, for example ET-HF [20], power levels on the order of $500\,\mathrm{W}$ are foreseen at the input of the interferometer to increase their sensitivity further compared to current generation GWDs. Due to power losses in between the laser source and the interferometer input, for example at mode-cleaners, a laser power of about $700\,\mathrm{W}$ should be provided by the GWD pre-stabilized laser system (PSL). The investigations on solid-state laser amplifiers performed in this thesis and on fiber laser amplifiers, as summarized in Section 1.3.1, showed that the sequential amplification of a single laser beam is currently not sufficient to generate the required power levels.
As alternative, the coherent combination of two laser beams as possible technique for further power scaling is explained in Section 1.3.2 and investigated in Chapter 3 under different aspects in separate laser systems.
The first pre-stabilized laser system (PSL) based on the coherent beam combination (CBC) technique is presented in Section 3.2. Two laser beams originating from the same seed source, each amplified by a solid-state laser amplifier, were coherently combined in a Mach Zehnder interferometer configuration. The resulting laser system was integrated in the aLIGO pre-stabilized reference laser system, which was described in Chapter 2, and characterized in detail regarding the spatial

beam profile and possible noise couplings in the CBC process. The resulting beam had a total power of $100\,\mathrm{W}$ and was successfully power and frequency stabilized with noise performances comparable to current GWD laser systems. No significant noise couplings of the CBC process were measured in most parameters. Only the influence on the combined beam's RF frequency noise was suggested to be further investigated in future experiments. The results suggest that laser systems based on CBC in the shown configuration are suitable for the usage as GWD laser system.
A power scaling of the combined beam can be realized, for example by using sequential solid-state laser amplifiers, like presented before, or fiber laser amplifiers in the to-be-combined laser beams.
A CBC system with fiber laser amplifier chains in the two arms of a Mach-Zehnder interferometer was investigated in cooperation with and assembled at the Laser Zentrum Hannover e.V. and is presented in Section 3.3. The generated total laser power of $398\,\mathrm{W}$ represents the highest so far measured power of a laser beam designed for GWDs. The spatial beam quality and free-running noise of the system was investigated and no significant increase in the combined beam's noise in comparison to the single beams was identified. The results of this work are published in the shared corresponding author paper [74] and in [75].
A future experiment to demonstrate $400\,\mathrm{W}$ of laser power in a PSL, based on the results from Section 3.2 and Section 3.3, is already under construction. Fiber laser amplifiers with power levels up to $365\,\mathrm{W}$ were demonstrated [64, 66] but do not yet fulfill all of the stringent GWD requirements. After further development, they might be used in similar CBC layouts as here presented to increase the laser power further.
Intended and unintended mismatches of the laser powers of the two to-be-combined laser beams limit the maximal available power in the combined beam if a $50:50$ beam splitter is used as combining element. Therefore, the usage of a beam splitter, with a variable ratio between transmission and reflection, could be beneficial to maximize the laser power generated in the CBC.
The benefits of using a variable beam splitter as combining element for the CBC of two laser beams with different laser powers and different seed sources are investigated in Section 3.4. The ratio between transmission and reflection of the variable beam splitter was successfully fit to the single beams' laser powers of $60\,\mathrm{W}$ and $100\,\mathrm{W}$ in a proof-of-principle experiment. A combined beam with about $145\,\mathrm{W}$ of laser power was generated in this scheme. Inspired from the obtained results, an improved variable beam splitter will be used in the mentioned $400\,\mathrm{W}$ PSL, which is under construction, to compensate for unintended power mismatches.
Chapter 4 is dedicated to novel technologies for the generation and transport of high power laser beams for future GWD's.
A power scaling above the level available from two amplifier chains, can be realized by the coherent combination of more than two laser beams. A new CBC technology for the combination of three laser beams is presented in Section 4.1. Three $5\,\mathrm{W}$ laser beams from a single seed laser source were combined at a bow-tie optical resonator as combining element in a proof-of-principle experiment. The combined beam had a laser power of $11.3\,\mathrm{W}$, where combination losses could be traced back to a high higher-order mode (HOM) content of the individual beams. The first relative power noise (RPN) measurements show only small differences between the combined beam and the single beams, and the next steps for a detailed characterization of the experiment, as well as a power scaling within this layout,

are discussed in detail. The combination on a resonator instead of a cascaded set of beam splitters could have several advantages, as, for example a high spatial beam quality of the combined beam, given by the resonators eigenmode. Furthermore, the resonator could serve as combining element and the PSL's PMC simultaneously and thereby reduce the system's complexity. With, for example, high power fiber laser amplifiers in all three beam paths, this technique is a promising candidate to reach the required power and spatial purity of future GWD laser systems.
The high power laser beams that are generated in the GWD PSLs need to be transported from the laser table to the GWD main vacuum system. The currently used insertion via transparent viewports is vulnerable to the coupling of ground movements or air fluctuations to the relative pointing of the laser beam. In addition, viewports can produce stray light or thermal effects scaling with the increased injected laser power that should be used in future detectors.
A promising solution to improve the transportation of the generated high power laser beams from the laser table to the GWD main vacuum system via a hollow core fiber is discussed in Section 4.2. In contrast to fibers with a solid core, hollow core fibers allow for the transportation of high laser powers over long fiber lengths, as the maximal laser power is not limited by stimulated Brillouin scattering. A customized hollow core fiber was used to transport an $85\,\mathrm{W}$ laser beam, which was beforehand filtered by an aLIGO pre-mode-cleaner (PMC). About $80\,\mathrm{W}$ of the injected power was transmitted by the fiber and the resulting beam was analyzed in comparison to the fiber's input laser beam. The spatial beam profile and especially the noise characteristics of the both beams are very similar, meaning that the transport did not substantially degrade the beam characteristics. Next tests with a new hollow core fiber are planned. Here the injected laser power will be increased to about $400\,\mathrm{W}$ to further identify limitations by the fiber. Additionally a coupling to a vacuum tank is planned to investigate the transmitted beam under realistic conditions.
In summary, the systems and techniques investigated in this thesis present the way from the development of the current GWD laser systems up to the complex technologies needed for the next generation of GWDs, including a possible transportation mechanism of the resulting high power laser beam.

Acknowledgements

I am part of the former Laser Group and now Laser and Squeezed Light Group at the Albert Einstein Institute Hanover since I started to work on my Bachelor Thesis. Coming to this institute was one of the best decisions I ever made and has shaped me personally and as a scientist in many ways. This institute offers interesting science, an exceptional infrastructure and a warm and friendly work atmosphere. I want to thank Karsten Danzmann a lot for creating such an amazing place.
My deepest gratitude goes to Benno Willke. You're group is a place that allows people to grow to independent scientists while they can still ask for support whenever they need to. I am really thankful for the interesting topics I could work on in the last years and for the possibility to develop a diverse set of skills. I enjoyed our discussions and am grateful for your patience and all the time you take for us. I always left your office with a better feeling than I had before. I also want to thank you for the possibility to visit different conferences and especially to spend three month as a research fellow at aLIGO Livingston. This was an amazing and motivating time that showed me even more how good you prepare us to work in science.
The time at the institute wouldn't have been the same without its people. I would like to thank you all for nice chats on the corridor, interesting presentations about the work that is done in other groups, amazing times at the lecture weeks and conferences, and of course the great Christmas and Halloween parties. Especially I want to thank the Members of the Kranoleum for the nice company at lunch, followed by challenging Rundlauf matches.
Of course, I would like to especially thank the actual and former members of the laser and squeezed light group. You are much more than just colleagues and I really enjoyed our group activities, including singing with you when Joscha played the guitar, our, sometimes stupid, conversations at lunch time, all the nice tea kitchen chats and not to forget the solution orientated and very helpful discussions about science. Your helpful suggestions, ideas and sometimes just you listening to my problems helped me in many situations and my thesis wouldn't be the same without all of you.
I also want to thank Patrick, Fabian and Christoph for our shared time in the labs. It is always helpful to discuss steps on the experiments in between and in addition it is also just nice to have another person around.
Thank you Marina, Patrick and especially Fabian for proofreading my thesis and all your helpful suggestions and comments.
For all the fruitful discussions during and outsides our meetings I want to thank our LZH collaborators. Especially I want to thank Felix Wellmann for the time on our joined project. I enjoyed working with you in the LZH labs and on our shared paper. In addition, I want to thank Sven Hochheim and Kristopher Kruska for all the help with the fiber amplifiers at the AEI.
I want to thank David Ottaway and Zac Holmes for the interesting discussions in our meetings regarding the PMC CBC experiment. Thank you Zac for our shared time at the AEI lab, while you were visiting us. It was really nice working with you.

A big thanks goes also to the electronic workshop, the mechanic workshop and the IT staff. Without your help I wouldn't have been able to focus on the science as I could. A special thanks goes also to Gerrit for always helping me fast with CDS related problems.
Finally, I want to thank my friends and family and especially my husband Chris. Thank you so much for all the support in the last years, I am lucky to have you by my side!

Bibliography

[1] Albert Einstein. "Näherungsweise Integration der Feldgleichungen der Gravitation". In: *Sitzungsbericht der Preußischen Akademie der Wissenschaften* (1916), pp. 688–696.

[2] LIGO Scientific Collaboration. "Advanced LIGO". In: *Classical and Quantum Gravity* 32.7 (Mar. 2015), p. 074001. DOI: 10.1088/0264-9381/32/7/074001. URL: https://doi.org/10.1088%2F0264-9381%2F32%2F7%2F074001.

[3] Virgo Collaboration. "Advanced Virgo: a second-generation interferometric gravitational wave detector". In: *Classical and Quantum Gravity* 32.2 (Dec. 2014), p. 024001. DOI: 10.1088/0264-9381/32/2/024001. URL: https://doi.org/10.1088%2F0264-9381%2F32%2F2%2F024001.

[4] LIGO-Virgo Collaboration. "Search for gravitational waves from Scorpius X-1 in the second Advanced LIGO observing run with an improved hidden Markov model". In: *Physical Review D* 100.12 (Dec. 2019), p. 122002. DOI: 10.1103/physrevd.100.122002.

[5] LIGO-Virgo Collaboration. "Open data from the first and second observing runs of Advanced LIGO and Advanced Virgo". In: *SoftwareX* 13 (Jan. 2021), p. 100658. DOI: 10.1016/j.softx.2021.100658.

[6] LIGO-Virgo Collaboration. *GWTC-2.1: Deep Extended Catalog of Compact Binary Coalescences Observed by LIGO and Virgo During the First Half of the Third Observing Run*. 2021. DOI: 10.48550/ARXIV.2108.01045.

[7] LIGO-Virgo-KAGRA Collaboration. *GWTC-3: Compact Binary Coalescences Observed by LIGO and Virgo During the Second Part of the Third Observing Run*. 2021. DOI: 10.48550/ARXIV.2111.03606.

[8] LIGO-Virgo Collaboration. "First narrow-band search for continuous gravitational waves from known pulsars in advanced detector data". In: *Physical Review D* 96.12 (Dec. 2017), p. 122006. DOI: 10.1103/physrevd.96.122006.

[9] KAGRA Collaboration. "KAGRA: 2.5 generation interferometric gravitational wave detector". In: *Nature Astronomy* 3.1 (Jan. 2019), pp. 35–40. DOI: 10.1038/s41550-018-0658-y.

[10] T Akutsu et al. "Overview of KAGRA: Detector design and construction history". In: *Progress of Theoretical and Experimental Physics* 2021.5 (Aug. 2020). DOI: 10.1093/ptep/ptaa125.

[11] B Willke et al. "The GEO 600 gravitational wave detector". In: *Classical and Quantum Gravity* 19.7 (Mar. 2002), pp. 1377–1387. DOI: 10.1088/0264-9381/19/7/321. URL: https://doi.org/10.1088/0264-9381/19/7/321.

[12] K L Dooley and. "Status of GEO 600". In: *Journal of Physics: Conference Series* 610 (May 2015), p. 012015. DOI: 10.1088/1742-6596/610/1/012015.

[13] LIGO-Virgo-KAGRA Collaboration. "First joint observation by the underground gravitational-wave detector KAGRA with GEO 600". In: *Progress of Theoretical and Experimental Physics* 2022.6 (June 2022). ISSN: 2050-3911. DOI: 10.1093/ptep/ptac073. eprint: https://academic.oup.com/ptep/article-pdf/2022/6/063F01/43989382/ptac073.pdf. URL: https://doi.org/10.1093/ptep/ptac073.

[14] Tarun Souradeep. "LIGO-India". In: *Resonance* 21.3 (Mar. 2016), pp. 225–231. DOI: 10.1007/s12045-016-0316-6.

[15] LIGO-Virgo Collaboration. "Gravitational-wave Constraints on the Equatorial Ellipticity of Millisecond Pulsars". In: *The Astrophysical Journal Letters* 902.1 (Oct. 2020), p. L21. DOI: 10.3847/2041-8213/abb655.

[16] Craig Cahillane and Georgia Mansell. "Review of the Advanced LIGO Gravitational Wave Observatories Leading to Observing Run Four". In: *Galaxies* 10.1 (Feb. 2022), p. 36. DOI: 10.3390/galaxies10010036.

[17] LIGO Scientific Collaboration. *Instrument Science White Paper 2021*. Tech. rep. LIGO-T2100298–v2. LIGO Scientific Collaboration, July 2021.

[18] Diego Bersanetti, Barbara Patricelli, Ornella Juliana Piccinni, Francesco Piergiovanni, Francesco Salemi, and Valeria Sequino. "Advanced Virgo: Status of the Detector, Latest Results and Future Prospects". In: *Universe* 7.9 (Aug. 2021), p. 322. DOI: 10.3390/universe7090322.

[19] Virgo Collaboration. *Advanced Virgo Plus Phase I*. Tech. rep. VIR - 0596A - 19. June 2019.

[20] ET steering committee. *ET design report update 2020*. Tech. rep. Sept. 2020.

[21] M Punturo et al. "The Einstein Telescope: a third-generation gravitational wave observatory". In: *Classical and Quantum Gravity* 27.19 (Sept. 2010), p. 194002. DOI: 10.1088/0264-9381/27/19/194002.

[22] Matthew Evans et al. *A Horizon Study for Cosmic Explorer: Science, Observatories, and Community*. 2021. DOI: 10.48550/ARXIV.2109.09882.

[23] LISA Collaboration. *Laser Interferometer Space Antenna*. 2017. DOI: 10.48550/ARXIV.1702.00786.

[24] Tobin T Fricke et al. "DC readout experiment in Enhanced LIGO". In: *Classical and Quantum Gravity* 29.6 (Feb. 2012), p. 065005. DOI: 10.1088/0264-9381/29/6/065005.

[25] Peter R. Saulson. *Fundamentals of Interferometric Gravitational Wave Detectors*. WORLD SCIENTIFIC, Oct. 1994. DOI: 10.1142/2410.

[26] R. W. P. Drever. "Laser Interferometer Gravitational Wave Detectors". In: *General Relativity and Gravitation*. Springer Netherlands, 1984, pp. 397–412. DOI: 10.1007/978-94-009-6469-3_23.

[27] Stefan Hild. "A Basic Introduction to Quantum Noise and Quantum-Non-Demolition Techniques". In: *Advanced Interferometers and the Search for Gravitational Waves*. Springer International Publishing, 2014, pp. 291–314. DOI: 10.1007/978-3-319-03792-9_11.

[28] Brian J. Meers. “Recycling in laser-interferometric gravitational-wave detectors”. In: *Physical Review D* 38.8 (Oct. 1988), pp. 2317–2326. DOI: 10.1103/physrevd.38.2317.

[29] Sheila E. Dwyer, Georgia L. Mansell, and Lee McCuller. “Squeezing in Gravitational Wave Detectors”. In: *Galaxies* 10.2 (Mar. 2022), p. 46. DOI: 10.3390/galaxies10020046.

[30] LIGO Scientific Collaboration. *Instrument Science White Paper 2020*. Tech. rep. LIGO-T2000407–v3. Aug. 2020.

[31] M. Punturo and K. Somiya. “Underground Gravitational Wave Observatories: KAGRA and ET”. In: *International Journal of Modern Physics D* 22.05 (Apr. 2013), p. 1330010. DOI: 10.1142/s0218271813300103.

[32] R X Adhikari et al. “A cryogenic silicon interferometer for gravitational-wave detection”. In: *Classical and Quantum Gravity* 37.16 (July 2020), p. 165003. DOI: 10.1088/1361-6382/ab9143.

[33] D. Shoemaker, R. Schilling, L. Schnupp, W. Winkler, K. Maischberger, and A. Rüdiger. “Noise behavior of the Garching 30-meter prototype gravitational-wave detector”. In: *Physical Review D* 38.2 (July 1988), pp. 423–432. DOI: 10.1103/physrevd.38.423.

[34] A. Buikema et al. “Sensitivity and performance of the Advanced LIGO detectors in the third observing run”. In: *Physical Review D* 102.6 (Sept. 2020), p. 062003. DOI: 10.1103/physrevd.102.062003.

[35] Benno Willke, Peter King, Rick Savage, and Peter Fritschel. *Pre-Stabilized Laser Design Requirements*. Tech. rep. LIGO-T050036-v4. LIGO Laboratory and LIGO Scientific Collaboration, July 2011.

[36] François Bondu and Olivier Debieu. “Accurate measurement method of Fabry-Perot cavity parameters via optical transfer function”. In: *Applied Optics* 46.14 (Apr. 2007), p. 2611. DOI: 10.1364/ao.46.002611.

[37] Patrick Kwee. “Laser Characterization and Stabilization for Precision Interferometry”. PhD thesis. Gottfried Wilhelm Leibniz Universität Hannover, 2010.

[38] Jan Põld. “Design, Implementation and Characterization of the Advanced LIGO 200WLaser System”. PhD thesis. Gottfried Wilhelm Leibniz Universität Hannover, 2014.

[39] Steffen Kaufer and Benno Willke. “Optical AC coupling power stabilization at frequencies close to the gravitational wave detection band”. In: *Optics Letters* 44.8 (Apr. 2019), p. 1916. DOI: 10.1364/ol.44.001916.

[40] Marina Trad Nery, Jasper R. Venneberg, Nancy Aggarwal, Garrett G. Cole, Thomas Corbitt, Jonathan Cripe, Robert Lanza, and Benno Willke. “Laser power stabilization via radiation pressure”. In: *Optics Letters* 46.8 (Apr. 2021), p. 1946. DOI: 10.1364/ol.422614.

[41] Henning Vahlbruch, Dennis Wilken, Moritz Mehmet, and Benno Willke. “Laser Power Stabilization beyond the Shot Noise Limit Using Squeezed Light”. In: *Physical Review Letters* 121.17 (Oct. 2018), p. 173601. DOI: 10.1103/physrevlett.121.173601.

[42] A. Rüdiger, R. Schilling, L. Schnupp, W. Winkler, H. Billing, and K. Maischberger. "A Mode Selector to Suppress Fluctuations in Laser Beam Geometry". In: *Optica Acta: International Journal of Optics* 28.5 (May 1981), pp. 641–658. DOI: 10.1080/713820609.

[43] Jan Hendrik Põld. *aLIGO bow-tie Pre-Modecleaner document*. Tech. rep. LIGO-T0900616-v3. Albert-Einstein-Institut Hannover, 2012.

[44] Eric D. Black. "An introduction to Pound–Drever–Hall laser frequency stabilization". In: *American Journal of Physics* 69.1 (Jan. 2001), pp. 79–87. DOI: 10.1119/1.1286663.

[45] L. Ju, D. G. Blair, and C. Zhao. "Detection of gravitational waves". In: *Reports on Progress in Physics* 63.9 (Aug. 2000), pp. 1317–1427. DOI: 10.1088/0034-4885/63/9/201. URL: https://doi.org/10.1088/0034-4885/63/9/201.

[46] Chris L. Mueller et al. "The advanced LIGO input optics". In: *Review of Scientific Instruments* 87.1 (Jan. 2016), p. 014502. DOI: 10.1063/1.4936974.

[47] Craig Cahillane, Georgia L. Mansell, and Daniel Sigg. "Laser frequency noise in next generation gravitational-wave detectors". In: *Optics Express* 29.25 (Dec. 2021), p. 42144. DOI: 10.1364/oe.439253.

[48] R Schilling, L Schnupp, W Winkler, H Billing, K Maischberger, and A Rudiger. "A method to blot out scattered light effects and its application to a gravitational wave detector". In: *Journal of Physics E: Scientific Instruments* 14.1 (Jan. 1981), pp. 65–70. DOI: 10.1088/0022-3735/14/1/018. URL: https://doi.org/10.1088/0022-3735/14/1/018.

[49] Thomas J. Kane and Robert L. Byer. "Monolithic, unidirectional single-mode Nd:YAG ring laser". In: *Optics Letters* 10.2 (Feb. 1985), p. 65. DOI: 10.1364/ol.10.000065.

[50] Patrick Kwee and Benno Willke. "Automatic laser beam characterization of monolithic Nd:YAG nonplanar ring lasers". In: *Applied Optics* 47.32 (Nov. 2008), p. 6022. DOI: 10.1364/ao.47.006022.

[51] Yingxin Bai. "Pumping wavelength related population inversion in Nd:doped laser". In: *AIP Advances* 10.10 (Oct. 2020), p. 105309. DOI: 10.1063/5.0006436.

[52] Walter Koechner. *Solid-State Laser Engineering*. Springer Berlin Heidelberg, 1999. DOI: 10.1007/978-3-662-14219-6.

[53] Maik Frede, Bastian Schulz, Ralf Wilhelm, Patrick Kwee, Frank Seifert, Benno Willke, and Dietmar Kracht. "Fundamental mode, single-frequency laser amplifier for gravitational wave detectors". In: *Optics Express* 15.2 (Jan. 2007), p. 459. DOI: 10.1364/oe.15.000459.

[54] Fabian Thies, Nina Bode, Patrick Oppermann, Maik Frede, Bastian Schulz, and Benno Willke. "Nd:YVO4 high-power master oscillator power amplifier laser system for second-generation gravitational wave detectors". In: *Optics Letters* 44.3 (Jan. 2019), p. 719. DOI: 10.1364/ol.44.000719.

[55] Nina Bode, Fabian Meylahn, and Benno Willke. "Sequential high power laser amplifiers for gravitational wave detection". In: *Optics Express* 28.20 (Sept. 2020), p. 29469. DOI: 10.1364/oe.401826.

[56] Nina Bode et al. "Advanced LIGO Laser Systems for O3 and Future Observation Runs". In: *Galaxies* 8.4 (Dec. 2020), p. 84. DOI: 10.3390/galaxies8040084.

[57] P. Kwee et al. "Stabilized high-power laser system for the gravitational wave detector advanced LIGO". In: *Optics Express* 20.10 (Apr. 2012), p. 10617. DOI: 10.1364/oe.20.010617.

[58] Michael Steinke et al. "Single-Frequency Fiber Amplifiers for Next-Generation Gravitational Wave Detectors". In: *IEEE Journal of Selected Topics in Quantum Electronics* 24.3 (May 2018), pp. 1–13. DOI: 10.1109/jstqe.2017.2759275.

[59] Felix Wellmann, Michael Steinke, Fabian Meylahn, Nina Bode, Benno Willke, Ludger Overmeyer, Jörg Neumann, and Dietmar Kracht. "High power, single-frequency, monolithic fiber amplifier for the next generation of gravitational wave detectors". In: *Optics Express* 27.20 (Sept. 2019), p. 28523. DOI: 10.1364/oe.27.028523.

[60] Felix Wellmann, Michael Steinke, Peter Wessels, Nina Bode, Fabian Meylahn, Benno Willke, Ludger Overmeyer, Jörg Neumann, and Dietmar Kracht. "Performance study of a high-power single-frequency fiber amplifier architecture for gravitational wave detectors". In: *Applied Optics* 59.26 (Sept. 2020), p. 7945. DOI: 10.1364/ao.401048.

[61] Jinye Zhang and M. R. Phillips. "Modeling Intensity Noise Caused by Stimulated Brillouin Scattering in Optical Fibers". In: *Conference on Lasers and Electro-Optics, Quantum Electronics and Laser Science and Photonic Applications Systems Technologies*. Optica Publishing Group, 2005, CMH6. URL: https://opg.optica.org/abstract.cfm?URI=CLEO-2005-CMH6.

[62] Thomas Theeg, Hakan Sayinc, Jörg Neumann, and Dietmar Kracht. "All-Fiber Counter-Propagation Pumped Single Frequency Amplifier Stage With 300-W Output Power". In: *IEEE Photonics Technology Letters* 24.20 (Oct. 2012), pp. 1864–1867. DOI: 10.1109/lpt.2012.2217487.

[63] V. I. Kovalev and R. G. Harrison. "Suppression of stimulated Brillouin scattering in high-power single-frequency fiber amplifiers". In: *Optics Letters* 31.2 (Jan. 2006), p. 161. DOI: 10.1364/ol.31.000161.

[64] Clément Dixneuf, Germain Guiraud, Yves-Vincent Bardin, Quentin Rosa, Mathieu Goeppner, Adèle Hilico, Christophe Pierre, Johan Boullet, Nicholas Traynor, and Giorgio Santarelli. "Ultra-low intensity noise, all fiber 365 W linearly polarized single frequency laser at 1064 nm". In: *Optics Express* 28.8 (Mar. 2020), p. 10960. DOI: 10.1364/oe.385095.

[65] Sven Hochheim, Michael Steinke, Peter Wessels, Omar de Varona, Joona Koponen, Tyson Lowder, Steffen Novotny, Jörg Neumann, and Dietmar Kracht. "Single-frequency chirally coupled-core all-fiber amplifier with 100 W in a linearly polarized TEM00 mode". In: *Optics Letters* 45.4 (Feb. 2020), p. 939. DOI: 10.1364/ol.379002.

[66] Sven Hochheim, Eike Brockmüller, Peter Wessels, Joona Koponen, Tyson Lowder, Steffen Novotny, Benno Willke, Jörg Neumann, and Dietmar Kracht. “Single-Frequency 336 W Spliceless All-Fiber Amplifier Based on a Chirally-Coupled-Core Fiber for the Next Generation of Gravitational Wave Detectors”. In: *J. Lightwave Technol.* 40.7 (Apr. 2022), pp. 2136–2143. URL: https://opg.optica.org/jlt/abstract.cfm?URI=jlt-40-7-2136.

[67] Radoslaw Uberna, Andrew Bratcher, and Bruce G. Tiemann. “Coherent Polarization Beam Combination”. In: *IEEE Journal of Quantum Electronics* 46.8 (Aug. 2010), pp. 1191–1196. DOI: 10.1109/jqe.2010.2044976.

[68] Yanxing Ma et al. “Coherent beam combination of 108 kW fiber amplifier array using single frequency dithering technique”. In: *Optics Letters* 36.6 (Mar. 2011), p. 951. DOI: 10.1364/ol.36.000951.

[69] Pengfei Ma et al. “7.1 kW coherent beam combining system based on a seven-channel fiber amplifier array”. In: *Optics and Laser Technology* 140 (2021), p. 107016. ISSN: 0030-3992. DOI: https://doi.org/10.1016/j.optlastec.2021.107016. URL: https://www.sciencedirect.com/science/article/pii/S0030399221001043.

[70] C. X. Yu, S. J. Augst, S. M. Redmond, K. C. Goldizen, D. V. Murphy, A. Sanchez, and T. Y. Fan. “Coherent combining of a 4 kW, eight-element fiber amplifier array”. In: *Optics Letters* 36.14 (July 2011), p. 2686. DOI: 10.1364/ol.36.002686.

[71] T.Y. Fan. “Laser beam combining for high-power, high-radiance sources”. In: *IEEE Journal of Selected Topics in Quantum Electronics* 11.3 (May 2005), pp. 567–577. DOI: 10.1109/jstqe.2005.850241.

[72] Li-Wei Wei, Frédéric Cleva, and Catherine Nary Man. “Coherently combined master oscillator fiber power amplifiers for Advanced Virgo”. In: *Optics Letters* 41.24 (Dec. 2016), p. 5817. DOI: 10.1364/ol.41.005817.

[73] Henrik Tünnermann, Jan Hendrik Pöld, Jörg Neumann, Dietmar Kracht, Benno Willke, and Peter Weßels. “Beam quality and noise properties of coherently combined ytterbium doped single frequency fiber amplifiers”. In: *Optics Express* 19.20 (Sept. 2011), p. 19600. DOI: 10.1364/oe.19.019600.

[74] Felix Wellmann, Nina Bode, Peter Wessels, Ludger Overmeyer, Jörg Neumann, Benno Willke, and Dietmar Kracht. “Low noise 400 W coherently combined single frequency laser beam for next generation gravitational wave detectors”. In: *Optics Express* 29.7 (Mar. 2021), p. 10140. DOI: 10.1364/oe.420350.

[75] Felix Wellmann. “Monolithic fiber amplifiers for high power single-frequency and single-mode laser beam generation”. PhD thesis. Gottfried Wilhelm Leibniz Universität Hannover, 2021.

[76] Nina Bode. “Coherent beam combination and power actuation of high power lasers for gravitational wave detectors”. MA thesis. Gottfried Wilhelm Leibniz Universitaet Hannover, Apr. 2017.

[77] Patrick Kwee, Frank Seifert, Benno Willke, and Karsten Danzmann. "Laser beam quality and pointing measurement with an optical resonator". In: *Review of Scientific Instruments* 78.7 (July 2007), p. 073103. DOI: 10.1063/1.2754400.

[78] Rolf Bork, Jonathan Hanks, David Barker, Joseph Betzwieser, Jameson Rollins, Keith Thorne, and Erik von Reis. "advligorts: The Advanced LIGO real-time digital control and data acquisition system". In: *SoftwareX* 13 (Jan. 2021), p. 100619. DOI: 10.1016/j.softx.2020.100619.

[79] B. Willke, N. Uehara, E. K. Gustafson, R. L. Byer, P. J. King, S. U. Seel, and R. L. Savage. "Spatial and temporal filtering of a 10-W Nd:YAG laser with a Fabry–Perot ring-cavity premode cleaner". In: *Optics Letters* 23.21 (Nov. 1998), p. 1704. DOI: 10.1364/ol.23.001704.

[80] Jian Liu, Rick Savage, Peter King, Liyuan Zhang, and Stephen Appert. *aLIGO all-bolted PMC*. Tech. rep. LIGO-T1700543. LIGO Laboratory / LSC, Nov. 2017.

[81] Patrick Kwee, Benno Willke, and Karsten Danzmann. "Shot-noise-limited laser power stabilization with a high-power photodiode array". In: *Optics Letters* 34.19 (Sept. 2009), p. 2912. DOI: 10.1364/ol.34.002912.

[82] A. White. "Frequency stabilization of gas lasers". In: *IEEE Journal of Quantum Electronics* 1.8 (Nov. 1965), pp. 349–357. DOI: 10.1109/jqe.1965.1072246.

[83] Euan Morrison, Brian J. Meers, David I. Robertson, and Henry Ward. "Automatic alignment of optical interferometers". In: *Applied Optics* 33.22 (Aug. 1994), p. 5041. DOI: 10.1364/ao.33.005041.

[84] Anthony E. Siegman. *Lasers*. University Science Books, 1986.

[85] Henrik Tünnermann, Jörg Neumann, Dietmar Kracht, and Peter Weßels. "Gain dynamics and refractive index changes in fiber amplifiers: a frequency domain approach". In: *Opt. Express* 20.12 (June 2012), pp. 13539–13550. DOI: 10.1364/OE.20.013539. URL: http://www.opticsexpress.org/abstract.cfm?URI=oe-20-12-13539.

[86] Stephanie Novak and Adolph Moesle. "Analytic Model for Gain Modulation in EDFAs". In: *J. Lightwave Technol.* 20.6 (June 2002), p. 975. URL: http://jlt.osa.org/abstract.cfm?URI=jlt-20-6-975.

[87] Frédéric Cleva, Jean-Pierre Coulon, and Fabien Kéfélian. "Characterization, Integration and Operation of a 100 W Solid State Amplifier in the Advanced-VIRGO Pre-Stabilized Laser System". In: *2019 Conference on Lasers and Electro-Optics Europe and European Quantum Electronics Conference*. Optical Society of America, 2019, pp. 2–4. URL: http://www.osapublishing.org/abstract.cfm?URI=CLEO_Europe-2019-ca_2_4.

[88] R. S. Abbott and P. J. King. "Diode-pumped Nd:YAG laser intensity noise suppression using a current shunt". In: *Review of Scientific Instruments* 72.2 (2001), p. 1346. DOI: 10.1063/1.1334627.

[89] Christoph Gentemann. "Coherent combination of two high power neodymium vanadate amplifiers". MA thesis. Gottfried Wilhelm Leibniz Universität Hannover, July 2021.

[90] A. Ashkin, G. D. Boyd, J. M. Dziedzic, R. G. Smith, A. A. Ballman, J. J. Levinstein, and K. Nassau. “Optically-induced refractive index inhomogeneities in LiNbO3 and LiTaO3”. In: *Applied Physics Letters* 9.1 (July 1966), pp. 72–74. DOI: 10.1063/1.1754607.

[91] Christina Bogan. “Stabilized high power lasers and spatial mode conversion”. PhD thesis. Gottfried Wilhelm Leibniz Universität Hannover, 2013.

[92] L. Winkelmann et al. “Injection-locked single-frequency laser with an output power of 220 W”. In: *Applied Physics B* 102.3 (Feb. 2011), pp. 529–538. DOI: 10.1007/s00340-011-4411-9.

[93] H.J. Eichler, B. Liu, M. Kayser, and S.I. Khomenko. “Er:YAG-laser at 2.94 μm Q-switched by a FTIR-shutter with silicon output coupler and polarizer”. In: *Optical Materials* 5.4 (May 1996), pp. 259–265. DOI: 10.1016/0925-3467(96)00006-7.

[94] W. Demtröder. *Atoms, molecules and photons an introduction to atomic-, molecular- and quantum-physics. an introduction to atomic-, molecular- and quantum-physics*. Springer, 2010, p. 589. ISBN: 9783642102974.

[95] S. Zhu, A. W. Yu, D. Hawley, and R. Roy. “Frustrated total internal reflection: A demonstration and review”. In: *American Journal of Physics* 54.7 (July 1986), pp. 601–607. DOI: 10.1119/1.14514.

[96] Ajoy Ghatak and K. Thyagarajan. “Propagation characteristics of a step index fiber”. In: *Introduction to fiber optics*. Cambridge University Press, 1998, pp. 132–172. DOI: 10.1017/cbo9781139174770.009.

[97] Anders Bjarklev, Jes Broeng, and Araceli Sanchez Bjarklev. *Photonic Crystal Fibres*. Springer US, 2003. DOI: 10.1007/978-1-4615-0475-7.

[98] I. Gris-Sanchez and J. C. Knight. “Time-Dependent Degradation of Photonic Crystal Fiber Attenuation Around OH Absorption Wavelengths”. In: *Journal of Lightwave Technology* 30.23 (Dec. 2012), pp. 3597–3602. DOI: 10.1109/jlt.2012.2223453.

[99] Andreas Freise and Kenneth Strain. “Interferometer Techniques for Gravitational-Wave Detection”. In: *Living Reviews in Relativity* 13.1 (Feb. 2010). DOI: 10.12942/lrr-2010-1.

A. Coherent beam combination on a beam splitter

In this chapter the formalism used in this thesis for the coherent combination of two laser beams on a beam splitter is presented. The basic equations for the beam splitter outputs are derived in Appendix A.1. In Appendix A.2 the relative power noise (RPN) of the combined beam dependent on the RPN of the two input beams is evaluated for uncorrelated and correlated noise contributions.

A.1. Coherent combination formalism

All calculations in this chapter are based on the input and output fields on a beam splitter with the amplitude coefficients for transmission and reflection τ and ρ, respectively, as depicted in figure A.1. The basic formalism used for the following calculations is adapted from [99]. The amplitude coefficients for transmission and reflection for an ideal beam splitter, are related as described in Equation (A.1). The

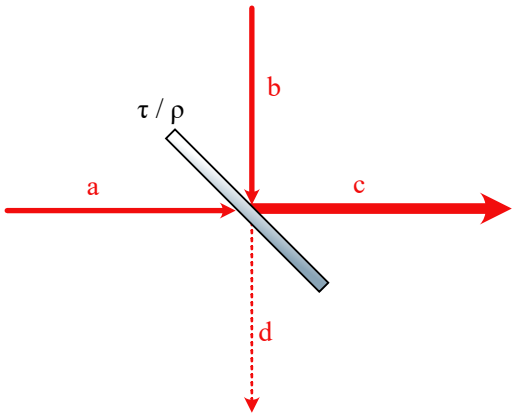

Figure A.1.: Beam a and b are coherently combined on a beam splitter with the amplitude coefficients for transmission and reflection τ and ρ, respectively.

$$\tau^2 + \rho^2 = 1 \tag{A.1}$$

$$a = a_0 e^{i\varphi_\mathrm{a}} \tag{A.2}$$

$$b = b_0 e^{i\varphi_\mathrm{b}} \tag{A.3}$$

$$c = i\tau a + \rho b \tag{A.4}$$

$$d = \rho a + i\tau b \tag{A.5}$$

$$P_\mathrm{a} = |a|^2 = a \cdot a^* \tag{A.6}$$

field amplitudes of the two input fields are described as a and b in Equation (A.2) and Equation (A.3), respectively. The field amplitudes of the two output fields c and d are derived as a combination of the transmitted and reflected part from the two input fields and can be described via Equation (A.4) and Equation (A.5). The optical power of a field amplitude is calculated as in Equation (A.6).

With this formalism the power of the output field c can be evaluated to:

$$P_\mathrm{c} = |\tau|^2|a_0|^2 + |\rho|^2|b_0|^2 + i\tau\rho a_0 b_0(e^{i(\varphi_\mathrm{a}-\varphi_\mathrm{b})} - e^{-i(\varphi_\mathrm{a}-\varphi_\mathrm{b})}). \tag{A.7}$$

With the phase difference between the two input fields $\Delta\varphi = \varphi_\mathrm{a} - \varphi_\mathrm{b}$ and the relation $\sin x = \frac{1}{2i}(e^{ix} - e^{-ix})$ this is rewritten to:

$$P_\mathrm{c} = |\tau|^2 P_\mathrm{a} + |\rho|^2 P_\mathrm{b} - 2\tau\rho a_0 b_0 \sin(\Delta\varphi). \tag{A.8}$$

The power of the output field d is equivalently derived as:

$$P_\mathrm{d} = |\rho|^2 P_\mathrm{a} + |\tau|^2 P_\mathrm{b} + 2\tau\rho a_0 b_0 \sin(\Delta\varphi). \tag{A.9}$$

For equal input powers $P_\mathrm{a} = P_\mathrm{b} = P_\mathrm{in}$ and a $50:50$ beam splitter with $\tau = \rho = \sqrt{0.5}$ this the output powers are derived as:

$$P_\mathrm{c} = P_\mathrm{in}(1 + \sin(\Delta\varphi) \tag{A.10}$$
$$P_\mathrm{d} = P_\mathrm{in}(1 - \sin(\Delta\varphi). \tag{A.11}$$

A.2. Relative Power Noise

If a relative power noise term is added to the input beams they look as follows:

$$a = a_0 e^{i\varphi_\mathrm{a}}(1 + \tilde{m}_\mathrm{a}\cos(\Omega t)) \tag{A.12}$$
$$b = b_0 e^{i\varphi_\mathrm{b}}(1 + \tilde{m}_\mathrm{b}\cos(\Omega t)) \tag{A.13}$$

The outputs are then given as:

$$c = i\tau a_0 e^{i\varphi_\mathrm{a}}(1 + \tilde{m}_\mathrm{a}\cos(\Omega t)) + \rho b_0 e^{i\varphi_\mathrm{b}}(1 + \tilde{m}_\mathrm{b}\cos(\Omega t)) \tag{A.14}$$
$$d = \rho a_0 e^{i\varphi_\mathrm{a}}(1 + \tilde{m}_\mathrm{a}\cos(\Omega t)) + i\tau b_0 e^{i\varphi_\mathrm{b}}(1 + \tilde{m}_\mathrm{b}\cos(\Omega t)) \tag{A.15}$$

The output power of c can then be calculated as:

$$\begin{aligned} P_\mathrm{c} =& |c|^2 = c \cdot c* \\ =& [i\tau a_0 e^{i\varphi_\mathrm{a}}(1 + \tilde{m}_\mathrm{a}\cos(\Omega t)) + \rho b_0 e^{i\varphi_\mathrm{b}}(1 + \tilde{m}_\mathrm{b}\cos(\Omega t))] \cdot c.c. \\ \approx& \tau^2|a_0|^2(1 + 2\tilde{m}_\mathrm{a}\cos^2(\Omega t)) \\ &+ i\tau\rho a_0 b_0 e^{i(\varphi_\mathrm{a}-\varphi_\mathrm{b})t}(1 + \tilde{m}_\mathrm{a}\cos(\Omega t))(1 + \tilde{m}_\mathrm{b}\cos(\Omega t)) \\ &- i\tau\rho a_0 b_0 e^{-i(\varphi_\mathrm{a}-\varphi_\mathrm{b})t}(1 + \tilde{m}_\mathrm{a}\cos(\Omega t))(1 + \tilde{m}_\mathrm{b}\cos(\Omega t)) \\ &+ \rho^2|b_0|^2(1 + 2\tilde{m}_\mathrm{b}\cos^2(\Omega t)) \end{aligned} \tag{A.16}$$

With:

$$\begin{aligned} (1 + \tilde{m}_\mathrm{a}\cos(\Omega t))(1 + \tilde{m}_\mathrm{b}\cos(\Omega t)) =& 1 + \tilde{m}_\mathrm{a}\cos(\Omega t) + \tilde{m}_\mathrm{b}\cos(\Omega t) \\ &+ \tilde{m}_\mathrm{a}\tilde{m}_\mathrm{b}\cos^2(\Omega t) \\ \approx& 1 + \tilde{m}_\mathrm{a}\cos(\Omega t) + \tilde{m}_\mathrm{b}\cos(\Omega t) \end{aligned} \tag{A.17}$$

One can write:

$$\begin{aligned} P_\mathrm{c} \approx & \tau^2|a_0|^2(1+2\tilde{m}_\mathrm{a}\cos(\Omega t)) \\ & + i\tau\rho a_0 b_0 e^{i(\varphi_\mathrm{a}-\varphi_\mathrm{b})t}(1+\tilde{m}_\mathrm{a}\cos(\Omega t)+\tilde{m}_\mathrm{b}\cos(\Omega t)) \\ & - i\tau\rho a_0 b_0 e^{-i(\varphi_\mathrm{a}-\varphi_\mathrm{b})t}(1+\tilde{m}_\mathrm{a}\cos(\Omega t)+\tilde{m}_\mathrm{b}\cos(\Omega t)) \\ & + \rho^2|b_0|^2(1+2\tilde{m}_\mathrm{b}\cos(\Omega t)). \end{aligned} \tag{A.18}$$

If P_c is split in its carrier and noise terms and $\varphi_\mathrm{a}-\varphi_\mathrm{b}=\Delta\varphi$:

$$\begin{aligned} P_\mathrm{c} \approx & \tau^2|a_0|^2+\rho^2|b_0|^2+i\tau\rho a_0 b_0(e^{i\Delta\varphi}-e^{-i\Delta\varphi}) \\ & + 2(\tau^2|a_0|^2\tilde{m}_\mathrm{a}+\rho^2|b_0|^2\tilde{m}_\mathrm{b})\cos(\Omega t) \\ & + i\tau\rho a_0 b_0(e^{i\Delta\varphi}-e^{-i\Delta\varphi})(\tilde{m}_\mathrm{a}+\tilde{m}_\mathrm{b})\cos(\Omega t). \end{aligned} \tag{A.19}$$

With $e^{i\Delta\varphi}-e^{-i\Delta\varphi}=-2i\sin(\Delta\varphi)$ we get:

$$\begin{aligned} P_\mathrm{c} \approx & \tau^2|a_0|^2+\rho^2|b_0|^2+2\tau\rho a_0 b_0\sin(\Delta\varphi) \\ & + 2(\tau^2|a_0|^2\tilde{m}_\mathrm{a}+\rho^2|b_0|^2\tilde{m}_\mathrm{b})\cos(\Omega t) \\ & + 2\tau\rho a_0 b_0\sin(\Delta\varphi)(\tilde{m}_\mathrm{a}+\tilde{m}_\mathrm{b})\cos(\Omega t) \end{aligned} \tag{A.20}$$

Rewriting this in the form $P_\mathrm{c}=|c_0|^2\cdot[1+2\tilde{m}_\mathrm{c}\cos(\Omega t)]$ one gets:

$$|c_0|^2 \approx \tau^2|a_0|^2+\rho^2|b_0|^2+2\tau\rho a_0 b_0\sin(\Delta\varphi) \tag{A.21}$$

$$\tilde{m}_\mathrm{c} \approx \frac{\tau^2|a_0|^2\tilde{m}_\mathrm{a}+\rho^2|b_0|^2\tilde{m}_\mathrm{b}+\tau\rho a_0 b_0\sin(\Delta\varphi)(\tilde{m}_\mathrm{a}+\tilde{m}_\mathrm{b})}{\tau^2|a_0|^2+\rho^2|b_0|^2+2\tau\rho a_0 b_0\sin(\Delta\varphi)}. \tag{A.22}$$

With $RPN_\mathrm{c}=2\cdot\tilde{m}_\mathrm{c}$. This can now be split in two cases. The first one is the case for **correlated noise**.

A.2.1. Correlated relative power noise

If the relative power noise of the two input beams origins from the same noise source it is correlated.

Equal Power and Beam Splitter

Assuming the input power to be equal $a_0=b_0$ and a $50/50$ beam splitter ($\tau=\rho=\sqrt{1/2}$), equation A.22 can be rewritten to:

$$\begin{aligned} \tilde{m}_\mathrm{c} &= \frac{1}{2}\frac{|a_0|^2(1+\sin(\Delta\varphi))(\tilde{m}_\mathrm{a}+\tilde{m}_\mathrm{b})}{|a_0|^2(1+\sin(\Delta\varphi))} \\ &= \frac{1}{2}(\tilde{m}_\mathrm{a}+\tilde{m}_\mathrm{b}). \end{aligned} \tag{A.23}$$

The relative power noise is then:

$$RPN_\mathrm{c}=\frac{1}{2}(RPN_\mathrm{a}+RPN_\mathrm{b}) \tag{A.24}$$

A.2.2. Uncorrelated relative power noise

The noise is uncorrelated if there are for example two laser sources that are combined. It is also valid if one seed source is split up and amplified, but the RPN of the amplified beams is pump dominated. In this case the noise adds quadratical:

$$\tilde{m}_\mathrm{c} \approx \frac{\sqrt{\tau^4|a_0|^4\tilde{m}_\mathrm{a}^2 + \rho^4|b_0|^4\tilde{m}_\mathrm{b}^2 + \tau^2\rho^2a_0^2b_0^2\sin^2(\Delta\varphi)(\tilde{m}_\mathrm{a}^2+\tilde{m}_\mathrm{b}^2)}}{\tau^2|a_0|^2 + \rho^2|b_0|^2 + 2\tau\rho a_0 b_0\sin(\Delta\varphi)}. \tag{A.25}$$

Equal Power and Beam Splitter

Assuming the input power to be equal $a_0 = b_0$ and a $50/50$ beam splitter ($\tau = \rho = \sqrt{1/2}$), equation A.25 can be rewritten to:

$$\begin{aligned}
\tilde{m}_\mathrm{c} &= \frac{1}{2}\frac{|a_0|^2\sqrt{1+\sin^2(\Delta\varphi)}\sqrt{\tilde{m}_\mathrm{a}^2+\tilde{m}_\mathrm{b}^2}}{|a_0|^2(1+\sin(\Delta\varphi))} \\
&= \frac{1}{2}\frac{|a_0|^2}{|c_0|^2}\sqrt{\frac{|c_0|^4}{|a_0|^4} - 2\frac{|c_0|^2}{|a_0|^2} + 2}\cdot\sqrt{\tilde{m}_\mathrm{a}^2+\tilde{m}_\mathrm{b}^2} \\
&= \frac{1}{2}\sqrt{1 - 2\frac{|a_0|^2}{|c_0|^2} + 2\frac{|a_0|^4}{|c_0|^4}}\cdot\sqrt{\tilde{m}_\mathrm{a}^2+\tilde{m}_\mathrm{b}^2}
\end{aligned}$$

The relative power noise is then:

$$RPN_\mathrm{c} = \frac{1}{2}\sqrt{1 - 2\frac{|a_0|^2}{|c_0|^2} + 2\frac{|a_0|^4}{|c_0|^4}}\sqrt{RPN_\mathrm{a}^2 + RPN_\mathrm{b}^2} \tag{A.26}$$

This results in different a different RPN for measurements at the bright port and the dark port.

B. Equations for the coherent beam combination on a bow-tie resonator

In this chapter the basic equations for the coherent combination of three laser beams on a bow-tie optical resonator are given. It serves as a reference for Section 4.1. The given formulas are used in a Mathematica script to calculate the expected output power of the used resonator and to calculate the required mirror reflectivities for given parameters via maximization calculations.

Layout

Figure B.1 shows a bow-tie resonator with with the three input fields a_1, a_2, and a_3, one combined output field a_4 and the circulating field a_{circ}. The three reflected fields are named d_1, d_2, and d_3. Each resonator mirror has a amplitude transmission coefficient τ and amplitude reflection coefficient ρ.

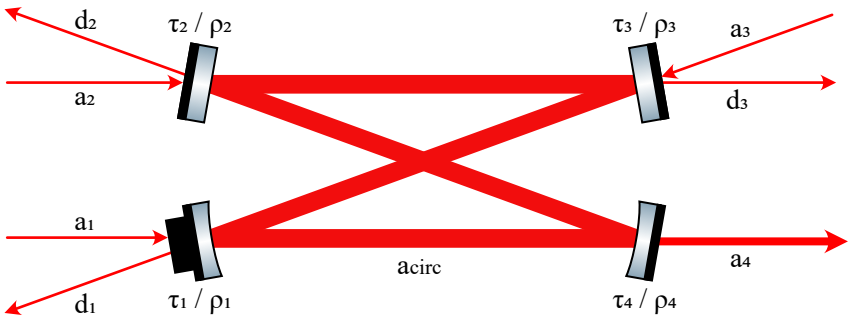

Figure B.1.: Bow-tie resonator with the three input fields a_1, a_2, a_3, one combined output field a_4 and the circulating field a_{circ}.

Mirror transmissivities

The amplitude transmission and reflection coefficients are related to each other as follows:

$$\tau_1(\rho_1) = \sqrt{1-\rho_1^2}, \tag{B.1}$$

$$\tau_2(\rho_2) = \sqrt{1-\rho_2^2}, \tag{B.2}$$

$$\tau_3(\rho_3) = \sqrt{1-\rho_3^2}. \tag{B.3}$$

Round-trip loss

The losses experienced by the circulating light in one round-trip in the resonator, are given by:

$$r(\rho_1, \rho_2, \rho_3, \rho_4) = \sqrt{\rho_1^2 \cdot \rho_2^2 \cdot \rho_3^2 \cdot \rho_4^2}. \tag{B.4}$$

Resonator finesse

The resonators finesse is calculated with:

$$\mathcal{F} = \frac{\pi\sqrt{r(\rho_1, \rho_2, \rho_3, \rho_4)}}{1 - r(\rho_1, \rho_2, \rho_3, \rho_4)}. \tag{B.5}$$

Circulating field

The resonators circulating field is calculated by:

$$a_{\text{circ}} = \frac{a_1 i\tau_1 + a_2 i\tau_2\rho_3\rho_1 + a_3 i\tau_3\rho_1}{1 - r(\rho_1, \rho_2, \rho_3, \rho_4)}. \tag{B.6}$$

This can be further used to calculate the resonator output fields, as follows.

Reflected output fields

The three reflected output fields are calculated by:

$$d_1 = a_1\rho_1 - a_{\text{circ}}\frac{i\tau_1}{\rho_2 \cdot \rho_4 \cdot \rho_3}, \tag{B.7}$$

$$d_2 = a_2\rho_2 - a_{\text{circ}}\frac{i\tau_2}{\rho_3 \cdot \rho_1}, \tag{B.8}$$

$$d_3 = a_3\rho_3 - a_{\text{circ}}\frac{i\tau_3}{\rho_2 \cdot \rho_4}. \tag{B.9}$$

Combined output field

The combined output field is calculated with:

$$a_4 = a_{\text{circ}} \cdot i\tau_4. \tag{B.10}$$

Power at combined output port

The power at the combined output field is calculated with:

$$P_4 = |a_4|^2. \tag{B.11}$$

The input powers in Section 4.1 are: $P_1 = P_2 = P_3 = 5\,\text{W}$ and mirror reflectivities $\rho_1 = \rho_2 = \rho_3 = \sqrt{0.9916}$ and $\rho_4 = \sqrt{0.975}$. The laser powers injected to the resonator are reduced due to the laser beams' HOMs of $HOM_1 = 25\,\%$, $HOM_2 = 26\,\%$ and $HOM_3 = 20\,\%$. Therewith the expected calculated combined laser power is:

$$P_a = 11.4467\,\text{W}. \tag{B.12}$$

Curriculum Vitae

Personal Information

	Nina Bode Born on June 30, 1990 in Hanover, Germany

University Studies

Since May 2017	Doctoral student in Physics Max Planck Institute for Gravitational Physics and, Institute for Gravitational Physics, Leibniz University Hanover, Germany
April 2015 - April 2017	Master of Science in Physics, Leibniz University Hanover
October 2010 - April 2015	Bachelor of Science, Leibniz University Hanover

Education

June 2010	Abitur, Victoria-Luise-Gymnasium in Hameln

Fellowship

July 2019 - October 2019	LIGO fellow at LIGO Livingston, Lousiana, USA

Publications

First author publications

[1] Nina Bode, Fabian Meylahn, and Benno Willke. "Sequential high power laser amplifiers for gravitational wave detection". In: *Optics Express* 28.20 (Sept. 2020), p. 29469. DOI: 10.1364/oe.401826.

[2] Nina Bode et al. "Advanced LIGO Laser Systems for O3 and Future Observation Runs". In: *Galaxies* 8.4 (Dec. 2020), p. 84. DOI: 10.3390/galaxies8040084.

[3] Felix Wellmann, Nina Bode, Peter Wessels, Ludger Overmeyer, Jörg Neumann, Benno Willke, and Dietmar Kracht. "Low noise 400 W coherently combined single frequency laser beam for next generation gravitational wave detectors". In: *Optics Express* 29.7 (Mar. 2021), p. 10140. DOI: 10.1364/oe.420350.

Other publications

[1] Fabian Thies, Nina Bode, Patrick Oppermann, Maik Frede, Bastian Schulz, and Benno Willke. "Nd:YVO4 high-power master oscillator power amplifier laser system for second-generation gravitational wave detectors". In: *Optics Letters* 44.3 (Jan. 2019), p. 719. DOI: 10.1364/ol.44.000719.

[2] Felix Wellmann, Michael Steinke, Fabian Meylahn, Nina Bode, Benno Willke, Ludger Overmeyer, Jörg Neumann, and Dietmar Kracht. "High power, single-frequency, monolithic fiber amplifier for the next generation of gravitational wave detectors". In: *Optics Express* 27.20 (Sept. 2019), p. 28523. DOI: 10.1364/oe.27.028523.

[3] Felix Wellmann, Michael Steinke, Peter Wessels, Nina Bode, Fabian Meylahn, Benno Willke, Ludger Overmeyer, Jörg Neumann, and Dietmar Kracht. "Performance study of a high-power single-frequency fiber amplifier architecture for gravitational wave detectors". In: *Applied Optics* 59.26 (Sept. 2020), p. 7945. DOI: 10.1364/ao.401048.

Collaboration publications

[1] LIGO-Virgo Collaboration. "First narrow-band search for continuous gravitational waves from known pulsars in advanced detector data". In: *Physical Review D* 96.12 (Dec. 2017), p. 122006. DOI: 10.1103/physrevd.96.122006.

[2] LIGO-Virgo Collaboration. "GW170608: Observation of a 19 Solar-mass Binary Black Hole Coalescence". In: *The Astrophysical Journal* 851.2 (Dec. 2017), p. L35. DOI: 10.3847/2041-8213/aa9f0c.

[3] LIGO-Virgo Collaboration. "Search for Post-merger Gravitational Waves from the Remnant of the Binary Neutron Star Merger GW170817". In: *The Astrophysical Journal* 851.1 (Dec. 2017), p. L16. DOI: 10.3847/2041-8213/aa9a35.

[4] LIGO-Virgo Collaboration. "First low-frequency Einstein@Home all-sky search for continuous gravitational waves in Advanced LIGO data". In: *Physical Review D* 96.12 (Dec. 2017), p. 122004. DOI: 10.1103/physrevd.96.122004.

[5] LIGO-Virgo Collaboration. "On the Progenitor of Binary Neutron Star Merger GW170817". In: *The Astrophysical Journal* 850.2 (Dec. 2017), p. L40. DOI: 10.3847/2041-8213/aa93fc.

[6] LIGO-Virgo Collaboration. "Estimating the Contribution of Dynamical Ejecta in the Kilonova Associated with GW170817". In: *The Astrophysical Journal* 850.2 (Dec. 2017), p. L39. DOI: 10.3847/2041-8213/aa9478.

[7] LIGO-Virgo-Collaboration, 1M2H, Dark Energy Camera GW-E, DES, DLT40, Las Cumbres Observatory, VINROUGE, MASTER. "A gravitational-wave standard siren measurement of the Hubble constant". In: *Nature* 551.7678 (Oct. 2017), pp. 85–88. DOI: 10.1038/nature24471.

[8] LIGO-Virgo Collaboration, Fermi GBM, INTEGRAL. "Gravitational Waves and Gamma-Rays from a Binary Neutron Star Merger: GW170817 and GRB 170817A". In: *The Astrophysical Journal* 848.2 (Oct. 2017), p. L13. DOI: 10.3847/2041-8213/aa920c.

[9] LIGO-Virgo Collaboration. "All-sky search for periodic gravitational waves in the O1 LIGO data". In: *Physical Review D* 96.6 (Sept. 2017), p. 062002. DOI: 10.1103/physrevd.96.062002.

[10] LIGO–Virgo Collaboration. "Upper Limits on Gravitational Waves from Scorpius X-1 from a Model-based Cross-correlation Search in Advanced LIGO Data". In: *The Astrophysical Journal* 847.1 (Sept. 2017), p. 47. DOI: 10.3847/1538-4357/aa86f0.

[11] LIGO-Virgo Collaboration. "Search for intermediate mass black hole binaries in the first observing run of Advanced LIGO". In: *Physical Review D* 96.2 (July 2017), p. 022001. DOI: 10.1103/physrevd.96.022001.

[12] LIGO-Virgo Collaboration. "Search for gravitational waves from Scorpius X-1 in the first Advanced LIGO observing run with a hidden Markov model". In: *Physical Review D* 95.12 (June 2017), p. 122003. DOI: 10.1103/physrevd.95.122003.

[13] LIGO-Virgo Collaboration. "GW170817: Observation of Gravitational Waves from a Binary Neutron Star Inspiral". In: *Physical Review Letters* 119.16 (Oct. 2017), p. 161101. DOI: 10.1103/physrevlett.119.161101.

[14] LIGO-Virgo Collaboration. "GW170814: A Three-Detector Observation of Gravitational Waves from a Binary Black Hole Coalescence". In: *Physical Review Letters* 119.14 (Oct. 2017), p. 141101. DOI: 10.1103/physrevlett.119.141101.

[15] LIGO-Virgo Collaboration. "GW170104: Observation of a 50-Solar-Mass Binary Black Hole Coalescence at Redshift 0.2". In: *Physical Review Letters* 118.22 (June 2017), p. 221101. DOI: 10.1103/physrevlett.118.221101.

[16] LIGO-Virgo Collaboration. “Search for Subsolar-Mass Ultracompact Binaries in Advanced LIGO’s First Observing Run”. In: *Physical Review Letters* 121.23 (Dec. 2018), p. 231103. DOI: 10.1103/physrevlett.121.231103.

[17] LIGO-Virgo Collaboration. “GW170817: Measurements of Neutron Star Radii and Equation of State”. In: *Physical Review Letters* 121.16 (Oct. 2018), p. 161101. DOI: 10.1103/physrevlett.121.161101.

[18] LIGO-Virgo Collaboration. “GW170817: Implications for the Stochastic Gravitational-Wave Background from Compact Binary Coalescences”. In: *Physical Review Letters* 120.9 (Feb. 2018), p. 091101. DOI: 10.1103/physrevlett.120.091101.

[19] LIGO-Virgo Collaboration. “Full band all-sky search for periodic gravitational waves in the O1 LIGO data”. In: *Physical Review D* 97.10 (May 2018), p. 102003. DOI: 10.1103/physrevd.97.102003.

[20] LIGO-Virgo Collaboration. “Constraints on cosmic strings using data from the first Advanced LIGO observing run”. In: *Physical Review D* 97.10 (May 2018), p. 102002. DOI: 10.1103/physrevd.97.102002.

[21] LIGO-Virgo Collaboration. “Search for Tensor, Vector, and Scalar Polarizations in the Stochastic Gravitational-Wave Background”. In: *Physical Review Letters* 120.20 (May 2018), p. 201102. DOI: 10.1103/physrevlett.120.201102.

[22] LIGO-Virgo Collaboration. “First Search for Nontensorial Gravitational Waves from Known Pulsars”. In: *Physical Review Letters* 120.3 (Jan. 2018), p. 031104. DOI: 10.1103/physrevlett.120.031104.

[23] LIGO-Virgo Collaboration. “Search for gravitational waves from Scorpius X-1 in the second Advanced LIGO observing run with an improved hidden Markov model”. In: *Physical Review D* 100.12 (Dec. 2019), p. 122002. DOI: 10.1103/physrevd.100.122002.

[24] B. P. Abbott et al. “Search for Gravitational-wave Signals Associated with Gamma-Ray Bursts during the Second Observing Run of Advanced LIGO and Advanced Virgo”. In: *The Astrophysical Journal* 886.1 (Nov. 2019), p. 75. DOI: 10.3847/1538-4357/ab4b48.

[25] LIGO-Virgo Collaboration. “Tests of General Relativity with GW170817”. In: *Physical Review Letters* 123.1 (July 2019), p. 011102. DOI: 10.1103/physrevlett.123.011102.

[26] LIGO-Virgo Collaboration. “Search for Subsolar Mass Ultracompact Binaries in Advanced LIGO’s Second Observing Run”. In: *Physical Review Letters* 123.16 (Oct. 2019), p. 161102. DOI: 10.1103/physrevlett.123.161102.

[27] LIGO-Virgo Collaboration. “Search for Eccentric Binary Black Hole Mergers with Advanced LIGO and Advanced Virgo during Their First and Second Observing Runs”. In: *The Astrophysical Journal* 883.2 (Sept. 2019), p. 149. DOI: 10.3847/1538-4357/ab3c2d.

[28] LIGO-Virgo Collaboration. “Search for intermediate mass black hole binaries in the first and second observing runs of the Advanced LIGO and Virgo network”. In: *Physical Review D* 100.6 (Sept. 2019), p. 064064. DOI: 10.1103/physrevd.100.064064.

[29] LIGO-Virgo Collaboration. "Binary Black Hole Population Properties Inferred from the First and Second Observing Runs of Advanced LIGO and Advanced Virgo". In: *The Astrophysical Journal* 882.2 (Sept. 2019), p. L24. DOI: 10.3847/2041-8213/ab3800.

[30] LIGO-Virgo Collaboration. "Searches for Gravitational Waves from Known Pulsars at Two Harmonics in 2015–2017 LIGO Data". In: *The Astrophysical Journal* 879.1 (June 2019), p. 10. DOI: 10.3847/1538-4357/ab20cb.

[31] LIGO-Virgo Collaboration. "Directional limits on persistent gravitational waves using data from Advanced LIGO's first two observing runs". In: *Physical Review D* 100.6 (Sept. 2019), p. 062001. DOI: 10.1103/physrevd.100.062001.

[32] LIGO-Virgo Collaboration. "Properties of the Binary Neutron Star Merger GW170817". In: *Physical Review X* 9.1 (Jan. 2019), p. 011001. DOI: 10.1103/physrevx.9.011001.

[33] LIGO-Virgo Collaboration. "All-sky search for short gravitational-wave bursts in the second Advanced LIGO and Advanced Virgo run". In: *Physical Review D* 100.2 (July 2019), p. 024017. DOI: 10.1103/physrevd.100.024017.

[34] LIGO-Virgo Collaboration. "All-sky search for continuous gravitational waves from isolated neutron stars using Advanced LIGO O2 data". In: *Physical Review D* 100.2 (July 2019), p. 024004. DOI: 10.1103/physrevd.100.024004.

[35] LIGO-Virgo Collaboration. "All-sky search for long-duration gravitational-wave transients in the second Advanced LIGO observing run". In: *Physical Review D* 99.10 (May 2019), p. 104033. DOI: 10.1103/physrevd.99.104033.

[36] LIGO-Virgo Collaboration. "Search for the isotropic stochastic background using data from Advanced LIGO's second observing run". In: *Physical Review D* 100.6 (Sept. 2019), p. 061101. DOI: 10.1103/physrevd.100.061101.

[37] LIGO-Virgo Collaboration. "Tests of general relativity with the binary black hole signals from the LIGO-Virgo catalog GWTC-1". In: *Physical Review D* 100.10 (Nov. 2019), p. 104036. DOI: 10.1103/physrevd.100.104036.

[38] LIGO-Virgo Collaboration. "Search for Transient Gravitational-wave Signals Associated with Magnetar Bursts during Advanced LIGO's Second Observing Run". In: *The Astrophysical Journal* 874.2 (Apr. 2019), p. 163. DOI: 10.3847/1538-4357/ab0e15.

[39] LIGO-Virgo Collaboration. "Search for Gravitational Waves from a Long-lived Remnant of the Binary Neutron Star Merger GW170817". In: *The Astrophysical Journal* 875.2 (Apr. 2019), p. 160. DOI: 10.3847/1538-4357/ab0f3d.

[40] LIGO-Virgo Collaboration. "Searches for Continuous Gravitational Waves from 15 Supernova Remnants and Fomalhaut b with Advanced LIGO". In: *The Astrophysical Journal* 875.2 (Apr. 2019), p. 122. DOI: 10.3847/1538-4357/ab113b.

[41] LIGO-Virgo Collaboration. "Narrow-band search for gravitational waves from known pulsars using the second LIGO observing run". In: *Physical Review D* 99.12 (June 2019), p. 122002. DOI: 10.1103/physrevd.99.122002.

[42] LIGO-Virgo Collaboration. "Low-latency Gravitational-wave Alerts for Multimessenger Astronomy during the Second Advanced LIGO and Virgo Observing Run". In: *The Astrophysical Journal* 875.2 (Apr. 2019), p. 161. DOI: 10.3847/1538-4357/ab0e8f.

[43] LIGO-Virgo Collaboration. "Constraining the p-Mode–g-Mode Tidal Instability with GW170817". In: *Physical Review Letters* 122.6 (Feb. 2019), p. 061104. DOI: 10.1103/physrevlett.122.061104.

[44] LIGO-Virgo Collaboration. "Gravitational-wave Constraints on the Equatorial Ellipticity of Millisecond Pulsars". In: *The Astrophysical Journal Letters* 902.1 (Oct. 2020), p. L21. DOI: 10.3847/2041-8213/abb655.

[45] LIGO-Virgo Collaboration. "Properties and astrophysical implications of the 150 Msun binary black hole merger GW190521". In: *The Astrophysical Journal* 900.1 (Sept. 2020), p. L13. DOI: 10.3847/2041-8213/aba493.

[46] LIGO-Virgo Collaboration. "GW190521: A Binary Black Hole Merger with a Total Mass of $150\ M_{\odot}$". In: *Physical Review Letters* 125.10 (Sept. 2020), p. 101102. DOI: 10.1103/physrevlett.125.101102.

[47] LIGO-Virgo Collaboration. "Model comparison from LIGO–Virgo data on GW170817's binary components and consequences for the merger remnant". In: *Classical and Quantum Gravity* 37.4 (Jan. 2020), p. 045006. DOI: 10.1088/1361-6382/ab5f7c.

[48] LIGO-Virgo Collaboration. "GW190412: Observation of a binary-black-hole coalescence with asymmetric masses". In: *Physical Review D* 102.4 (Aug. 2020), p. 043015. DOI: 10.1103/physrevd.102.043015.

[49] LIGO-Virgo Collaboration. "A guide to LIGO–Virgo detector noise and extraction of transient gravitational-wave signals". In: *Classical and Quantum Gravity* 37.5 (Feb. 2020), p. 055002. DOI: 10.1088/1361-6382/ab685e.

[50] LIGO-Virgo Collaboration. "GW190425: Observation of a Compact Binary Coalescence with Total Mass $\sim 3.4 M_{\odot}$". In: *The Astrophysical Journal Letters* 892.1 (Mar. 2020), p. L3. DOI: 10.3847/2041-8213/ab75f5.

[51] LIGO-Virgo-KAGRA Collaboration. "Prospects for observing and localizing gravitational-wave transients with Advanced LIGO, Advanced Virgo and KAGRA". In: *Living Reviews in Relativity* 23.1 (Sept. 2020). DOI: 10.1007/s41114-020-00026-9.

[52] LIGO-Virgo Collaboration. "Optically targeted search for gravitational waves emitted by core-collapse supernovae during the first and second observing runs of advanced LIGO and advanced Virgo". In: *Physical Review D* 101.8 (Apr. 2020), p. 084002. DOI: 10.1103/physrevd.101.084002.

[53] LIGO-Virgo Collaboration. "GW190814: Gravitational Waves from the Coalescence of a 23 Solar Mass Black Hole with a 2.6 Solar Mass Compact Object". In: *The Astrophysical Journal Letters* 896.2 (June 2020), p. L44. DOI: 10.3847/2041-8213/ab960f.

[54] LIGO-Virgo Collaboration. “Open data from the first and second observing runs of Advanced LIGO and Advanced Virgo”. In: *SoftwareX* 13 (Jan. 2021), p. 100658. DOI: 10.1016/j.softx.2021.100658.

[55] LIGO-Virgo Collaboration. “All-sky search for short gravitational-wave bursts in the third Advanced LIGO and Advanced Virgo run”. In: *Physical Review D* 104.12 (Dec. 2021), p. 122004. DOI: 10.1103/physrevd.104.122004.

[56] LIGO-Virgo Collaboration. “Search for Lensing Signatures in the Gravitational-Wave Observations from the First Half of LIGO–Virgo’s Third Observing Run”. In: *The Astrophysical Journal* 923.1 (Dec. 2021), p. 14. DOI: 10.3847/1538-4357/ac23db.

[57] LIGO-Virgo-KAGRA Collaboration. “All-sky search for long-duration gravitational-wave bursts in the third Advanced LIGO and Advanced Virgo run”. In: *Physical Review D* 104.10 (Nov. 2021), p. 102001. DOI: 10.1103/physrevd.104.102001.

[58] LIGO-Virgo-KAGRA Collaboration. “Constraints from LIGO O3 Data on Gravitational-wave Emission Due to R-modes in the Glitching Pulsar PSR J0537–6910”. In: *The Astrophysical Journal* 922.1 (Nov. 2021), p. 71. DOI: 10.3847/1538-4357/ac0d52.

[59] LIGO-Virgo-KAGRA Collaboration. “Searches for Continuous Gravitational Waves from Young Supernova Remnants in the Early Third Observing Run of Advanced LIGO and Virgo”. In: *The Astrophysical Journal* 921.1 (Nov. 2021), p. 80. DOI: 10.3847/1538-4357/ac17ea.

[60] LIGO-Virgo-KAGRA Collaboration. “All-sky search for continuous gravitational waves from isolated neutron stars in the early O3 LIGO data”. In: *Physical Review D* 104.8 (Oct. 2021), p. 082004. DOI: 10.1103/physrevd.104.082004.

[61] LIGO-Virgo-KAGRA Collaboration. “Diving below the Spin-down Limit: Constraints on Gravitational Waves from the Energetic Young Pulsar PSR J0537-6910”. In: *The Astrophysical Journal Letters* 913.2 (May 2021), p. L27. DOI: 10.3847/2041-8213/abffcd.

[62] LIGO-Virgo-KAGRA Collaboration. “Constraints on Cosmic Strings Using Data from the Third Advanced LIGO–Virgo Observing Run”. In: *Physical Review Letters* 126.24 (June 2021), p. 241102. DOI: 10.1103/physrevlett.126.241102.

[63] LIGO-Virgo Collaboration. “All-sky search in early O3 LIGO data for continuous gravitational-wave signals from unknown neutron stars in binary systems”. In: *Physical Review D* 103.6 (Mar. 2021), p. 064017. DOI: 10.1103/physrevd.103.064017.

[64] LIGO-Virgo Collaboration. “A Gravitational-wave Measurement of the Hubble Constant Following the Second Observing Run of Advanced LIGO and Virgo”. In: *The Astrophysical Journal* 909.2 (Mar. 2021), p. 218. DOI: 10.3847/1538-4357/abdcb7.

[65] LIGO–Virgo–KAGRA Collaboration. "Upper limits on the isotropic gravitational-wave background from Advanced LIGO and Advanced Virgo's third observing run". In: *Physical Review D* 104.2 (July 2021), p. 022004. DOI: 10.1103/physrevd.104.022004.

[66] LIGO-Virgo Collaboration. "Tests of general relativity with binary black holes from the second LIGO-Virgo gravitational-wave transient catalog". In: *Physical Review D* 103.12 (June 2021), p. 122002. DOI: 10.1103/physrevd.103.122002.

[67] LIGO-Virgo Collaboration. "Search for Gravitational Waves Associated with Gamma-Ray Bursts Detected by Fermi and Swift during the LIGO–Virgo Run O3a". In: *The Astrophysical Journal* 915.2 (July 2021), p. 86. DOI: 10.3847/1538-4357/abee15.

[68] LIGO-Virgo-KAGRA Collaboration. "Search for anisotropic gravitational-wave backgrounds using data from Advanced LIGO and Advanced Virgo's first three observing runs". In: *Physical Review D* 104.2 (July 2021), p. 022005. DOI: 10.1103/physrevd.104.022005.

[69] LIGO-Virgo-KAGRA Collaboration. "Observation of Gravitational Waves from Two Neutron Star–Black Hole Coalescences". In: *The Astrophysical Journal Letters* 915.1 (June 2021), p. L5. DOI: 10.3847/2041-8213/ac082e.

[70] LIGO-Virgo-KAGRA Collaboration. "Search for gravitational waves from Scorpius X-1 with a hidden Markov model in O3 LIGO data". In: *Physical Review D* 106.6 (Sept. 2022), p. 062002. DOI: 10.1103/physrevd.106.062002.

[71] LIGO-Virgo-KAGRA Collaboration. "Search for continuous gravitational wave emission from the Milky Way center in O3 LIGO-Virgo data". In: *Physical Review D* 106.4 (Aug. 2022), p. 042003. DOI: 10.1103/physrevd.106.042003.

[72] LIGO-Virgo Collaboration. "Search for intermediate-mass black hole binaries in the third observing run of Advanced LIGO and Advanced Virgo". In: *Astronomy & Astrophysics* 659 (Mar. 2022), A84. DOI: 10.1051/0004-6361/202141452.

[73] LIGO-Virgo-KAGRA Collaboration. "All-sky, all-frequency directional search for persistent gravitational waves from Advanced LIGO's and Advanced Virgo's first three observing runs". In: *Physical Review D* 105.12 (June 2022), p. 122001. DOI: 10.1103/physrevd.105.122001.

[74] LIGO-Virgo-KAGRA Collaboration. "Narrowband Searches for Continuous and Long-duration Transient Gravitational Waves from Known Pulsars in the LIGO-Virgo Third Observing Run". In: *The Astrophysical Journal* 932.2 (June 2022), p. 133. DOI: 10.3847/1538-4357/ac6ad0.

[75] LIGO-Virgo-KAGRA Collaboration. "All-sky search for gravitational wave emission from scalar boson clouds around spinning black holes in LIGO O3 data". In: *Physical Review D* 105.10 (May 2022), p. 102001. DOI: 10.1103/physrevd.105.102001.

[76] LIGO-Virgo-KAGRA Collaboration. “Constraints on dark photon dark matter using data from LIGO’s and Virgo’s third observing run”. In: *Physical Review D* 105.6 (Mar. 2022), p. 063030. DOI: 10.1103/physrevd.105.063030.

[77] LIGO-Virgo Collaboration. “Search of the early O3 LIGO data for continuous gravitational waves from the Cassiopeia A and Vela Jr. supernova remnants”. In: *Physical Review D* 105.8 (Apr. 2022), p. 082005. DOI: 10.1103/physrevd.105.082005.

[78] LIGO-Virgo-KAGRA Collaboration. “Search for Subsolar-Mass Binaries in the First Half of Advanced LIGO’s and Advanced Virgo’s Third Observing Run”. In: *Physical Review Letters* 129.6 (Aug. 2022), p. 061104. DOI: 10.1103/physrevlett.129.061104.

[79] LIGO-Virgo-KAGRA Collaboration. “Search for Gravitational Waves Associated with Gamma-Ray Bursts Detected by Fermi and Swift during the LIGO–Virgo Run O3b”. In: *The Astrophysical Journal* 928.2 (Apr. 2022), p. 186. DOI: 10.3847/1538-4357/ac532b.

[80] LIGO-Virgo-KAGRA Collaboration. “Search for continuous gravitational waves from 20 accreting millisecond x-ray pulsars in O3 LIGO data”. In: *Physical Review D* 105.2 (Jan. 2022), p. 022002. DOI: 10.1103/physrevd.105.022002.

[81] LIGO-Virgo-KAGRA Collaboration. “Searches for Gravitational Waves from Known Pulsars at Two Harmonics in the Second and Third LIGO-Virgo Observing Runs”. English. In: *ASTROPHYSICAL JOURNAL* 935.1 (Aug. 2022). ISSN: 0004-637X. DOI: 10.3847/1538-4357/ac6acf.

[82] A. Albert et al. “Search for High-energy Neutrinos from Binary Neutron Star Merger GW170817 with ANTARES, IceCube, and the Pierre Auger Observatory”. In: *The Astrophysical Journal* 850.2 (Nov. 2017), p. L35. DOI: 10.3847/2041-8213/aa9aed.

[83] A. Albert et al. “Search for Multimessenger Sources of Gravitational Waves and High-energy Neutrinos with Advanced LIGO during Its First Observing Run, ANTARES, and IceCube”. In: *The Astrophysical Journal* 870.2 (Jan. 2019), p. 134. DOI: 10.3847/1538-4357/aaf21d.

[84] Aidan F. Brooks et al. “Point absorbers in Advanced LIGO”. In: *Applied Optics* 60.13 (Apr. 2021), p. 4047. DOI: 10.1364/ao.419689.

[85] A. Buikema et al. “Sensitivity and performance of the Advanced LIGO detectors in the third observing run”. In: *Physical Review D* 102.6 (Sept. 2020), p. 062003. DOI: 10.1103/physrevd.102.062003.

[86] Fermi Gamma-ray Burst Monitor Team, LIGO-Virgo Collaboration. “A Fermi Gamma-ray Burst Monitor Search for Electromagnetic Signals Coincident with Gravitational-Wave Candidates in Advanced LIGO’s First Observing Run”. In: *The Astrophysical Journal* 871.1 (Jan. 2019), p. 90. DOI: 10.3847/1538-4357/aaf726.

[87] D Davis et al. “LIGO detector characterization in the second and third observing runs”. In: *Classical and Quantum Gravity* 38.13 (June 2021), p. 135014. DOI: 10.1088/1361-6382/abfd85.

[88] Fermi Gamma-ray Burst Monitor Team, LIGO-Virgo Collaboration. "A Joint Fermi-GBM and LIGO/Virgo Analysis of Compact Binary Mergers from the First and Second Gravitational-wave Observing Runs". In: *The Astrophysical Journal* 893.2 (Apr. 2020), p. 100. DOI: 10.3847/1538-4357/ab7d3e.

[89] Wenxuan Jia et al. "Point Absorber Limits to Future Gravitational-Wave Detectors". In: *Physical Review Letters* 127.24 (Dec. 2021), p. 241102. DOI: 10.1103/physrevlett.127.241102.

[90] LIGO-Virgo Collaboration. "GWTC-1: A Gravitational-Wave Transient Catalog of Compact Binary Mergers Observed by LIGO and Virgo during the First and Second Observing Runs". In: *Physical Review X* 9.3 (Sept. 2019), p. 031040. DOI: 10.1103/physrevx.9.031040.

[91] LIGO Scientific Collaboration. *Instrument Science White Paper 2020*. Tech. rep. LIGO-T2000407–v3. Aug. 2020.

[92] LIGO-Virgo Collaboration. *GWTC-2.1: Deep Extended Catalog of Compact Binary Coalescences Observed by LIGO and Virgo During the First Half of the Third Observing Run*. 2021. DOI: 10.48550/ARXIV.2108.01045.

[93] LIGO-Virgo-KAGRA Collaboration. *GWTC-3: Compact Binary Coalescences Observed by LIGO and Virgo During the Second Part of the Third Observing Run*. 2021. DOI: 10.48550/ARXIV.2111.03606.

[94] LIGO Scientific Collaboration. *Instrument Science White Paper 2021*. Tech. rep. LIGO-T2100298–v2. LIGO Scientific Collaboration, July 2021.

[95] LIGO-Virgo Collaboration. "GWTC-2: Compact Binary Coalescences Observed by LIGO and Virgo during the First Half of the Third Observing Run". In: *Physical Review X* 11.2 (June 2021), p. 021053. DOI: 10.1103/physrevx.11.021053.

[96] LIGO-Virgo-KAGRA Collaboration. "First joint observation by the underground gravitational-wave detector KAGRA with GEO 600". In: *Progress of Theoretical and Experimental Physics* 2022.6 (June 2022). ISSN: 2050-3911. DOI: 10.1093/ptep/ptac073. eprint: https://academic.oup.com/ptep/article-pdf/2022/6/063F01/43989382/ptac073.pdf. URL: https://doi.org/10.1093/ptep/ptac073.

[97] L. McCuller et al. "LIGO's quantum response to squeezed states". In: *Physical Review D* 104.6 (Sept. 2021), p. 062006. DOI: 10.1103/physrevd.104.062006.

[98] P Nguyen et al. "Environmental noise in advanced LIGO detectors". In: *Classical and Quantum Gravity* 38.14 (June 2021), p. 145001. DOI: 10.1088/1361-6382/ac011a.

[99] E Schwartz et al. "Improving the robustness of the advanced LIGO detectors to earthquakes". In: *Classical and Quantum Gravity* 37.23 (Nov. 2020), p. 235007. DOI: 10.1088/1361-6382/abbc8c.

[100] DES, LIGO-Virgo Collaboration. "First Measurement of the Hubble Constant from a Dark Standard Siren using the Dark Energy Survey Galaxies and the LIGO/Virgo Binary–Black-hole Merger GW170814". In: *The Astrophysical Journal* 876.1 (Apr. 2019), p. L7. DOI: 10.3847/2041-8213/ab14f1.

[101] S Soni et al. “Reducing scattered light in LIGO’s third observing run”. In: *Classical and Quantum Gravity* 38.2 (Jan. 2021), p. 025016. DOI: 10.1088/1361-6382/abc906.

[102] M. Tse et al. “Quantum-Enhanced Advanced LIGO Detectors in the Era of Gravitational-Wave Astronomy”. In: *Physical Review Letters* 123.23 (Dec. 2019), p. 231107. DOI: 10.1103/physrevlett.123.231107.

[103] LIGO-Virgo Collaboration, Fermi GBM, INTEGRAL, IceCube Collaboration, AstroSatCadmium Zinc Telluride Imager Team, IPN Collaboration, The Insight-Hxmt Collaboration, ANTARES Collaboration,The Swift Collaboration, AGILE Team, The 1M2H Team, The Dark Energy Camera GW-EM Collaboration, theDES Collaboration, The DLT40 Collaboration, GRAWITA: GRAvitational Wave Inaf TeAm, The Fermi Large AreaTelescope Collaboration, ATCA: Australia Telescope Compact Array, ASKAP: Australian SKA Pathfinder, LasCumbres Observatory Group, OzGrav, DWF (Deeper, Wider, Faster Program), AST3, CAASTRO Collaborations, TheVINROUGE Collaboration, MASTER Collaboration, J-GEM, GROWTH, JAGWAR, Caltech- NRAO, TTU-NRAO,NuSTAR Collaborations, Pan-STARRS, The MAXI Team, TZAC Consortium, KU Collaboration, Nordic OpticalTelescope, ePESSTO, GROND, Texas Tech University, SALT Group, TOROS: Transient Robotic Observatory of theSouth Collaboration, The BOOTES Collaboration, MWA: Murchison Widefield Array, The CALET Collaboration,IKI-GW Follow-up Collaboration, H.E.S.S. Collaboration, LOFAR Collaboration, LWA: Long Wavelength Array,HAWC Collaboration, The Pierre Auger Collaboration, ALMA Collaboration, Euro VLBI Team, Pi of the SkyCollaboration, The Chandra Team at McGill University, DFN: Desert Fireball Network, ATLAS, High TimeResolution Universe Survey, RIMAS, RATIR, SKA South Africa/MeerKAT. “Multi-messenger Observations of a Binary Neutron Star Merger”. In: *The Astrophysical Journal* 848.2 (Oct. 2017), p. L12. DOI: 10.3847/2041-8213/aa91c9.